Adaptive Detection and Estimation Using a Conformal Array Antenna

A Thesis
Presented to
The Academic Faculty

by

Ryan K. Hersey

In Partial Fulfillment
of the Requirements for the Degree
Doctor of Philosophy in
Electrical and Computer Engineering

Georgia Institute of Technology
December 2004

Adaptive Detection and Estimation Using a Conformal Array Antenna

James H. McClellan (advisor)
School of Electrical and Computer Engineering

William L. Melvin
Georgia Tech Research Institute

Mark A. Richards
School of Electrical and Computer Engineering

Date Approved: November 22, 2004

ACKNOWLEDGEMENT

I first thank my advisor Dr. James McClellan for his valuable support and motivation over the last four years. I especially thank Dr. William Melvin of the Georgia Tech Research Institute for his generous support and supervision of my work and for teaching me the finer points of adaptive radar. I also thank Dr. Mark Richards for first introducing me to the concepts of radar and for serving on my reading committee. I also thank Dr. Greg Showman of the Georgia Tech Research Institute for many invaluable discussions on the subject matter. Finally, I thank Ed Culpepper and the US Air Force Research Laboratory for funding this work under contract F33615-97-D-1095-0007.

TABLE OF CONTENTS

LIST OF TABLES

LIST OF FIGURES

LIST OF ABBREVIATIONS

AF	Array Factor
CNR	Clutter-to-Noise Ratio
CRLB	Cramer-Rao Lower Bound
DOF	Degrees Of Freedom
EFA	Extended Factored Algorithm
EP	Element Pattern
GMTI	Ground Moving Target Indication
HODW	Higher-Order Doppler Warping
JDO	Joint Domain Optimum
JDL	Joint Domain Localization
JDSTAP	Joint Domain STAP
JointSTARS	Joint Surveillance Target Attack Radar System
MCARM	Multi-Channel Airborne Radar Measurements
MLE	Maximum Likelihood Estimate
MTI	Moving Target Indication
MVDR	Minimum Variance Distortionless Response
PRF	Pulse Repetition Frequency
PRI	Pulse Repetition Interval
RMB	Reed Mallett Brennan
RMS	Root Mean Square
ROC	Receiver Operator Characteristic
SAF	Subarray Factor

SINR	Signal-to-Interference-plus-Noise Ratio
SLL	Side-Lobe Level
SNR	Signal-to-Noise Ratio
STAP	Space-Time Adaptive Processing
SVM	Steering Vector Mismatch
UAV	Unmanned Aerial Vehicle
UESA	UHF Electronically Scanned Array
UHF	Ultra High Frequency
ULA	Uniform Linear Array

SUMMARY

Conformal arrays possess certain desirable characteristics for deployment on unmanned aerial vehicles and other payload-limited platforms: aerodynamic design, minimal payload weight, increased field of view, and ease of integration with diverse sensor functions. However, the conformal array's nonplanar geometry causes high adaptive losses in conventional space-time adaptive processing (STAP) algorithms.

In this thesis, we develop a conformal array signal model and apply it to evaluate the performance of conventional STAP algorithms on simulated ground clutter data. We find that array-induced clutter nonstationarity leads to high adaptive losses, which greatly burden detection performance. To improve adaptive performance, we investigate the application of existing equivalent-linear-array transformations and develop novel deterministic and adaptive angle-Doppler compensation techniques, which align nonstationary clutter returns. Through the application of these techniques, we are able to nearly fully mitigate the nonstationary behavior yielding performance similar to that of a conventional planar array. Finally, we investigate the impact of array errors on the performance of conformal arrays, and propose several array calibration techniques as ameliorating solutions.

CHAPTER 2

BACKGROUND

2.1 Overview

In this chapter we present an overview of STAP fundamentals and ground-clutter characteristics for the case of a ULA. We assume a basic understanding of radar signal processing, including both Doppler processing and beamforming. More detailed information on these topics can be found in [23-24].

Throughout this thesis, we use the fixed coordinate system shown in Fig. 2.1 with the x-axis aligned to true North, the y-axis pointing due West, and the z-axis perpendicularly directed away from the Earth's surface. The azimuth angle, ϕ, is measured positive in the counterclockwise direction from true North, while the elevation angle, θ, characterizing the depression angle from the x-y plane, is negative in a downward direction from the horizon. For convenience we define $\boldsymbol{\psi} = \begin{bmatrix} \phi & \theta \end{bmatrix}^T$. A unit vector pointing in the direction $\boldsymbol{\psi}$ is

$$\mathbf{k}(\boldsymbol{\psi}) = \cos(\theta)\cos(\phi)\hat{\mathbf{x}} + \cos(\theta)\sin(\phi)\hat{\mathbf{y}} + \sin(\theta)\hat{\mathbf{z}}. \tag{2.1}$$

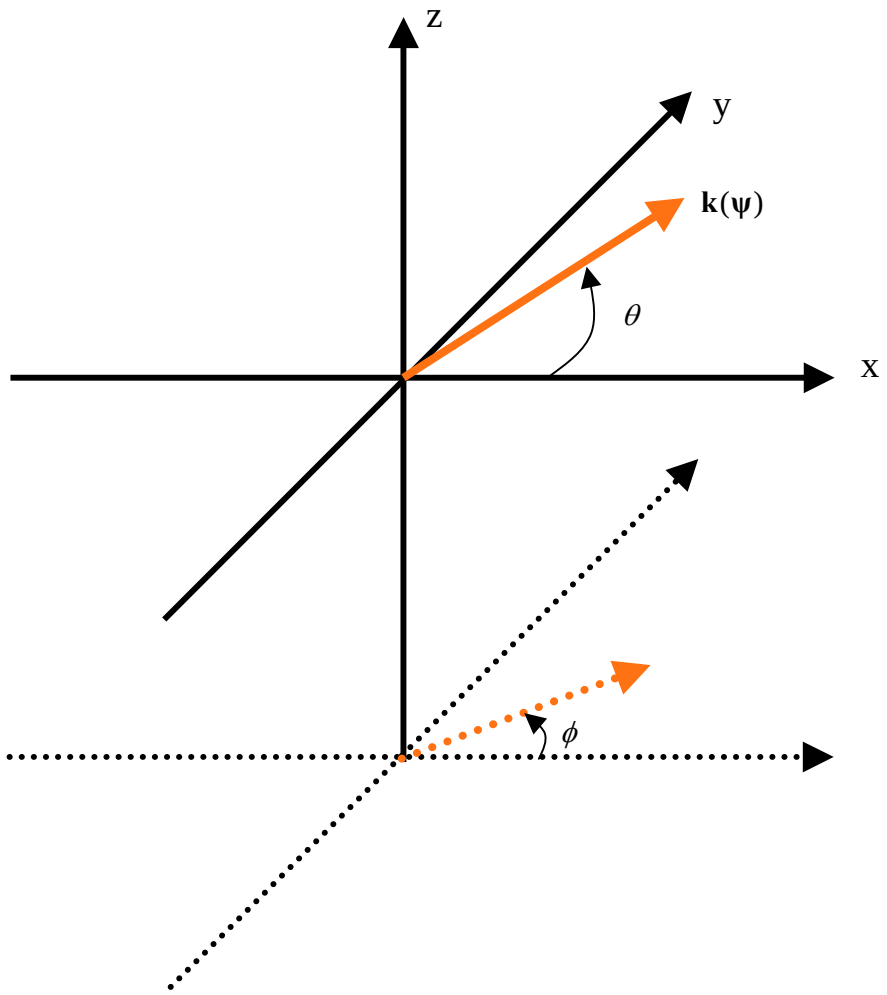

Figure 2.1. Reference coordinate system.

2.2 *STAP Fundamentals*

Moving target indication (MTI) is a common radar application involving the detection of airborne and ground targets. Ground moving target indication (GMTI) presents a particularly difficult problem as the targets are masked by ground clutter interference. STAP is a joint-domain (spatial and temporal) adaptive approach that is particularly useful in detecting weak and slow-moving ground targets in challenging clutter environments.

We present an overview of STAP in the block diagram in Fig. 2.2. We first pre-process the data cube to account for any nonstationary behavior. We describe this in more detail in Chapters 5 and 6. We then use the adjusted data in the STAP processor, which consists of three steps. In the STAP processor, we first estimate the space-time covariance matrix for each range bin using surrounding range data. Next we use the estimated space-time covariance matrix to estimate the optimum filter response for all desired Doppler and spatial frequencies. In the final part of the STAP processor, we compare the matched filter output with a threshold to determine whether or not a target is present. As the final overall stage, we use the filtered data for a variety of applications including bearing estimation and tracking.

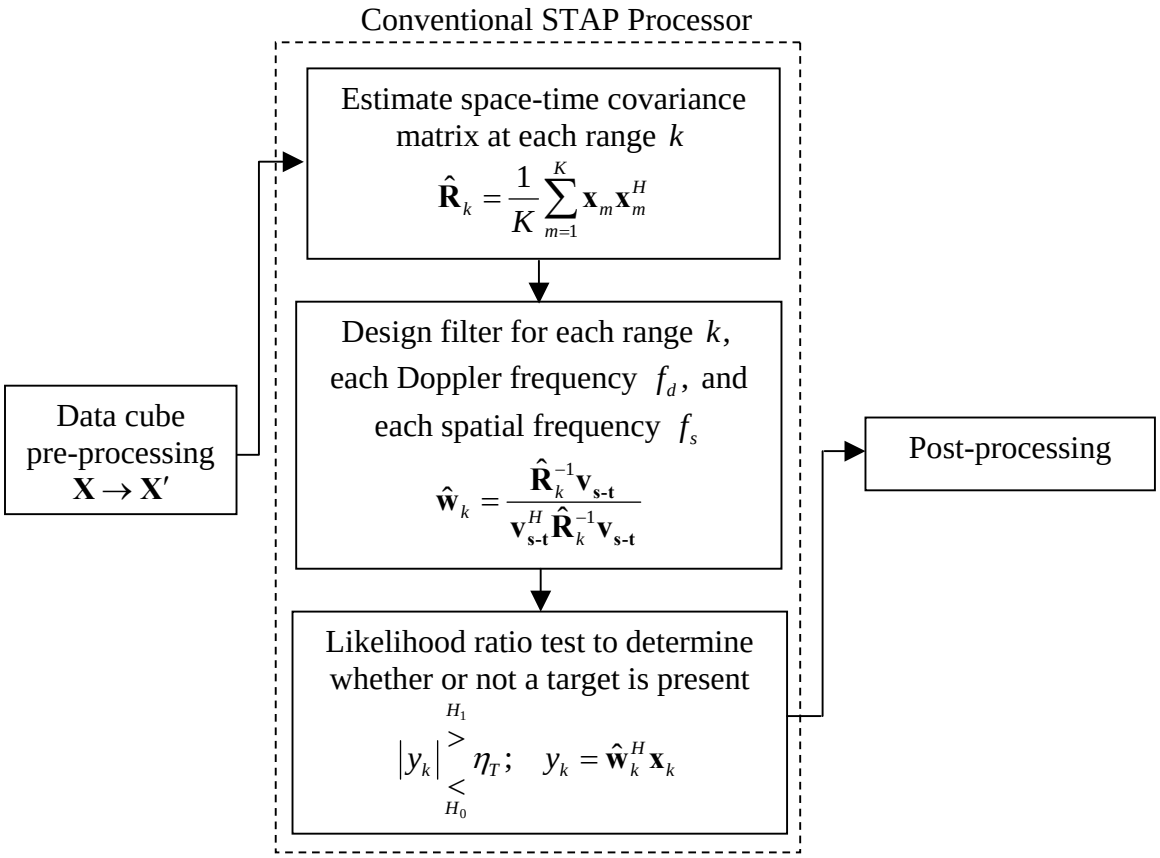

Figure 2.2. Overview of STAP

As a joint space-time adaptive technique, STAP requires the use of all three dimensions of the radar data cube, channel (subarray), pulse (slow time), and range (fast time), as shown in Fig. 2.3. We can represent the data from each range cell in matrix form as

$$\mathbf{X}_k = \begin{bmatrix} [\mathbf{X}_k]_{1,1} & [\mathbf{X}_k]_{1,2} & \cdots & [\mathbf{X}_k]_{1,N} \\ [\mathbf{X}_k]_{2,1} & [\mathbf{X}_k]_{2,2} & \cdots & [\mathbf{X}_k]_{2,N} \\ \vdots & \vdots & \ddots & \vdots \\ [\mathbf{X}_k]_{M,1} & [\mathbf{X}_k]_{M,2} & \cdots & [\mathbf{X}_k]_{M,N} \end{bmatrix}, \tag{2.2}$$

where rows correspond to channels (M total) and columns corresponds to pulses (N total). We define this as a space-time data snapshot. By stacking each of the N columns on top of each other, we can represent the same data in vector form $\mathbf{x}_k$.

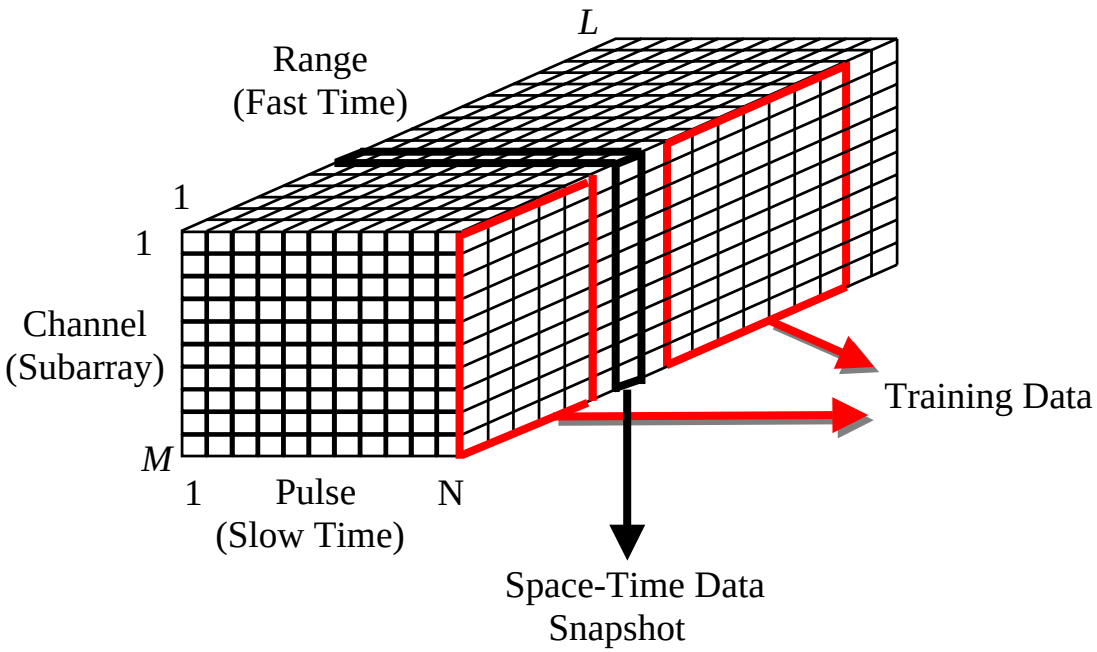

Figure 2.3. Radar data cube indicating three dimensions of data and training over range.

We typically model individual point scatterers using a space-time steering vector of the form

$$\mathbf{s}_{\text{s-t}} = \mathbf{s}_{\text{t}} \otimes \mathbf{s}_{\text{s}}, \tag{2.3}$$

where $\mathbf{s}_{\text{t}}$ is the temporal steering vector, $\mathbf{s}_{\text{s}}$ is the spatial steering vector, and $\otimes$ is the Kronecker product. For a radar system with a constant pulse repetition interval (PRI), T, we define the temporal steering vector as

$$\mathbf{s}_{\text{t}} = \begin{bmatrix} 1 & e^{j2\pi f_d T} & e^{j2\pi 2 f_d T} & \dots & e^{j2\pi(N-1) f_d T} \end{bmatrix}, \tag{2.4}$$

where $f_d = \dfrac{2v}{\lambda}$ is the Doppler frequency of a scatterer with radial velocity v relative to the radar and for a signal of wavelength λ. For a ULA we define the spatial steering vector as

$$\mathbf{s}_{\text{s}} = \begin{bmatrix} 1 & e^{j2\pi f_s} & e^{j2\pi 2 f_s} & \dots & e^{j2\pi(M-1) f_s} \end{bmatrix}, \tag{2.5}$$

where $f_s = \dfrac{d}{\lambda}\cos(\phi_{cone})$ is the spatial frequency for a ULA with element spacing, d, at a cone angle, ϕ_{cone} as shown in Fig. 2.4 [23-25].

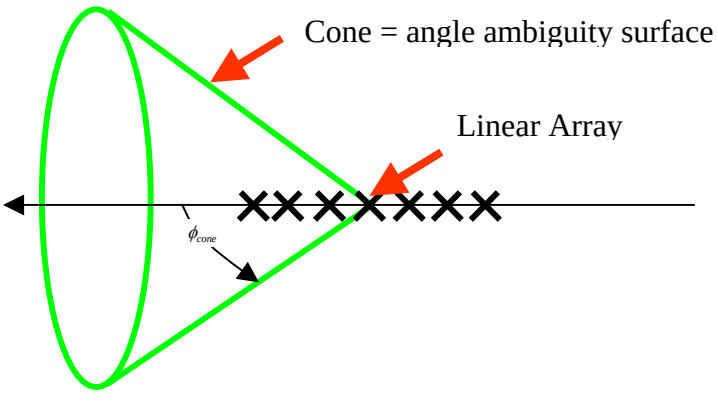

Figure 2.4. Cone ambiguity surface for a linear array.

The goal of STAP is to maximize the probability of detection $\left(P_D\right)$ for a given Doppler, angle, and range using an optimal linear space-time filter of the form

$$y_k = \mathbf{w}_k^H \mathbf{x}_k \,, \tag{2.6}$$

where $\mathbf{x}_k$ is the space-time data snapshot at range k and $\mathbf{w}_k$ is a complex weight vector. Figure 2.5 shows an example angle-Doppler power spectra for a side-looking ULA in the presence of ground clutter and jamming. Jammers impinge on the array at a fixed angle and are white in Doppler, resulting in the vertical profile as indicated in the angle-Doppler spectra. Ground clutter impinges on the array from all azimuth angles with varying Dopplers. We describe ground clutter in more detail in Section 2.3. Figure 2.6 shows the corresponding filter response with indicated nulls on the clutter ridge and jammers.

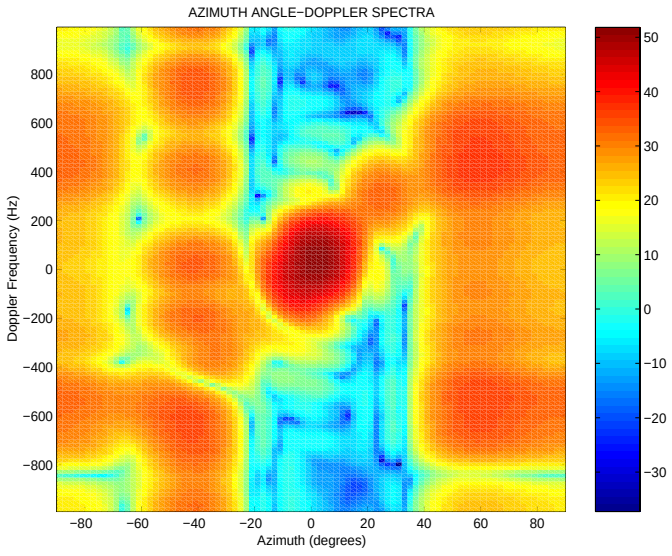

Figure 2.5. Angle-Doppler power spectra for a side-looking ULA in the presence of ground clutter and jammers.

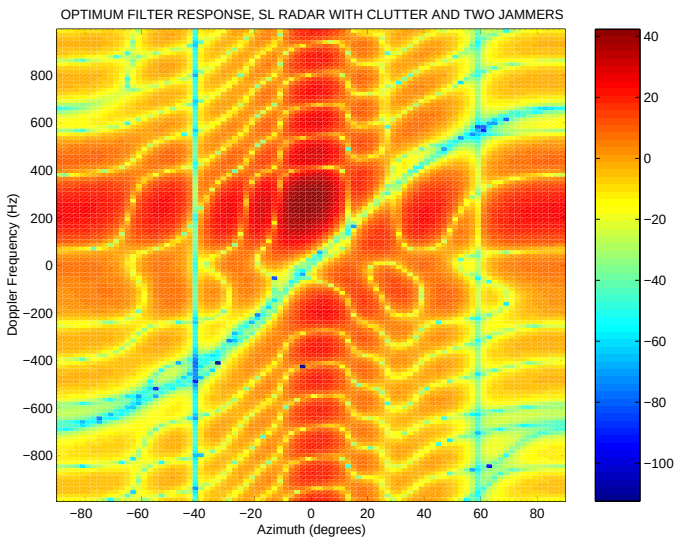

Figure 2.6. Filter response corresponding to angle-Doppler spectra shown in Fig. 2.4.

We compare the filter output, y_k, with a threshold via a likelihood ratio test of the form

$$|y_k| \underset{H_0}{\overset{H_1}{\gtrless}} \eta_T, \tag{2.7}$$

where we determine the detection threshold, η_T, using a preset probability of false alarm (P_{FA}) [5, 25]. Figure 2.7 shows typical receiver operator characteristic (ROC) curves for various Swerling target models [23]. These plots show that maximizing P_D is equivalent to maximizing the signal-to-interference-plus-noise ratio (SINR). Additionally, small losses in SINR can lead to large losses in P_D, which makes maximizing SINR of critical importance [25].

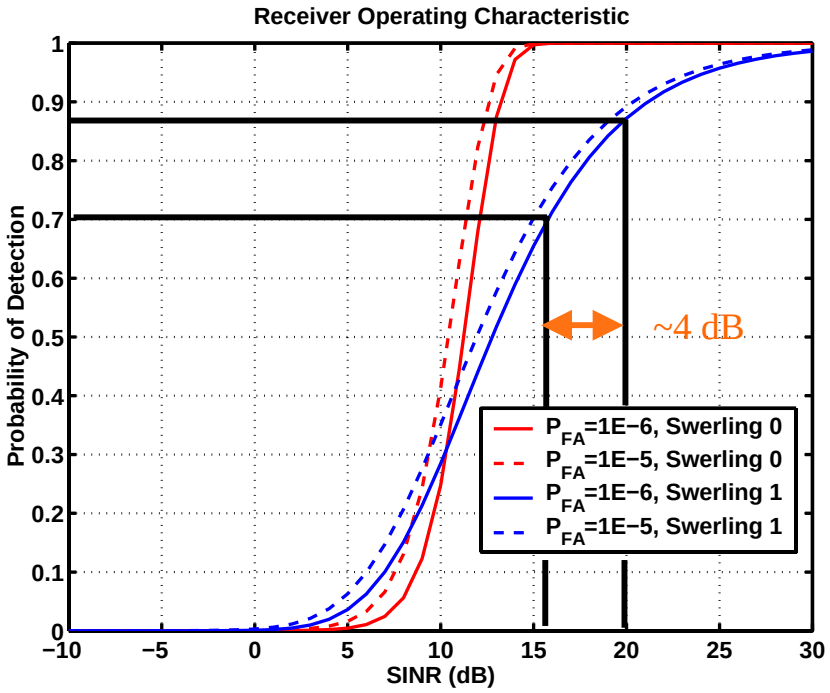

Figure 2.7. ROC curves for varying P_{FA} and Swerling models.

We define SINR as

$$\text{SINR} = \frac{\mathbf{w}_k^H \mathbf{R}_\mathbf{s} \mathbf{w}_k}{\mathbf{w}_k^H \mathbf{R}_k \mathbf{w}_k}, \tag{2.8}$$

where $\mathbf{R}_k$ is the noise plus interference covariance matrix at range bin k, and $\mathbf{R}_\mathbf{s} = \sigma_s^2 \mathbf{s}_{\mathbf{s\text{-}t}} \mathbf{s}_{\mathbf{s\text{-}t}}^H$ is the signal covariance matrix with signal power σ_s^2, which can be calculated from the radar equation [23].

The optimal weight vector in the SINR sense is the minimum variance distortionless response (MVDR) weight vector, [5, 24, 26]

$$\mathbf{w}_{\mathbf{opt}/k} = \frac{\mathbf{R}_k^{-1} \mathbf{s}_{\mathbf{s\text{-}t}}}{\mathbf{s}_{\mathbf{s\text{-}t}}^H \mathbf{R}_k^{-1} \mathbf{s}_{\mathbf{s\text{-}t}}}, \tag{2.9}$$

which gives the optimal SINR as

$$\mathrm{SINR}_{\mathrm{opt}} = \frac{\mathbf{w}_{\mathbf{opt}/k}^{H}\mathbf{R}_{\mathbf{s}}\mathbf{w}_{\mathbf{opt}/k}}{\mathbf{w}_{\mathbf{opt}/k}^{H}\mathbf{R}_{k}\mathbf{w}_{\mathbf{opt}/k}} = \sigma_s^2\mathbf{s}_{\mathbf{s\text{-}t}}^{H}\mathbf{R}_{k}^{-1}\mathbf{s}_{\mathbf{s\text{-}t}}. \tag{2.10}$$

In practice, the true interference plus noise covariance matrix, $\mathbf{R}_k$, is unknown, and we must find an estimate using training data. A commonly used estimate is the maximum likelihood estimate (MLE), which has the form

$$\hat{\mathbf{R}}_k = \frac{1}{K}\sum_{m=1}^{K}\mathbf{x}_m\mathbf{x}_m^{H}, \tag{2.11}$$

where K is the total number of training bins [5]. Additionally, as a result of element position errors, the true space-time steering vector, $\mathbf{s}_{\mathbf{s\text{-}t}}$, is generally unknown requiring the use of the surrogate $\mathbf{v}_{\mathbf{s\text{-}t}}$. Applying these estimates, we define the adaptive weight vector as

$$\mathbf{w}_{\mathbf{adap}} = \frac{\hat{\mathbf{R}}_k^{-1}\mathbf{v}_{\mathbf{s\text{-}t}}}{\mathbf{v}_{\mathbf{s\text{-}t}}^{H}\hat{\mathbf{R}}_k^{-1}\mathbf{v}_{\mathbf{s\text{-}t}}}, \tag{2.12}$$

which gives the adaptive SINR as

$$\mathrm{SINR}_{\mathrm{adap}} = \frac{\mathbf{w}_{\mathbf{adap}/k}^{H}\mathbf{R}_{\mathbf{s}}\mathbf{w}_{\mathbf{adap}/k}}{\mathbf{w}_{\mathbf{adap}/k}^{H}\mathbf{R}_{k}\mathbf{w}_{\mathbf{adap}/k}} = \frac{\sigma_s^2\left|\mathbf{v}_{\mathbf{s\text{-}t}}^{H}\hat{\mathbf{R}}_k^{-1}\mathbf{s}_{\mathbf{s\text{-}t}}\right|^2}{\mathbf{v}_{\mathbf{s\text{-}t}}^{H}\hat{\mathbf{R}}_k^{-1}\mathbf{R}_k\hat{\mathbf{R}}_k^{-1}\mathbf{v}_{\mathbf{s\text{-}t}}}. \tag{2.13}$$

For convenience, we divide the adaptive SINR into signal-to-noise-ratio (SNR) and SINR loss terms such that

$$\mathrm{SINR}_{\mathrm{adap}} = \mathrm{SNR}\cdot L_{s,1}\cdot L_{s,2}, \tag{2.14}$$

where $\mathrm{SNR} = \dfrac{\mathbf{w}^{H}\mathbf{R}_{\mathbf{s}}\mathbf{w}}{\mathbf{w}^{H}\mathbf{R}_{\mathbf{n}}\mathbf{w}} = MN\dfrac{\sigma_s^2}{\sigma_n^2}$ is the maximum array signal to noise ratio with white noise covariance, $\mathbf{R}_{\mathbf{n}} = \sigma_n^2\mathbf{I}$, $L_{s,1} = \dfrac{\mathrm{SINR}_{\mathrm{opt}}}{\mathrm{SNR}}$ is the clairvoyant loss resulting from

interference (colored noise) and $L_{s,2} = \dfrac{\text{SINR}_{\text{adap}}}{\text{SINR}_{\text{opt}}}$ is the adaptive loss resulting from estimation errors. Evaluating $L_{s,1}$ and $L_{s,2}$ gives the relations

$$L_{s,1} = \sigma_n^2 \frac{\mathbf{s}_{\mathbf{s-t}}^H \mathbf{R}_k^{-1} \mathbf{s}_{\mathbf{s-t}}}{\mathbf{s}_{\mathbf{s-t}}^H \mathbf{s}_{\mathbf{s-t}}} = \sigma_n^2 \frac{\mathbf{s}_{\mathbf{s-t}}^H \mathbf{R}_k^{-1} \mathbf{s}_{\mathbf{s-t}}}{NM}, \tag{2.15}$$

and

$$L_{s,2} = \frac{\left| \mathbf{v}_{\mathbf{s-t}}^H \hat{\mathbf{R}}_k^{-1} \mathbf{s}_{\mathbf{s-t}} \right|^2}{\left(\mathbf{s}_{\mathbf{s-t}}^H \mathbf{R}_k^{-1} \mathbf{s}_{\mathbf{s-t}} \right) \left(\mathbf{v}_{\mathbf{s-t}}^H \hat{\mathbf{R}}_k^{-1} \mathbf{R}_k \hat{\mathbf{R}}_k^{-1} \mathbf{v}_{\mathbf{s-t}} \right)}. \tag{2.16}$$

If the training data is independent and identically distributed (i.i.d.) and the space-time matched filter is known, i.e., $\mathbf{v}_{\mathbf{s-t}} = \mathbf{s}_{\mathbf{s-t}}$, the mean estimation loss is

$$E\left[L_{s,2} \right] = \frac{K + 2 - NM}{K + 1}, \tag{2.17}$$

which is commonly known as the Reed-Mallett-Brennan (RMB) rule [6]. In the special case where the number of training samples is twice the number of degrees of freedom (DOF), i.e., $K = 2NM$, the mean adaptive loss is approximately 3 dB. If the training data is not i.i.d., higher estimation losses may occur. We describe possible causes of this in Section 2.3.2.

2.3 Ground Clutter Characteristics

A critical aspect of GMTI is the mitigation of ground clutter interference. In this section, we present a method of modeling ground clutter returns as well as properties of ground clutter, particularly array-induced nonstationarity.

2.3.1 Ground Clutter Modeling

We model ground clutter returns using the iso-range patch model depicted in Fig. 2.8, which gives a clutter return of the form

$$\mathbf{c}_k = \sum_{m=1}^{N_a} \sum_{n=1}^{N_c} \mathbf{a}_{\text{s-t}}(m,n;k) \odot \mathbf{s}_{\text{s-t}}\left(f_{s/m,n}, f_{d/m,n};k\right), \tag{2.18}$$

where N_a is the number of ambiguous ranges, N_c is the number of clutter patches in each iso-range, $\mathbf{a}_{\text{s-t}}(m,n;k)$ is a random complex patch voltage vector calculated from the radar equation, $\odot$ is the Hadamard product, $f_{s/m,n}$ is the clutter patch spatial frequency, and $f_{d/m,n}$ is the clutter patch Doppler frequency, which can be calculated from the relation

$$f_{d/m,n} = \frac{2}{\lambda}\mathbf{v}_{\mathbf{p}}^T \mathbf{k}\left(\boldsymbol{\psi}_{m,n}\right) = \frac{2\left|\mathbf{v}_{\mathbf{p}}\right|}{\lambda}\cos(\alpha), \tag{2.19}$$

where $\mathbf{v}_{\mathbf{p}}$ is the platform velocity vector and α is the angle between the platform velocity vector and the clutter scatterer [25]. For convenience, we define the relative Doppler frequency as

$$f_r = \frac{f_d \lambda}{2\left|\mathbf{v}_{\mathbf{p}}\right|} = \cos(\alpha). \tag{2.20}$$

We divide each iso-range in both azimuth and range such that any two adjacent patches have clutter Dopplers that differ by less than the Doppler resolution, $f_{d,res} = \frac{1}{NT}$ [25, 27].

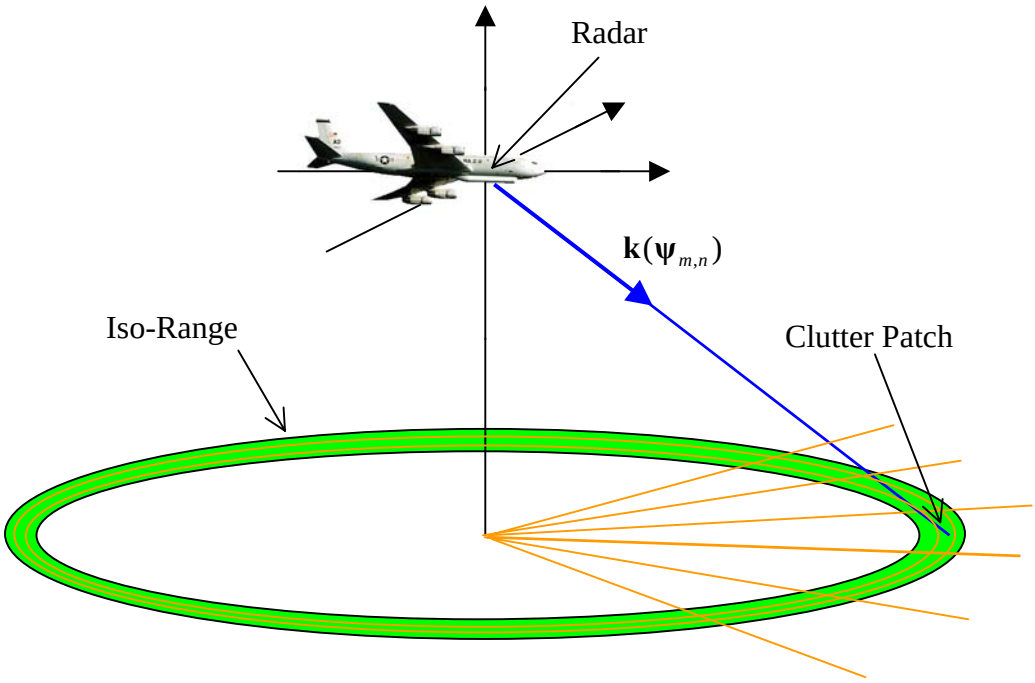

Figure 2.8. Ground clutter model indicating clutter patches for a single iso-range.

The multi-channel airborne radar measurements (MCARM) program collected data to examine the performance potential of STAP [28]. To justify the form of this ground clutter model, we compare the MVDR angle-Doppler spectra for the measured MCARM data and simulated data in Fig. 2.9. We see acceptable agreement between the measured data spectra and the simulated data spectra. Some of the angular spreading of the measured data is likely due to radome multi-path reflections and near-field scattering effects, not accounted for in the simulation [25, 27].

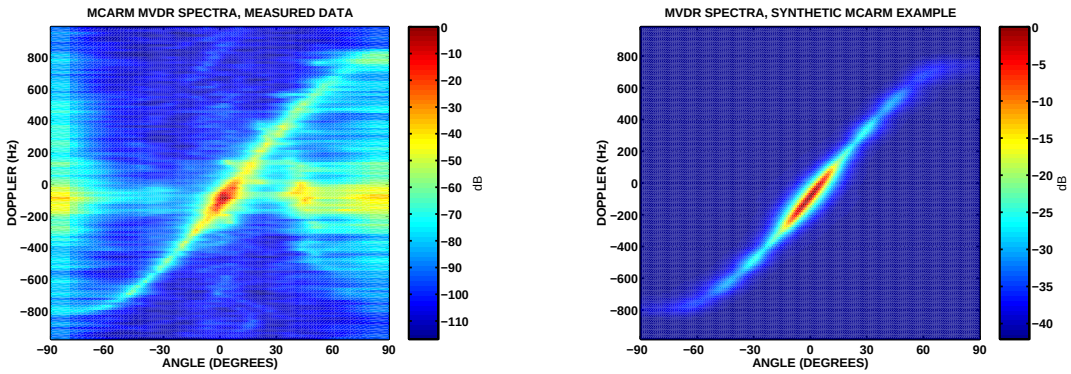

Figure 2.9. Comparison of MVDR spectra for measured MCARM data (left) and simulation (right).

2.3.2 Clutter Nonstationarity

As previously stated in Section 2.2, an accurate space-time covariance matrix estimate requires i.i.d. training data. If the training data is not iid, which may result from either clutter heterogeneity [29-34] or array-induced clutter nonstationarity [17-19, 35-37], higher adaptive losses may occur. Clutter heterogeneity refers to changing clutter properties, e.g., reflectivity, over the training region. Array-induced clutter nonstationarity, on the other hand, refers to changing clutter properties as seen by the array, e.g., Doppler and angle, over the training region.

To describe the issue of clutter nonstationarity further, we take a look at isodops (lines of constant clutter Doppler) and beam traces (lines of constant array properties). From (2.20), we can generate hyperbolas of constant clutter Doppler, called isodops, as shown in Fig. 2.10 [2]. Each isodop corresponds to a set of locations on the ground where α, the angle between the platform velocity vector and the clutter scatterer, is constant. The orientation of the isodops depends only on the platform's velocity. Similarly, any linear array has a cone ambiguity surface as previously shown in Fig. 2.4.

All points on a cone have the same spatial steering vector and thus the same properties as seen by the array. When projected onto a flat ground plane, these form hyperbolas called beam traces as shown in Fig 2.11 for a side-looking ULA. The orientation of the beam traces depends only on the linear array's orientation and not on the platform's velocity.

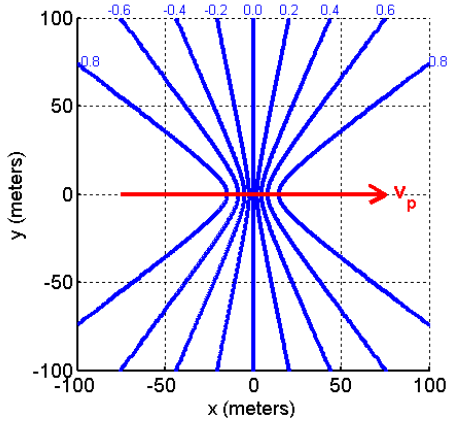

Figure 2.10. Isodops at varying relative Doppler frequencies for a given platform velocity.

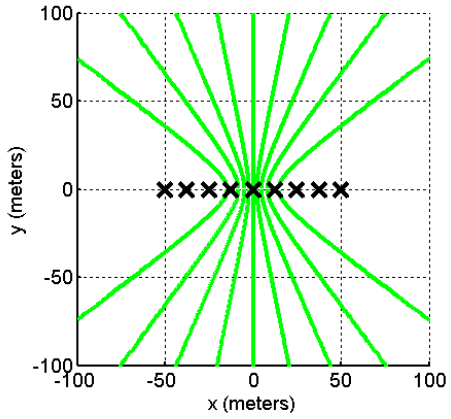

Fig 2.11. Beam traces for a side-looking array orientation.

In the case of a side-looking linear array, where the array normal is perpendicular to the platform velocity vector, the isodops and beam traces align perfectly as shown in Fig. 2.12. This is the stationary case, where the clutter's angle-Doppler properties as seen by

the array are constant with range. If we rotate the array 10° forward, so the crab angle between the array normal and the velocity vector is 80°, the isodops and beam traces begin to misalign as shown in Fig. 2.13. If we continue rotating the array to a forward-looking orientation, where the array normal and platform velocity vector are aligned, the isodops and beam traces become severely misaligned as shown in Fig. 2.14. These two later cases are nonstationary, so the clutter's angle-Doppler properties as seen by the array vary with range.

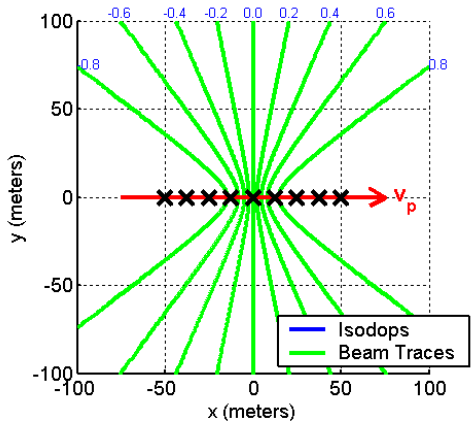

Figure 2.12. Aligned isodops and beam traces for a side-looking linear array indicating the clutter returns for this array are stationary.

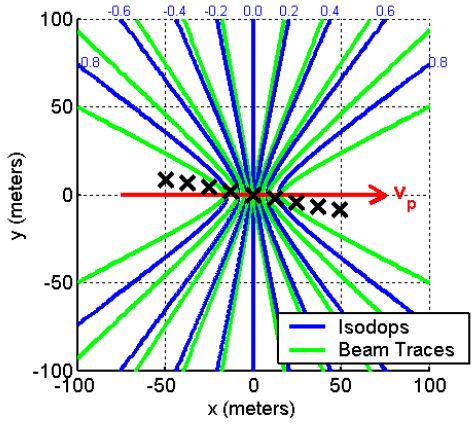

Figure 2.13. Slightly misaligned isodops and beam traces for a 10°-rotated linear array indicating the clutter returns for this array are nonstationary.

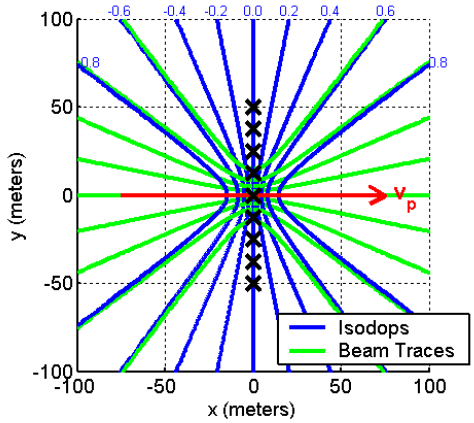

Figure 2.14. Severely misaligned isodops and beam traces for a forward-looking linear array indicating the clutter returns for this array are nonstationary.

From the isodops and beam traces, we can generate the clutter ridge plots shown in Figs. 2.15-2.17 [2]. These plots show the clutter's angle-Doppler profile for a given range. For the side-looking linear array (crab angle of 90°), the clutter ridge is linear and unchanging for all range, which again indicates the clutter returns from this array are stationary. For the linear array at a crab angle of 80°, the clutter ridge is elliptical and varies slightly with range. For the forward-looking array (crab angle of 0°), the clutter ridge is circular with a radius that varies greatly with range. This plot shows that the clutter's nonstationary behavior is greater at close range where the clutter ridge varies significantly from 15 km to 30 km. At longer ranges, (45-75 km), the clutter ridges begin to align as the clutter becomes more stationary.

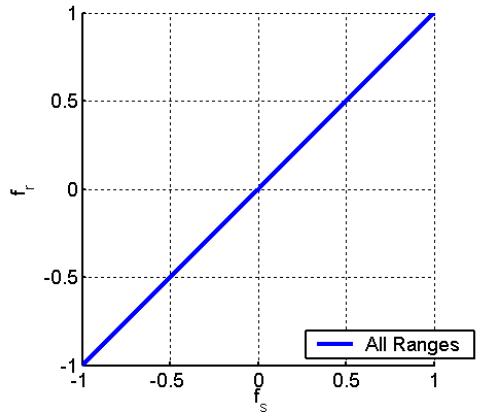

Figure 2.15. Clutter ridge for a side-looking linear array.

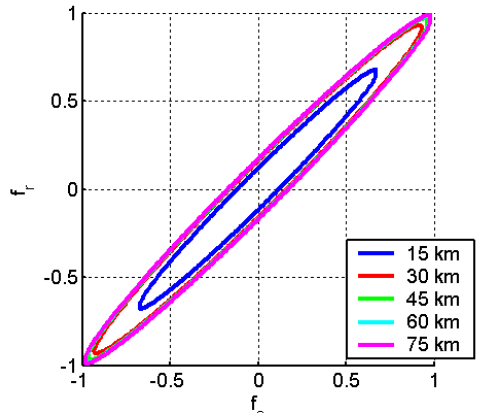

Figure 2.16. Clutter ridges for a 10° rotated linear array.

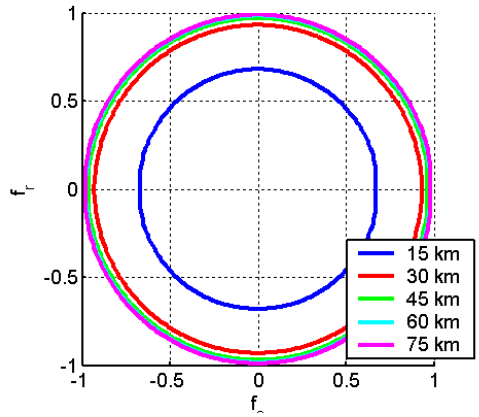

Figure 2.17. Clutter ridges for a forward-looking linear array.

In general, nonlinear arrays, including conformal arrays, have no ambiguity surfaces and thus have no beam traces with constant array properties. As a result, clutter returns from nonlinear arrays are inherently nonstationary. The degree of nonstationarity varies depending on the array geometry, which we discuss in greater detail in Chapter 4.

CHAPTER 1

INTRODUCTION

1.1 STAP Overview

STAP is well documented throughout the literature, including several recent texts [1-4] and many classic papers [5-7]. The fundamental function of STAP is to design a multidimensional (temporal and spatial) optimal filter to cancel clutter, jamming and other interference, thereby improving target detection. STAP is most commonly applied to airborne radar and is a necessity for weak or slow-moving ground target detection [3].

STAP is currently applied in the E-8C Joint Surveillance Target Attack Radar System (JointSTARS) shown in Fig. 1.1. This radar system consists of a 7.3 m long side-looking planar array housed in a canoe-shaped radome mounted on the forward fuselage of a Boeing 707-300 aircraft. The array can mechanically rotate 60° to control look direction and can detect ground-moving targets at distant ranges up to 250 km [8].

Figure 1.1. JointSTARS radar system mounted on the underside of a Boeing 707 aircraft.

1.2 Motivation for Conformal Arrays

It is desirable to mount large-aperture arrays on smaller platforms such as unmanned aerial vehicles (UAVs) and fighter aircraft shown in Fig. 1.2. The large size and weight of the JointSTARS array make it impractical for these applications. Conformal arrays offer a possible solution to this problem.

Figure 1.2. Global Hawk UAV (center) and Joint Strike Fighter (right).

Conformal array antennas assume the shape of the radar-bearing platform and generally belong to the class of nonlinear arrays. Conformal arrays offer many advantages over conventional planar arrays including the following:

- Conformal arrays provide aerodynamic shape compatible with the corresponding airframe.
- The conformal design yields potentially greater effective aperture for the same class of platform.
- Conformal arrays reduce payload weight. No rigid support structure or radome is necessary.

- A conformal antenna design can provide 360^o of surveillance coverage without mechanically canting or rotating the array.
- Conformal arrays offer improved flexibility when integrating diverse sensor functions. A system resource allocator can assign different functions – such as moving target indication, spoofing, synthetic aperture imaging or communications – to different physical locations on the conformal antenna.

In general, conformal arrays have nonuniform element spacing and a nonplanar shape. Many complications arise as a result of these factors including the following:

- The loss of certain desirable beampattern characteristics.
- Array-induced clutter nonstationarity.
- A nonuniform-magnitude spatial steering vector.

These complications can severely degrade the performance of conventional STAP algorithms, requiring the development of novel conformal array STAP techniques.

1.3 Conformal Array Literature

The majority of the conformal array literature relates to radiation-pattern synthesis [9-12]. These authors use a variety of techniques to place elements on a conformal surface, given constraints on the radiation pattern. Sidelobe optimization for special classes of conformal arrays is also a topic of interest [13], as well as the polarimetric response of a conformal array [14-16]. The main conformal array STAP contribution to the literature is for the special case of circular arrays [17-22]. In [17], a horizontally mounted circular array's performance is compared with the performance of a uniform linear array (ULA).

The circular array results show significant nonstationarity. Reduced-dimension STAP techniques and time-varying weights are proposed as a possible solution and are further analyzed.

1.4 Contributions

This thesis makes the following contributions:

- Development of a conformal array signal model, which includes element normal concerns, a novel general subarraying technique, and a conformal array clutter simulation algorithm.
- Derivation of the conformal array matched filter.
- Performance analysis of existing STAP techniques (conventional, localized training, time-varying weights) on mitigating conformal-array nonstationary clutter.
- Application of equivalent-ULA techniques to conformal arrays.
- Development of novel theoretical and adaptive angle-Doppler compensation techniques for conformal arrays.
- Analysis of the effect of array errors on conformal array performance and a potential array calibration techniques.

1.5 Thesis Outline

In this thesis, we present the application of conformal arrays to STAP, concentrating on the mitigation of ground clutter returns. In Chapter 2 we present the fundamentals of STAP for a ULA. We include an explanation of radar fundamentals, STAP performance

metrics, and ground clutter characteristics. In Chapter 3 we extend the STAP fundamentals to the conformal array case in our development of a conformal array signal model. In this modeling we include considerations of element placement and normal definition, the polarimetric response, subarraying, ground clutter returns, the conformal array matched filter, and array errors. In Chapter 4 through conformal array clutter simulations, we analyze the performance of conventional and more advanced STAP algorithms. We find that the conformal array's nonlinear geometry and non-side-looking orientation induce nonstationary clutter returns, which severely degrade adaptive performance. In Chapter 5 we investigate equivalent-ULA techniques as a possible solution to the conformal-array nonstationary clutter returns. In Chapter 6 we develop novel theoretical and adaptive angle-Doppler compensation techniques, which align nonstationary clutter returns. Finally, in Chapter 7 we investigate the impact of array errors on adaptive performance and propose potential array calibration techniques.

CHAPTER 3

CONFORMAL ARRAY MODELING

3.1 Modeling Overview

Conformal arrays assume the shape of the radar-bearing platform. This nonlinearity causes many modeling challenges including the following:

- The placement and spacing of elements on the conformal surface;
- The definition and influence of varying element normals;
- The polarimetric response of the array;
- The grouping of elements into subarrays;
- The conformal array matched filter (spatial steering vector); and,
- The modeling of array errors.

In this chapter we consider these factors as they relate to both the geometry model and signal model. We develop a method to place elements on a conformal surface as well as calculate the element normals. We also develop a conformal array target model and apply it to an existing validated clutter model to generate a novel conformal clutter model. We derive the spatial matched filter for the conformal array case, allowing for array element and normal errors. Finally, we define a set of performance metrics, which we use to characterize a conformal array's response and adaptive performance.

3.2 Geometry Model

We define conformal surfaces using parallel slices, which allows for easier element placement on the surface. Figure 3.1 shows example chined and airfoil conformal surfaces. The linearly tapered airfoil surface requires two parallel slices whereas the more complicated chined surface requires twenty-three parallel slices for an accurate surface definition.

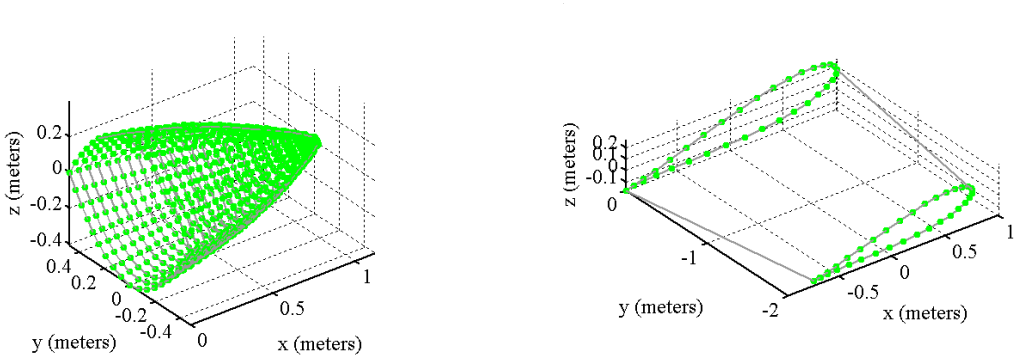

Figure 3.1. Example chined and airfoil conformal surfaces.

We define surface normals for all surface definition points on all surface slices. The surface normals can either be individually defined, as shown for the chined radome in Fig. 3.2 or calculated from the given surface as shown for the airfoil in Fig. 3.3. We calculate the normals for a surface point by averaging the linear normals between that point and all adjacent points. Figure 3.4 illustrates a simplified 2-D version of this procedure.

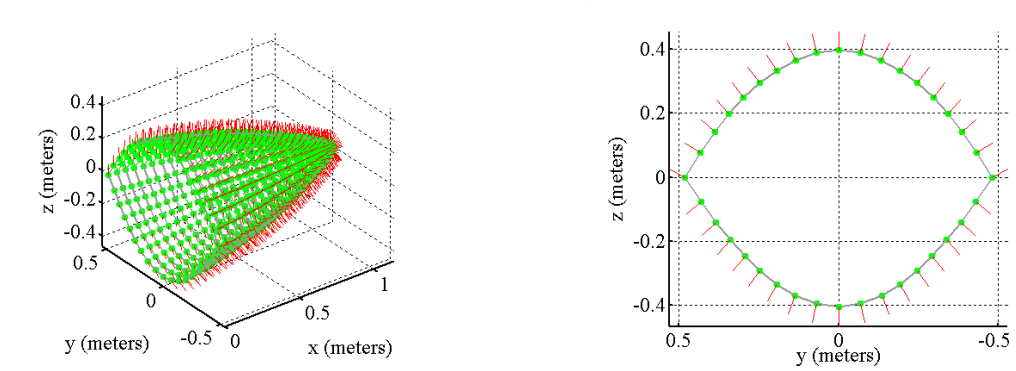

Figure 3.2. Chined conformal surface with individually defined surface normals.

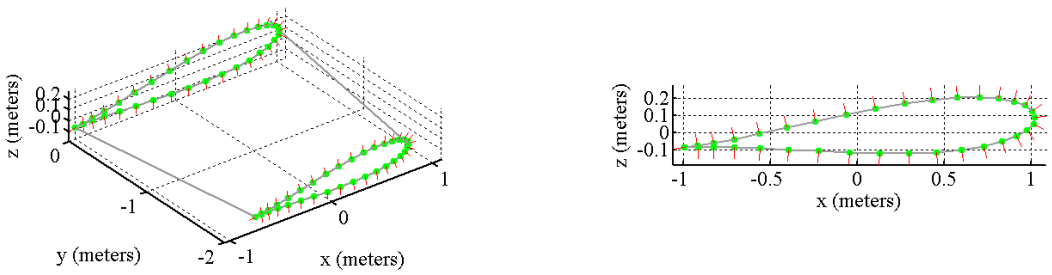

Figure 3.3. Airfoil conformal surface with calculated surface normals.

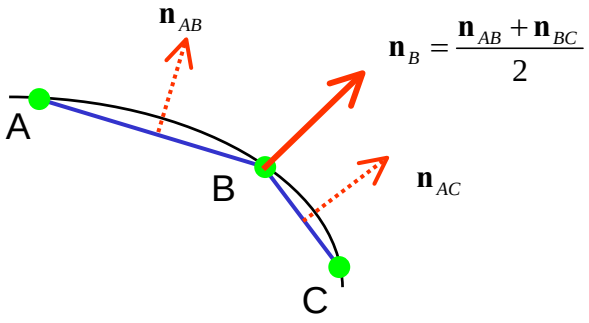

Figure 3.4. Illustration of 2-D surface-normal calculation procedure.

After fully defining surfaces and normals, we calculate positions and normals for new slices at a specified spacing (typically $\lambda/2$) by linearly interpolating between the nearest-neighbor surface slices. Next, we place elements on the new interpolated slice by moving at increments of a specified spacing along the surface of the slice, linearly interpolating between the nearest points on the slice to obtain both the element position and the normal. Figures 3.5 and 3.6 show example element positions and normals for the chined and airfoil conformal arrays, respectively.

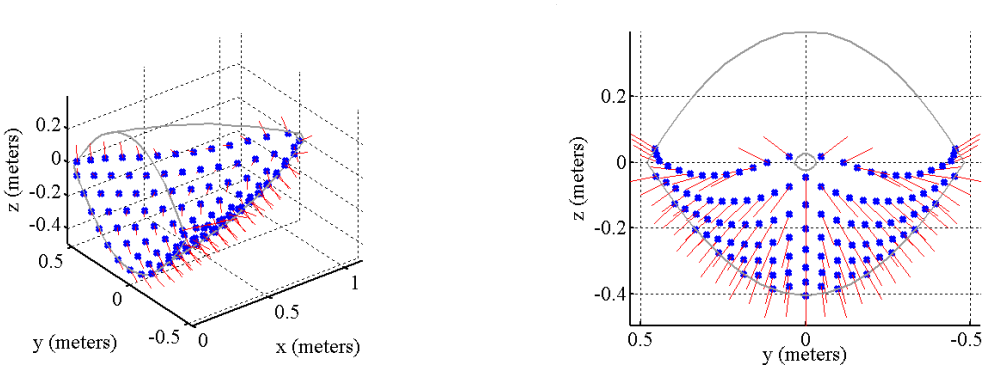

Figure 3.5. Element placement on the chined conformal surface.

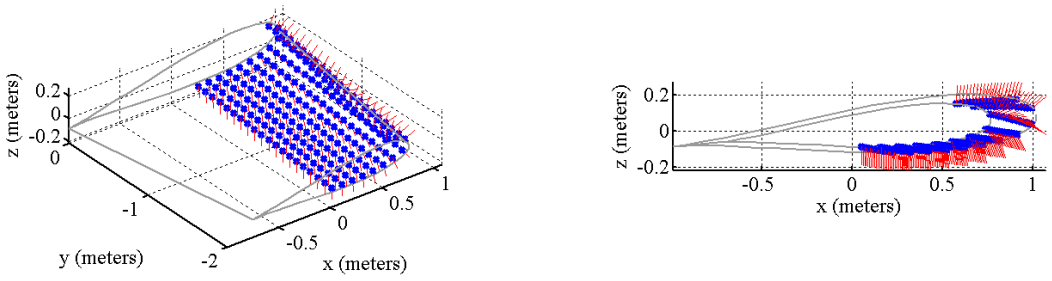

Figure 3.6. Element placement on the airfoil conformal surface.

3.3 Element Model

3.3.1 Element Pattern

Element normals can vary greatly for conformal arrays, as previously shown in Figs. 3.5 and 3.6. As a result, we must take special care in defining the appropriate element gains. We assume all elements have a cosine-squared pattern such that

$$g_{e/m}(\alpha_m) = \begin{cases} g_0 \cos^2\left(\alpha_m \dfrac{\pi}{\theta_{null}}\right) & -\dfrac{\pi}{2} \le \alpha_m \le \dfrac{\pi}{2} \\ g_b g_0 \cos^2\left(\alpha_m \dfrac{\pi}{\theta_{null}}\right) & \dfrac{\pi}{2} < \alpha_m < \dfrac{3\pi}{2} \end{cases}, \tag{3.1}$$

where g_0 is the peak element gain, $\alpha_m = \cos^{-1}\left(\mathbf{n}_{\mathbf{e}/m} \cdot \mathbf{k}(\boldsymbol{\psi})\right)$ is the angle between the element normal $\mathbf{n}_{\mathbf{e}/m}$ and the pointing vector $\left(\mathbf{k}(\boldsymbol{\psi})\right)$, θ_{null} is the beamwidth between the nulls and g_b is the backlobe attenuation.

Figure 3.7 shows the effect of the varying element normals for three neighboring elements of an example airfoil conformal array. As a result of the airfoil's severe curvature, the element patterns vary greatly from one element to another.

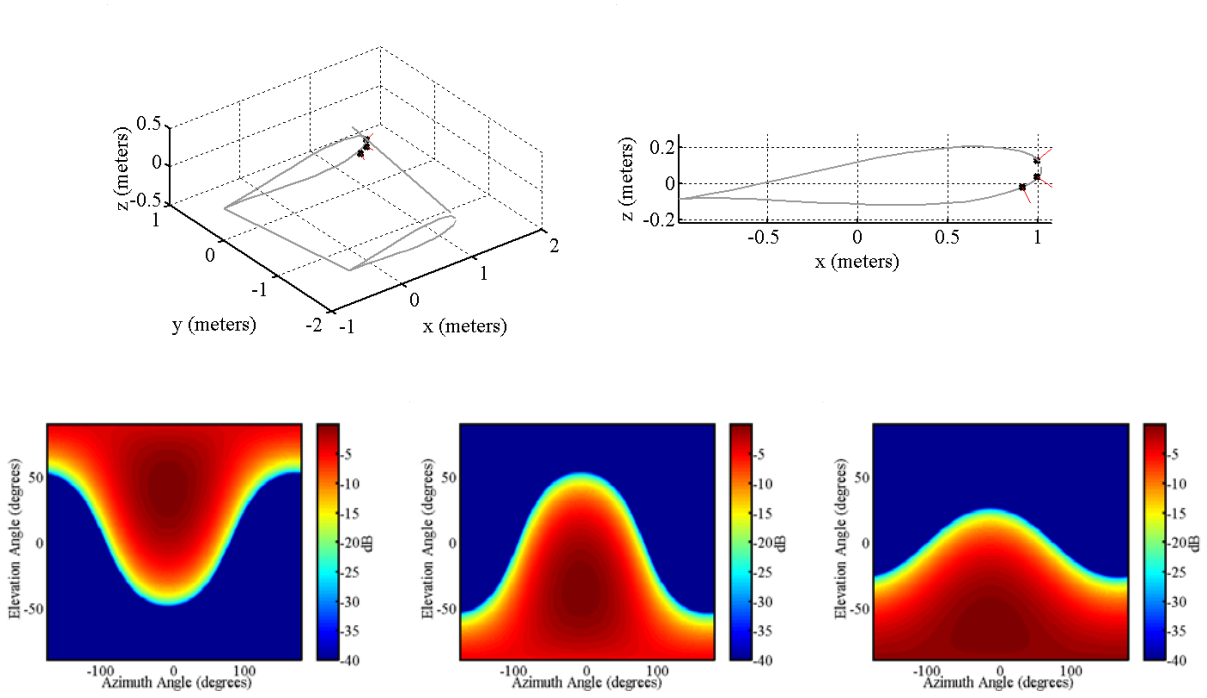

Figure 3.7. 3-D element patterns for the adjacent elements on the example airfoil surface.

3.3.2 Polarization

As a result of the varying normals, elements exhibit unique polarization dependence, which may result in additional gain mismatch. The polarization-dependent gain is

$$\bar{g}_{e/m}(\alpha_m) = g_{H/m}(\alpha_m)\hat{\mathbf{h}} + g_{V/m}(\alpha_m)\hat{\mathbf{v}}, \tag{3.2}$$

where $g_{H/m}(\alpha_m)$ and $g_{V/m}(\alpha_m)$ are the element gains for horizontal and vertical polarizations and $\hat{\mathbf{h}}$ and $\hat{\mathbf{v}}$ are the horizontal and vertical basis vectors. Approximations for $g_{H/m}(\alpha_m)$ and $g_{V/m}(\alpha_m)$ take the form of (3.1) with appropriate adjustments to the maximum gain g_0 [27]. The receive voltage for a given target at element m has the form

$$\begin{aligned} v_{R/m} &= \eta \bar{\mathbf{g}}_{\mathbf{e}/m}^T \mathbf{P}_\mathbf{T} \mathbf{t}_\mathbf{t}; \\ \bar{\mathbf{g}}_{\mathbf{e}/m}^T &= \left[g_{H/m}(\alpha_m) \quad g_{V/m}(\alpha_m) \right]^T, \end{aligned} \tag{3.3}$$

where η is a complex random variable, $\mathbf{P_T}$ is the target polarization scattering matrix, and $\mathbf{t_t}$ describes the polarization properties of the transmit waveform. Hence, three factors influence the receive voltage, the polarimetric scattering characteristics of the target, the transmit polarization, and the receive polarization at each element. We can accommodate the impact of each element's polarization dependence for a given target class by substituting a unique gain factor in (3.1).

In the literature, many authors have investigated the impact of polarization on conformal arrays [14-16]. Polarization mismatch creates additional losses, which in turn burdens adaptive performance. Optimizing the polarimetric response is generally considered an antenna design problem independent from the adaptive processing. So as not to detract from our primary objective of optimizing adaptive performance, we assume a uniform polarimetric response across the elements.

3.3.3 Array Pattern

We define the narrowband beampattern for a general array as

$$E(\boldsymbol{\psi}) = \sum_{m=1}^{M_e} w_m e^{j\mathbf{k_w}(\boldsymbol{\psi})\cdot\mathbf{d}_{\mathbf{e}/m}} \sqrt{g_{e/m}(\boldsymbol{\psi})} \tag{3.4}$$

where M_e is the total number of elements, w_m is a complex weight applied to element m, $\mathbf{k_w}(\boldsymbol{\psi}) = (2\pi/\lambda)\mathbf{k}(\boldsymbol{\psi})$ is the wavenumber vector, $\mathbf{d}_{\mathbf{e}/m}$ is the element position vector, and $g_{e/m}(\boldsymbol{\psi})$ is the element gain [38]. For a ULA or a planar array, we can separate the element pattern (EP), subarray factor (SAF), and array factor (AF) such that

$$E(\boldsymbol{\psi}) = \sqrt{g_e(\boldsymbol{\psi})} \sum_{m=1}^{M_{e,sa}} w_m e^{j\mathbf{k_w}(\boldsymbol{\psi})\cdot\mathbf{d}_{\mathbf{e}/m}} \sum_{n=1}^{M} w_n e^{j\mathbf{k_w}(\boldsymbol{\psi})\cdot\mathbf{d}_{\mathbf{sa}/n}}, \tag{3.5}$$

and

$$P(\boldsymbol{\psi}) = \mathrm{EP}(\boldsymbol{\psi}) \cdot \mathrm{SAF}(\boldsymbol{\psi}) \cdot \mathrm{AF}(\boldsymbol{\psi}) \tag{3.6}$$

where $M_{e,sa}$ is the number of elements in each subarray and $\mathbf{d}_{\mathbf{sa}/n}$ is the phase center of subarray n [23].

For conformal arrays, we cannot simplify the array pattern in this manner since both elements patterns and subarray patterns vary. As a result, we must perform all modeling at the element level.

3.4 Space-Time Target Model

3.4.1 Element SNR

We define the SNR for a point target at range k and element m as

$$\mathrm{SNR}_{k,m} = \left(\frac{P_t G_t(\boldsymbol{\psi})}{4\pi R_{T/k}^2} \right) \left(\frac{\sigma_T}{4\pi R_{T/k}^2} \right) \left(\frac{\lambda^2}{4\pi k_B T_s B_r} \right) G_{sp} g_{e/m}, \tag{3.7}$$

where P_t is the transmit power, G_t is the active aperture transmit gain in the direction of interest, $R_{T,k}$ is the target slant range, σ_T is the target radar cross section, k_B is Boltzman's constant, T_s is the system temperature, B_T is the receiver bandwidth, and G_{sp} is the signal processing gain [23]. For convenience, we define a random element-independent voltage

$$v_k = \varsigma \sigma_n \sqrt{\frac{\mathrm{SNR}_{k,m}}{g_{e/m}}} = \varsigma \sigma_n \sqrt{\left(\frac{P_t G_t(\boldsymbol{\psi})}{4\pi R_{T/k}^2} \right) \left(\frac{\sigma_T}{4\pi R_{T/k}^2} \right) \left(\frac{\lambda^2}{4\pi k_B T_s B_r} \right) G_{sp}}, \tag{3.8}$$

where σ_n^2 is the output noise variance and ς is a complex Gaussian random variable with unity variance.

3.4.2 Spatial Snapshot and Subarraying

Accounting for the time delay between elements, we define the complex baseband receive signal as

$$r_{k,m} = v_k \sqrt{g_{e/m}} e^{j\mathbf{k}_w(\psi)\cdot\mathbf{d}_{e/m}}. \tag{3.9}$$

Expressing (3.9) in vector form gives the full-element spatial snapshot at range k as

$$\mathbf{x}_{e/k} = v_k \hat{\mathbf{g}}(\psi) \odot \mathbf{s}_s(\psi), \tag{3.10}$$

where

$$\hat{\mathbf{g}}(\psi) = \left[\sqrt{g_{e/1}} \quad \sqrt{g_{e/2}} \quad \cdots \quad \sqrt{g_{e/M_e}} \right]^T \tag{3.11}$$

is a vector of element gains, and

$$\mathbf{s}_s(\psi) = \left[e^{j\mathbf{k}(\psi)\cdot\mathbf{d}_{e/1}} \quad e^{j\mathbf{k}(\psi)\cdot\mathbf{d}_{e/2}} \quad \cdots \quad e^{j\mathbf{k}(\psi)\cdot\mathbf{d}_{e/M_e}} \right]^T \tag{3.12}$$

is the conventional spatial steering vector [27].

In (3.10), we assume the narrowband approximation holds, and that we have perfect element-to-element correlation. The validity of this approximation depends on the array size, direction of arrival (DOA), and fractional bandwidth [39]. Given a bandlimited receive waveform, we define the spatial correlation between elements m and n as

$$\rho_s(m,n) = \mathrm{sinc}\left(\pi B_r \left(\tau_{e/m} - \tau_{e/n}\right)\right). \tag{3.13}$$

where B_r is the receiver bandwidth and $\tau_{e/m} = \dfrac{\mathbf{k}(\psi)\cdot\mathbf{d}_{e/m}}{c}$ is the time delay to element m. Adding this decorrelation effect to (3.10) gives the new full-element spatial snapshot as

$$\mathbf{x}_{e/k} = v_k \hat{\mathbf{g}}(\psi) \odot \mathbf{a}_s \odot \mathbf{s}_s(\psi), \tag{3.14}$$

where $\mathbf{a_s}$ is a random vector with spatial correlation matrix

$$\mathbf{A_s} = E\left[\mathbf{a_s}\mathbf{a_s}^H\right] = \begin{bmatrix} \rho_s(1,1) & \rho_s(1,2) & \dots & \rho_s(1,M_e) \\ \rho_s(2,1) & \rho_s(2,2) & \dots & \rho_s(2,M_e) \\ \vdots & \vdots & \ddots & \vdots \\ \rho_s(M_e,1) & \rho_s(M_e,2) & \dots & \rho_s(M_e,M_e) \end{bmatrix}. \tag{3.15}$$

Subarraying involves the weighting and summing of specified groupings of elements. Element groupings can be exclusive, or the subarrays can share elements (overlapped subarrays). As previously discussed, ULAs and planar arrays can be broken into subarrays so that all subarrays share a common array pattern so that we only need to simulate at the subarray level. Conformal arrays, on the other hand, require simulations at the element level followed by the coherent grouping of elements into subarrays. The subarray spatial snapshot then follows as

$$\mathbf{x_{s}}_{/k} = \mathbf{T}^H \mathbf{x_e}_{/k} = \left[\left[\mathbf{x_s}_{/k}\right]_1 \quad \left[\mathbf{x_s}_{/k}\right]_2 \quad \dots \quad \left[\mathbf{x_s}_{/k}\right]_M\right]^T, \tag{3.16}$$

where $\mathbf{T} \in C^{M_e x M}$ is a linear operator summing the elements into M subarrays with appropriate steering phase weightings; $w_{ps/m} = e^{j\mathbf{k_w}(\boldsymbol{\psi}_{\mathbf{ps}})\cdot\mathbf{d_e}_{/m}}$ is the mth weight for pre-steer direction $\boldsymbol{\psi}_{\mathbf{ps}}$. We denote $\mathbf{T}$ as the subarray transformation matrix.

We illustrate the function of the subarray transformation matrix using the five-element ULA shown in Fig. 3.8. In the first case, we form two nonoverlapping subarrays pre-steered broadside to the array. In the second case, we again form two nonoverlapping subarrays, but now pre-steer at an angle of ϕ_{ps}. In the third case, we form two overlapping subarrays and again pre-steer at an angle of ϕ_{ps}.

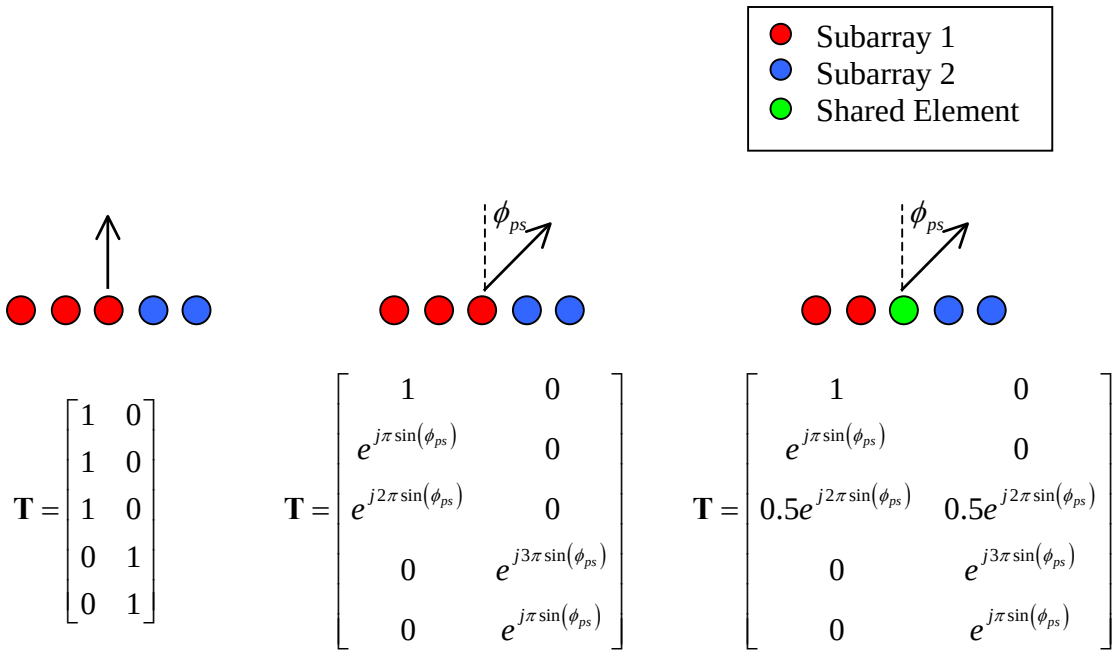

Figure 3.8. Example subarraying schemes and corresponding transformation matrices for a five-element ULA.

As a final note, we derive the target spatial covariance matrix at range k as

$$\mathbf{R}_{\mathbf{s}/k} = E\left[\mathbf{x}_{\mathbf{s}/k}\mathbf{x}_{\mathbf{s}/k}^H\right] = \tilde{\sigma}_s^2\mathbf{T}^H\left(\mathbf{A}_\mathbf{s} \odot \hat{\mathbf{g}}\hat{\mathbf{g}}^H \odot \mathbf{s}_\mathbf{s}\mathbf{s}_\mathbf{s}^H\right)\mathbf{T}, \tag{3.17}$$

where $\tilde{\sigma}_s^2 = E\left[\left|v_k^2\right|\right]$.

3.4.3 Temporal Snapshot

The Doppler steering vector describes the pulse-to-pulse phase change resulting from platform and target motion. We define the Doppler steering vector as

$$\mathbf{s}_\mathbf{t} = \left[1 \quad e^{j2\pi f_d T} \quad e^{j2\pi 2 f_d T} \quad \ldots \quad e^{j2\pi(N-1) f_d T}\right], \tag{3.18}$$

where $f_d = \dfrac{2\mathbf{k}\left(\boldsymbol{\psi}_\mathbf{s}\right)\cdot\left(\mathbf{v}_\mathbf{p} - \mathbf{v}_\mathbf{s}\right)}{\lambda}$ is the Doppler frequency of a scatterer at angle $\boldsymbol{\psi}_\mathbf{s}$ moving with velocity $\mathbf{v}_\mathbf{s}$. We model the temporal snapshot at element m as

$$\mathbf{x}_{\mathbf{t}/k}(m) = v_k \sqrt{g_{e/m}} \left(\mathbf{a}_{\mathbf{t}} \odot \mathbf{s}_{\mathbf{t}}(f_d) \right), \tag{3.19}$$

where $\mathbf{a}_{\mathbf{t}}$ is a random vector with temporal correlation matrix

$$\mathbf{A}_{\mathbf{t}} = E\left[\mathbf{a}_{\mathbf{t}} \mathbf{a}_{\mathbf{t}}^H \right] = \text{Toeplitz}\left(\rho_I(0), \rho_I(1), \rho_I(2), \ldots, \rho_I(N-1) \right) \tag{3.20}$$

with autocorrelation coefficient $p_I(m)$ at lag m. Common choices for the autocorrelation function shape include Gaussian [23] and exponential [40]. Finally, the temporal covariance matrix for element m at range k is

$$\mathbf{R}_{\mathbf{t}/k}(m) = E\left[\mathbf{x}_{\mathbf{t}/k}(m) \mathbf{x}_{\mathbf{t}/k}^H(m) \right] = \tilde{\sigma}_s^2 g_{e/m} \mathbf{A}_{\mathbf{t}} \odot \mathbf{s}_{\mathbf{t}} \mathbf{s}_{\mathbf{t}}^H . \tag{3.21}$$

3.4.4 Space-Time Snapshot

Combining the spatial and temporal snapshots, we define the space-time snapshot at range k with Doppler f_d and angle $\boldsymbol{\psi}$ as

$$\mathbf{x}_k = v_k \left(\mathbf{a}_{\mathbf{t}} \odot \mathbf{s}_{\mathbf{t}}(f_d) \right) \otimes \left(\mathbf{T}^H \left(\mathbf{a}_{\mathbf{s}} \odot \hat{\mathbf{g}} \odot \mathbf{s}_{\mathbf{s}}(\boldsymbol{\psi}) \right) \right), \tag{3.22}$$

and the corresponding space-time covariance matrix is

$$\mathbf{R}_k = E\left[\mathbf{x}_{\mathbf{k}} \mathbf{x}_{\mathbf{k}}^H \right] = \tilde{\sigma}_s^2 \left(\mathbf{A}_{\mathbf{t}} \odot \mathbf{s}_{\mathbf{t}} \mathbf{s}_{\mathbf{t}}^H \right) \otimes \left(\mathbf{T}^H \left(\mathbf{A}_{\mathbf{s}} \odot \hat{\mathbf{g}} \hat{\mathbf{g}}^H \odot \mathbf{s}_{\mathbf{s}} \mathbf{s}_{\mathbf{s}}^H \right) \mathbf{T} \right). \tag{3.23}$$

3.5 *Ground Clutter Model*

We model ground clutter returns using the iso-range patch model depicted in Fig. 3.9, which has been validated for the ULA case as described in Chapter 2. For the conformal array case, we apply the necessary updates to this model to give a clutter return of the form

$$\mathbf{c}_k = \sum_{m=1}^{N_a}\sum_{n=1}^{N_c} v_k\left(\boldsymbol{\psi}_{m,n}\right)\left[\mathbf{a}_\mathbf{t}\left(f_d\left(\boldsymbol{\psi}_{m,n}\right)\right)\odot\mathbf{s}_\mathbf{t}\left(f_d\left(\boldsymbol{\psi}_{m,n}\right)\right)\right]\otimes\left[\mathbf{T}^H\left(\mathbf{a}_\mathbf{s}\left(\boldsymbol{\psi}_{m,n}\right)\odot\hat{\mathbf{g}}\left(\boldsymbol{\psi}_{m,n}\right)\odot\mathbf{s}_\mathbf{s}\left(\boldsymbol{\psi}_{m,n}\right)\right)\right]. \tag{3.24}$$

This new model accounts for the varying element and subarray gains inherent in conformal array geometries. Just as before in the ULA model, we sample each iso-range in both azimuth and range at the Doppler Nyquist rate, accounting for ambiguous range returns.

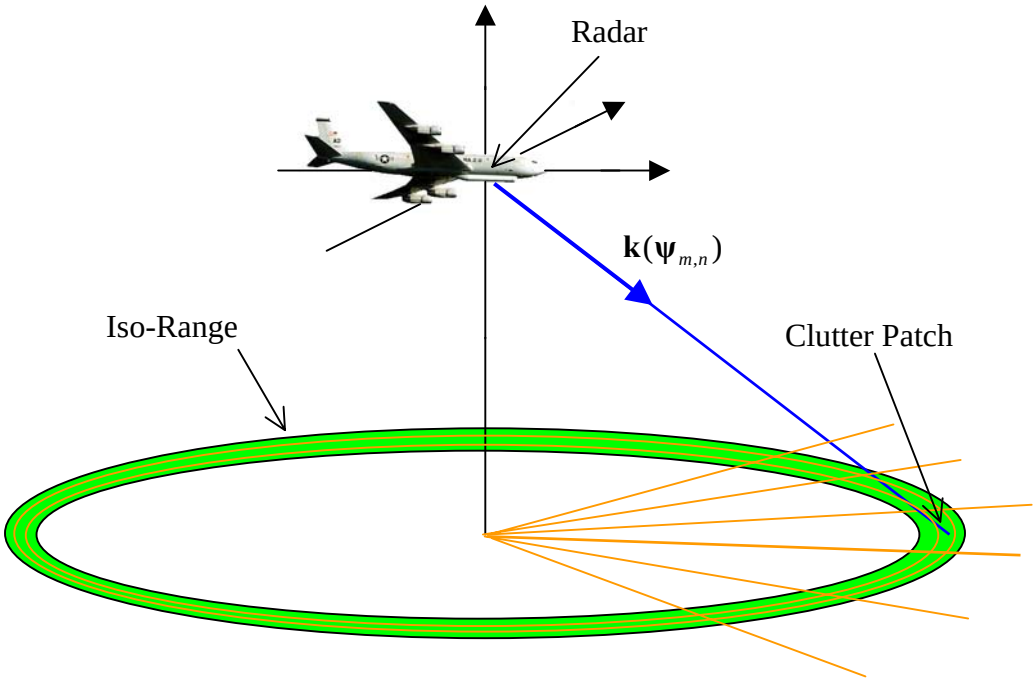

Figure 3.9. Ground clutter model indicating clutter patches for a single iso-range.

3.6 Conformal-Array Matched Filter

For conventional STAP, the spatial matched filter is the spatial steering vector, $\mathbf{s}_s$, corresponding to the subarray phase centers. For conformal arrays, this formulation does not hold due to the varying element and subarray gains. In this section, we derive the matched filter for the conformal array case and illustrate it further with an example conformal array.

3.6.1 Spatial-Matched-Filter Formulation

We derive the conformal array spatial matched filter as the filter that maximize SNR in the presence of both sky and receiver noise. We assume that both noise sources are Gaussian, and the sky noise is spatially white over all elements, while receiver noise is spatially white over all subarrays. A spatial snapshot at the element level with the addition of sky noise is

$$\mathbf{y}_\mathbf{e} = \mathbf{x}_\mathbf{e} + \mathbf{n}_\mathbf{s}, \tag{3.25}$$

and a spatial snapshot at the subarray level with the addition of both sky noise and receiver noise is

$$\mathbf{y}_\mathbf{s} = \mathbf{T}^H \mathbf{y}_\mathbf{e} + \mathbf{n}_\mathbf{r} = \mathbf{T}^H \mathbf{x}_\mathbf{e} + \mathbf{T}^H \mathbf{n}_\mathbf{s} + \mathbf{n}_\mathbf{r}, \tag{3.26}$$

where $\mathbf{n}_\mathbf{s}$ is a length M_e vector and $\mathbf{n}_\mathbf{r}$ is a length M vector. The corresponding spatial covariance matrix is

$$\mathbf{R}_{\mathbf{y}_\mathbf{s}} = E\left[\mathbf{y}_\mathbf{s}\mathbf{y}_\mathbf{s}^H\right] = \mathbf{T}^H \mathbf{x}_\mathbf{e}\mathbf{x}_\mathbf{e}^H \mathbf{T} + \sigma_{n_s}^2 \mathbf{T}^H \mathbf{T} + \sigma_{n_r}^2 \mathbf{I}, \tag{3.27}$$

where $\sigma_{n_s}^2$ and $\sigma_{n_r}^2$ are the sky and white noise powers. Finally, we define SNR as

$$\text{SNR} = \frac{\mathbf{w}^H \mathbf{R}_s \mathbf{w}}{\mathbf{w}^H \left(\sigma_{n_s}^2 \mathbf{T}^H \mathbf{T} + \sigma_{n_r}^2 \mathbf{I} \right) \mathbf{w}} . \tag{3.28}$$

We solve this optimization problem using the Rayleigh quotient as described in [24]. For convenience, we define a Hermitian matrix

$$\mathbf{B} = \sigma_{n_s}^2 \mathbf{T}^H \mathbf{T} + \sigma_{n_r}^2 \mathbf{I} , \tag{3.29}$$

and a modified weight vector

$$\tilde{\mathbf{w}} = \mathbf{B}^{1/2} \mathbf{w} . \tag{3.30}$$

Substituting into (3.28) gives

$$\text{SNR} = \frac{\tilde{\mathbf{w}}^H \mathbf{B}^{-1/2} \mathbf{R}_s \mathbf{B}^{-1/2} \tilde{\mathbf{w}}}{\tilde{\mathbf{w}}^H \tilde{\mathbf{w}}} . \tag{3.31}$$

From the Rayleigh quotient, we maximize SNR when $\tilde{\mathbf{w}}$ is the eigenvector corresponding to the maximum eigenvalue of $\mathbf{A} = \mathbf{B}^{-1/2} \mathbf{R}_s \mathbf{B}^{-1/2}$. For the narrowband case where $\rho_s = 1$, $\mathbf{A} = \tilde{\sigma}_s^2 \mathbf{B}^{-1/2} \mathbf{T}^H \left(\hat{\mathbf{g}} \odot \mathbf{s}_s \right) \left(\hat{\mathbf{g}} \odot \mathbf{s}_s \right)^H \mathbf{T} \mathbf{B}^{-1/2}$, and $\tilde{\mathbf{w}}_{\mathbf{max}} = \mathbf{B}^{-1/2} \mathbf{T}^H \left(\hat{\mathbf{g}} \odot \mathbf{s}_s \right)$. Substituting this result into (3.30), gives the matched filter

$$\mathbf{s}_{\mathbf{s,cfa}} = \mathbf{w}_{\mathbf{max}} = \mu \mathbf{B}^{-1} \mathbf{T}^H \left(\hat{\mathbf{g}} \odot \mathbf{s}_s \right) = \mu \left(\sigma_{n_s}^2 \mathbf{T}^H \mathbf{T} + \sigma_{n_r}^2 \mathbf{I} \right)^{-1} \mathbf{T}^H \left(\hat{\mathbf{g}} \odot \mathbf{s}_s \right), \tag{3.32}$$

where μ is an arbitrary constant. In the case of negligible sky noise, $\sigma_{n_s}^2 << \sigma_{n_r}^2$, the matched filter simplifies to

$$\mathbf{s}_{\mathbf{s,cfa}} = \mu \mathbf{T}^H \left(\hat{\mathbf{g}} \odot \mathbf{s}_s \right). \tag{3.33}$$

This result shows that the conformal-array matched filter is dependent not only upon the element phases $(\mathbf{s}_s)$, but also the element gains $(\hat{\mathbf{g}})$ and the general subarraying scheme $(\mathbf{T})$.

3.6.2 Spatial-Matched-Filter Gain

We choose the gain of the matched filter so that the inner product is consistent with the spatial steering vector in conventional STAP, i.e., $\mathbf{w}_{\mathbf{max}}^H \mathbf{w}_{\mathbf{max}} = \mathbf{s}_{\mathbf{s}}^H \mathbf{s}_{\mathbf{s}} = M$. Applying this constraint, we get the matched-filter gain

$$\mu = \sqrt{\frac{M}{\left(\hat{\mathbf{g}} \odot \mathbf{s}_{\mathbf{s}}\right)^H \mathbf{T}\mathbf{T}^H \left(\hat{\mathbf{g}} \odot \mathbf{s}_{\mathbf{s}}\right)}}, \tag{3.34}$$

and define the conformal array spatial steering vector as

$$\begin{aligned} \mathbf{s}_{\mathbf{s,cfa}} &= \sqrt{\frac{M}{\tilde{\mathbf{e}}_{\mathbf{sg}}^H \tilde{\mathbf{e}}_{\mathbf{sg}}}} \tilde{\mathbf{e}}_{\mathbf{sg}}, \\ \tilde{\mathbf{e}}_{\mathbf{sg}} &= \mathbf{T}^H \left(\hat{\mathbf{g}} \odot \mathbf{s}_{\mathbf{s}}\right). \end{aligned} \tag{3.35}$$

3.6.3 Circular Array Example

We present a more intuitive explanation of the conformal array matched filter using the three-element circular array shown in Fig. 3.10. For this array, element one's normal is aligned with the x-axis, element two's normal is 45° from the x-axis, and element three's normal is aligned with the y-axis. From (3.12), we calculate the conventional spatial steering vector for three different directions of arrival as

$$\mathbf{s}_{\mathbf{s}}\left(\theta\right) = \begin{cases} \begin{bmatrix} -1 & e^{j\frac{\pi}{\sqrt{2}}} & 1 \end{bmatrix}^T & \theta = 0° \\ \begin{bmatrix} e^{j\frac{\pi}{\sqrt{2}}} & -1 & e^{j\frac{\pi}{\sqrt{2}}} \end{bmatrix}^T & \theta = 45°. \\ \begin{bmatrix} 1 & e^{j\frac{\pi}{\sqrt{2}}} & -1 \end{bmatrix}^T & \theta = 90° \end{cases} \tag{3.36}$$

From (3.1), the element gains are

$$g_e(\alpha)=\begin{cases}1 & \alpha=0^\circ\\ 0.5 & \alpha=45^\circ,\\ 0 & \alpha=90^\circ\end{cases} \tag{3.37}$$

where α is the angle between the element normal and the direction of interest. For the case of a signal impinging on the array from the x-axis $(\theta=0^\circ)$, we expect element one to have the highest signal gain and element three to have a very low signal gain. If we use the conventional matched filter from (3.36), all of the elements are weighted equally, and element three will contribute just as much as element one despite not receiving any of the signal. Applying the conformal matched filter from (3.33), we get

$$\mathbf{s}_{\text{s,cfa}}(\theta)=\begin{cases}\mu(\theta=0^\circ)\left[-1 \quad \frac{1}{\sqrt{2}}e^{j\frac{\pi}{\sqrt{2}}} \quad 0\right]^T & \theta=0^\circ\\ \mu(\theta=45^\circ)\left[\frac{1}{\sqrt{2}}e^{j\frac{\pi}{\sqrt{2}}} \quad -1 \quad \frac{1}{\sqrt{2}}e^{j\frac{\pi}{\sqrt{2}}}\right]^T & \theta=45^\circ.\\ \mu(\theta=90^\circ)\left[0 \quad \frac{1}{\sqrt{2}}e^{j\frac{\pi}{\sqrt{2}}} \quad -1\right]^T & \theta=90^\circ\end{cases} \tag{3.38}$$

Now, in the case of a signal impinging on the array from $\theta=0^\circ,$ element three has no contribution as expected.

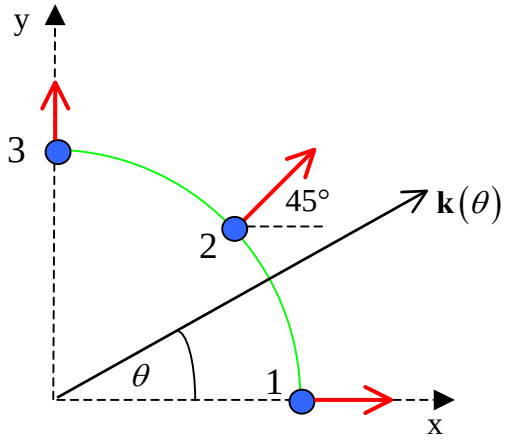

Figure 3.10. Example three-element circular array.

We illustrate the importance of the matched-filter gain by again using the circular array shown in Fig. 3.10. In the case of only white noise, we expect the output power, $P(\theta) = \mathbf{w}^H(\theta)\mathbf{R_n}\mathbf{w}(\theta) = \sigma_n^2 \mathbf{w}^H(\theta)\mathbf{w}(\theta)$, to be $3\sigma_n^2$ for all θ. However, if we let $\mathbf{w}(\theta) = \mathbf{s}_{\mathbf{s,cfa}}(\theta)$ from (3.38) with $\mu(\theta) = 1$ for all θ,

$$P(\theta) = \begin{cases} 1.5\sigma_n^2 & \theta = 0° \\ 2\sigma_n^2 & \theta = 45°. \\ 1.5\sigma_n^2 & \theta = 90° \end{cases} \tag{3.39}$$

Using the incorrect matched-filter gain causes the array power to vary over angle, which is incorrect for the white-noise-only case. Applying the correct values of μ as defined in (3.35), gives the matched filter as

$$\mathbf{s}_{\mathbf{s,cfa}}(\theta) = \begin{cases} \sqrt{2}\left[-1 \quad \frac{1}{\sqrt{2}} e^{j\frac{\pi}{\sqrt{2}}} \quad 0\right]^T & \theta = 0° \\ \sqrt{1.5}\left[\frac{1}{\sqrt{2}} e^{j\frac{\pi}{\sqrt{2}}} \quad -1 \quad \frac{1}{\sqrt{2}} e^{j\frac{\pi}{\sqrt{2}}}\right]^T & \theta = 45°, \\ \sqrt{2}\left[0 \quad \frac{1}{\sqrt{2}} e^{j\frac{\pi}{\sqrt{2}}} \quad -1\right]^T & \theta = 90° \end{cases} \tag{3.40}$$

and the output power as

$$P(\theta) = \begin{cases} 3\sigma_n^2 & \theta = 0° \\ 3\sigma_n^2 & \theta = 45°. \\ 3\sigma_n^2 & \theta = 90° \end{cases} \tag{3.41}$$

Using the correct matched-filter gain gives the expected output noise power over all angles.

3.6.4 Space-Time-Matched-Filter

For the conformal array case, the temporal matched filter is consistent with the conventional case as defined in (3.18). From this we define the conformal-array space-time matched filter as

$$\mathbf{s}_{\text{s-t,cfa}} = \mathbf{s}_{\text{t}} \otimes \mathbf{s}_{\text{s,cfa}}. \tag{3.42}$$

3.7 Array Errors

In this section we present two classifications of array spatial steering vector errors, angle-independent and angle-dependent errors. We present details on the impact of array errors on adaptive performance and some ameliorating solutions in Chapter 7.

Channel mismatch create angle-independent errors between the true and assumed spatial steering vector [41-44]. We model the mismatch as multiplicative i.i.d. complex Gaussian errors fixed over all angles and applied at the element level. Therefore, the true element-level spatial steering vector with angle-independent errors is

$$\mathbf{s}_{\text{s}}(\boldsymbol{\psi}) = \mathbf{v}_{\text{s}}(\boldsymbol{\psi}) \odot \boldsymbol{\eta}_{\text{s}}, \tag{3.43}$$

where $\mathbf{v}_{\text{s}}(\boldsymbol{\psi}) = \left[e^{j\mathbf{k}(\boldsymbol{\psi})\cdot\mathbf{d}_{\text{e}/1}} \quad e^{j\mathbf{k}(\boldsymbol{\psi})\cdot\mathbf{d}_{\text{e}/2}} \quad \ldots \quad e^{j\mathbf{k}(\boldsymbol{\psi})\cdot\mathbf{d}_{\text{e}/M_e}} \right]^T$ is the assumed spatial steering vector and $\boldsymbol{\eta}_{\text{s}}$ is a vector of complex Gaussian errors.

Flexing and bending of the conformal surface induces element position and normal errors, which create an angle-dependent spatial steering vector mismatch. Ideally, these errors are correlated both between elements and between position and normal, but for ease of implementation we model these as i.i.d. errors such that

$$\begin{aligned}\bar{\mathbf{d}}_{\mathbf{e}/m} &= \mathbf{d}_{\mathbf{e}/m} + \boldsymbol{\eta}_{\mathbf{e}/m};\\ \bar{\mathbf{n}}_{\mathbf{e}/m} &= \mathbf{n}_{\mathbf{e}/m} + \boldsymbol{\eta}_{\mathbf{n}/m},\end{aligned} \tag{3.44}$$

where $\boldsymbol{\eta}_{\mathbf{e}/m}$ is an i.i.d. vector of Gaussian element position errors and $\boldsymbol{\eta}_{\mathbf{n}/m}$ is an i.i.d. vector of Gaussian element normal errors. As a result of these errors, the true element-level spatial steering phases and gains are

$$\begin{aligned}&\left[\mathbf{s}_{\mathbf{s}}\left(\boldsymbol{\psi}\right)\right]_m = e^{j\mathbf{k}(\boldsymbol{\psi})\cdot\bar{\mathbf{d}}_{\mathbf{e}/m}};\\ &g_{e/m}\left(\boldsymbol{\psi}\right) = \begin{cases} g_0\cos^2\left(\bar{\alpha}_m\dfrac{\pi}{\theta_{null}}\right) & -\dfrac{\pi}{2}\le\bar{\alpha}_m\le\dfrac{\pi}{2} \\ g_b g_0\cos^2\left(\bar{\alpha}_m\dfrac{\pi}{\theta_{null}}\right) & \dfrac{\pi}{2}<\bar{\alpha}_m<\dfrac{3\pi}{2}\end{cases};\\ &\bar{\alpha}_m = \cos^{-1}\left(\bar{\mathbf{n}}_{\mathbf{e}/m}\cdot\mathbf{k}\left(\boldsymbol{\psi}\right)\right).\end{aligned} \tag{3.45}$$

3.8 Performance Metrics

In this section we present a set of performance metrics, which we use to characterize a conformal array's response and adaptive performance in the presence of ground clutter interference.

3.8.1 Array Transmit Pattern

We plot the 3-D array transmit pattern as defined in (3.4), varying the angle vector $\boldsymbol{\psi}$ over the full k space. As previously stated and shown in Fig. 2.1, we define a unit vector pointing in the direction $\boldsymbol{\psi}$ as

$$\mathbf{k}\left(\boldsymbol{\psi}\right) = k_x\hat{\mathbf{x}} + k_y\hat{\mathbf{y}} + k_z\hat{\mathbf{z}} = \cos\left(\theta\right)\cos\left(\phi\right)\hat{\mathbf{x}} + \cos\left(\theta\right)\sin\left(\phi\right)\hat{\mathbf{y}} + \sin\left(\theta\right)\hat{\mathbf{z}}. \tag{3.46}$$

To cover the full 3-D k space, we can either vary azimuth angle ϕ and elevation angle θ, or vary k_x, k_y, and k_z. To demonstrate the difference, we show the transmit pattern for a planar array plotted using both techniques in Fig. 3.11. In the azimuth-elevation plot on the left, the array pattern is significantly distorted due to the nonlinearity between the angles and the pointing vector. In the $k_y - k_z$ plot on the right, we see a more true array pattern. Note that since we have a narrowband array, $k_x = \pm\sqrt{1-k_y^2-k_z^2}$.

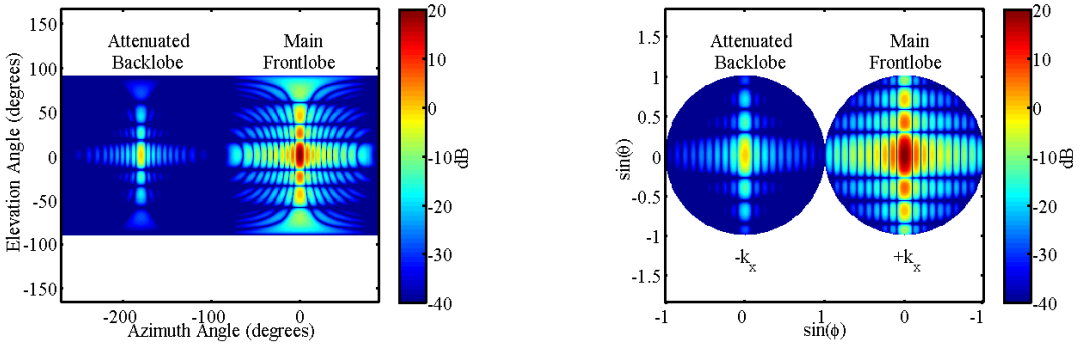

Figure 3.11. Transmit pattern for a planar array plotted using azimuth and elevation angles (left) and k values (right).

3.8.2 Angle-Doppler Spectra

In general, we define power spectrum as

$$P(f_d, \boldsymbol{\psi}) = \mathbf{w}^H \mathbf{R} \mathbf{w}, \tag{3.47}$$

where $\mathbf{w}$ is a space-time weight vector and $\mathbf{R}$ is a space-time covariance matrix. We define the following cases for the MVDR weight vector:

- Optimal (known covariance matrix)

- $\mathbf{w}_k = \dfrac{\mathbf{R}_k^{-1}\mathbf{s}_{\text{s-t,cfa}}(f_d,\psi)}{\mathbf{s}_{\text{s-t,cfa}}^H(f_d,\psi)\mathbf{R}_k^{-1}\mathbf{s}_{\text{s-t,cfa}}(f_d,\psi)}$

- $P_{MVDR/k}(f_d,\psi) = \dfrac{1}{\mathbf{s}_{\text{s-t,cfa}}^H(f_d,\psi)\mathbf{R}_k^{-1}\mathbf{s}_{\text{s-t,cfa}}(f_d,\psi)}$

- Estimate

  - $\mathbf{w}_k = \dfrac{\hat{\mathbf{R}}_k^{-1}\mathbf{v}_{\text{s-t,cfa}}(f_d,\psi)}{\mathbf{v}_{\text{s-t,cfa}}^H(f_d,\psi)\hat{\mathbf{R}}_k^{-1}\mathbf{v}_{\text{s-t,cfa}}(f_d,\psi)};\ \hat{\mathbf{R}}_k = \dfrac{1}{K}\sum_{m=1}^{K}\mathbf{x}_m\mathbf{x}_m^H$

  - $\hat{P}_{MVDR/k}(f_d,\psi) = \dfrac{\mathbf{v}_{\text{s-t,cfa}}^H(f_d,\psi)\hat{\mathbf{R}}_k^{-1}\mathbf{R}_k\hat{\mathbf{R}}_k^{-1}\mathbf{v}_{\text{s-t,cfa}}(f_d,\psi)}{\left(\mathbf{v}_{\text{s-t,cfa}}^H(f_d,\psi)\hat{\mathbf{R}}_k^{-1}\mathbf{v}_{\text{s-t,cfa}}(f_d,\psi)\right)^2}$

For linear arrays, we can define spatial frequency entirely using one variable, which allows us to plot the full angle-Doppler spectrum as shown in Fig. 3.12 for a forward-looking ULA.

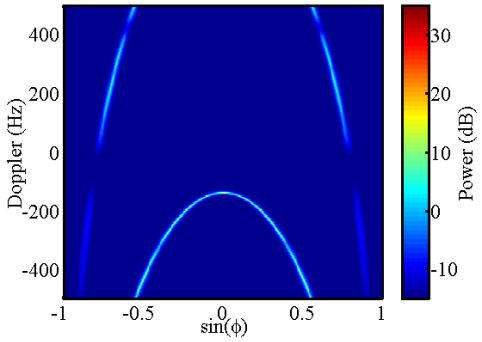

Figure 3.12. Known MVDR spectra for a ten-element forward-looking ULA.

For conformal arrays on the other hand, we require two spatial variables as previously discussed in Section 3.7.1. To fully display the complete angle-Doppler, we can use 3-D clutter ridge plots as shown in Fig. 3.13 for a chined conformal array. To generate these

plots, we plot only the peak Doppler at all spatial frequencies. This gives us a full spatial view at the expense of Doppler. To view the Doppler profile, we plot slices of the angle-Doppler spectra at specified azimuth and elevation as shown in Fig. 3.14.

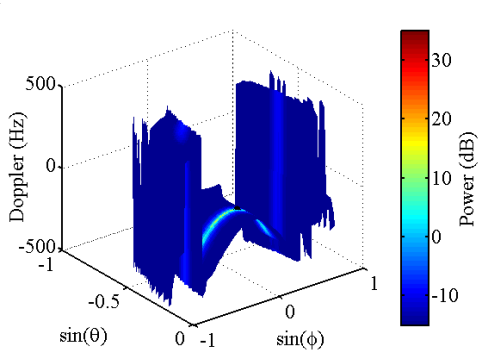

Figure 3.13. 3-D clutter ridge for a ten-channel chined conformal array.

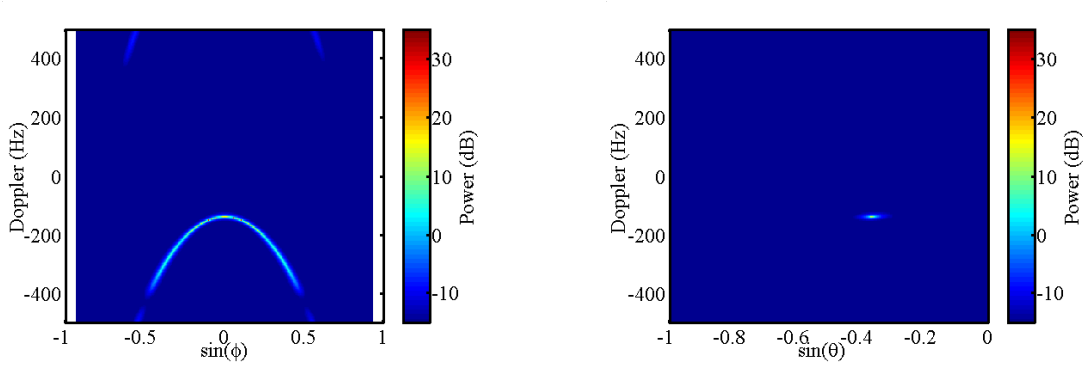

Figure 3.14. 2-D MVDR spectra slices, azimuth (left) and elevation (right), for a ten-channel chined conformal array.

3.8.3 SINR Loss

As previously discussed in Chapter 2, we can express SINR in terms of SNR and SINR loss terms such that

$$\text{SINR}_{\text{adap}} = \text{SNR} \cdot L_{s,1} \cdot L_{s,2}. \tag{3.48}$$

We define

$$L_{s,1} = \frac{\text{SINR}_{\text{opt}}}{\text{SNR}} = \sigma_n^2 \frac{\mathbf{s}_{\text{s-t,cfa}}^H \mathbf{R}_k^{-1} \mathbf{s}_{\text{s-t}}}{\mathbf{s}_{\text{s-t,cfa}}^H \mathbf{s}_{\text{s-t,cfa}}}, \tag{3.49}$$

which represents losses for the joint-domain optimum (JDO) filter case. We can also view this term as losses caused from colored noise (clutter and jamming) and refer to it as clairvoyant loss as it requires perfect knowledge of both the space-time covariance matrix and the conformal space-time steering vector. In practice, we do not have perfect knowledge of these terms, and so they must be estimated. This leads us to the $L_{s,2}$ term, which we define as

$$L_{s,2} = \frac{\text{SINR}_{\text{adap}}}{\text{SINR}_{\text{opt}}} = \frac{\left| \mathbf{v}_{\text{s-t,cfa}}^H \hat{\mathbf{R}}_k^{-1} \mathbf{s}_{\text{s-t,cfa}} \right|^2}{\left(\mathbf{s}_{\text{s-t,cfa}}^H \mathbf{R}_k^{-1} \mathbf{s}_{\text{s-t,cfa}} \right) \left(\mathbf{v}_{\text{s-t,cfa}}^H \hat{\mathbf{R}}_k^{-1} \mathbf{R}_k \hat{\mathbf{R}}_k^{-1} \mathbf{v}_{\text{s-t,cfa}} \right)}. \tag{3.50}$$

$L_{s,2}$ represents adaptive losses from inaccurate estimation of the space-time covariance matrix and conformal space-time steering vector. Unlike SINR, these SINR loss terms are independent of the signal power. This independence is useful in that we need not define any target parameters (radar cross section, range, DOA) to evaluate performance, which results in range-independent losses.

CHAPTER 4

CONVENTIONAL STAP RESULTS

4.1 Overview

In this chapter we present clutter simulation results and analysis for a variety of array geometries. We begin by presenting the simulation parameters for both the radar system and array geometries in Section 4.2. We next present results for the conformal array matched filter in Section 4.3. In Section 4.4 we show results for conventional full-dimension STAP and show these algorithms suffer from array-induced clutter nonstationarity. In Sections 4.5-4.7 we attempt some well known ameliorating solutions including nonadaptive processing, localized training through reduced-dimension STAP, and time-varying weights.

4.2 Simulation Parameters

Using the previously described clutter model, we generate simulated space-time data cubes and the corresponding known space-time covariance matrices. We choose radar and array parameters for the following applications:

- Ultra high frequency (UHF) electronically scanned array (UESA)
- Surveillance (UAV)
- Nose mounted (Fighter)

We choose the UESA parameters to duplicate the circular array STAP results from [17]. We choose the surveillance and nose-mounted applications as candidate conformal array designs.

Table 4.1 shows the radar system parameters for each application. The UESA parameters are consistent with those in [17]. We choose the surveillance parameters to simulate a UAV's flight (high altitude and low velocity) and the nose-mounted parameters to simulate a fighter's flight (low altitude and high velocity).

Table 4.1. Radar system parameters for UESA, surveillance, and nose-mounted applications.

Application	Frequency	PRF	Bandwidth	Pulses	Subarrays	Platform Height	Platform Velocity
UESA	0.45 GHz	300 Hz	4 MHz	18	18,20	9 km	50 m/s
Surveillance	1.5 GHz	1 kHz	7.5 MHz	32	10	20 km	100 m/s
Nose Mounted	1.5 GHz	1 kHz	7.5 MHz	32	10	11 km	200 m/s

Multiple parameters can be varied for each conformal array design, including the surface size, surface curvature, surface orientation, array steering, element locations, and subarraying strategy. For the analysis considered herein, we choose the parameters for each conformal array as shown in Table 4.2. For each set of applications, we keep the array aperture and subarraying strategy consistent thereby facilitating comparisons between different array geometries. Additionally, we make comparisons between array orientations (i.e., crab or yaw). Traditionally we define the array crab as the angle between the platform velocity vector and the array normal. Since we do not have an array normal for conformal arrays, we define the array crab as the angle between the

platform velocity vector and the steered azimuth angle. Finally for the surveillance and nose-mounted applications, we use the bar-steering scheme described in Table 4.3. This steering method generates multiple data cubes with different steered elevation angles, allowing for full illumination of the radar's unambiguous range.

For the estimated space-time covariance matrix we use the MLE with modest diagonal loading, i.e.,

$$\hat{\mathbf{R}}_k = \frac{1}{K_i}\sum_{m=1}^{K_i}\mathbf{x}_m\mathbf{x}_m^H + \frac{\sigma_n^2}{100}\mathbf{I}, \tag{4.1}$$

where $K_i = \min\left(2MN, L_i\right)$ and L_i is the total number of range cells in data cube *i* corresponding to the ith beam position. The –20 dB diagonal loading term ensures a nonsingular matrix. Additionally, we assume perfect knowledge of the space-time steering vector so that

$$\mathbf{v}_{\mathbf{s\text{-}t,cfa}} = \mathbf{s}_{\mathbf{s\text{-}t,cfa}}. \tag{4.2}$$

We analyze the effect of steering vector mismatch in Chapter 7.

Table 4.2. Array geometry specifications for UESA, surveillance, and nose-mounted applications.

Application	Geometry	Active Array Size			Elements		Orientation		Array Pre-Steering		Element Type	
		Length	Height	Depth	Number	Spacing	Crab	Tilt	Azimuth	Elevation	Pattern	Backlobe Attenuation
UESA	ULA	6.0 m	0.0 m	0.0 m	18	λ/2	90°	0°	0°	0°	cos sq	25 dB
	Circular	6.0 m	0.0 m	0.8 m	20	λ/2	90°	0°	0°	0°	cos sq	25 dB
Surveillance	Planar	1.9 m	0.6 m	0.0 m	140	λ/2	90°,83°	-40°	0°	See Table 4.3	cos sq	40 dB
	Uniform Canoe	1.9 m	0.6 m	0.7 m	160	λ/2	90°,83°	0°	0°	See Table 4.3	cos sq	40 dB
	Tapered Canoe	1.9 m	0.6 m	0.7 m	160	λ/2	90°,83°	0°	0°	See Table 4.3	cos sq	40 dB
	Airfoil	1.9 m	0.3 m	0.7 m	160	λ/2	0°	0°	0°	See Table 4.3	cos sq	40 dB
Nose Mounted	Planar	0.9 m	0.7 m	0.0 m	80	λ/2	0°	0°	0°	See Table 4.3	cos sq	40 dB
	Cone	0.9 m	0.5 m	1.1 m	117	λ/2	0°	0°	0°	See Table 4.3	cos sq	40 dB
	Chined	0.9 m	0.5 m	1.1 m	117	λ/2	0°	0°	0°	See Table 4.3	cos sq	40 dB

Table 4.3. Bar steering scheme for surveillance and nose-mounted applications.

Surveillance Applications					Nose-Mounted Applications				
Data Cube	Steered Elevation Angle	Range Bins	Slant Ranges		Data Cube	Steered Elevation Angle	Range Bins	Slant Ranges	
			From	To				From	To
1	-46°	350	25 km	32 km	1	-39°	300	15 km	21 km
2	-33°	700	31 km	45 km	2	-26°	650	20 km	33 km
3	-20°	2000	44 km	84 km	3	-14°	2500	32 km	82 km

4.3 Matched-Filter Results

We analyze the impact of the conformal array matched filter by comparing the clutter responses of a circular array with normals oriented in the same direction and normals oriented perpendicular to the surface, as shown in Fig 4.1. In Fig. 4.2 we show clairvoyant SINR loss for both arrays using both the conformal and conventional matched filters. For the array with constant normals, the conventional and conformal matched filters show perfect agreement as all elements have the same gain for any given look direction. For the array with varying normals however, the conventional matched filter results in a 40 dB drop in the clutter-to-noise ratio (CNR) indicating we must account for both amplitude and phase in our matched filter design.

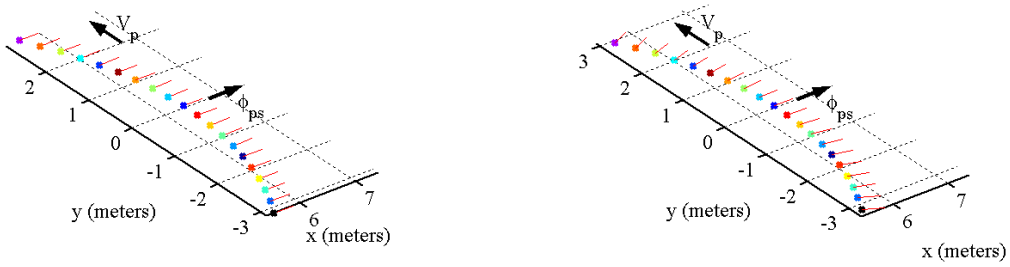

Figure 4.1.Circular array geometries with normals oriented in the same direction (left) and normals oriented perpendicular to the surface (right).

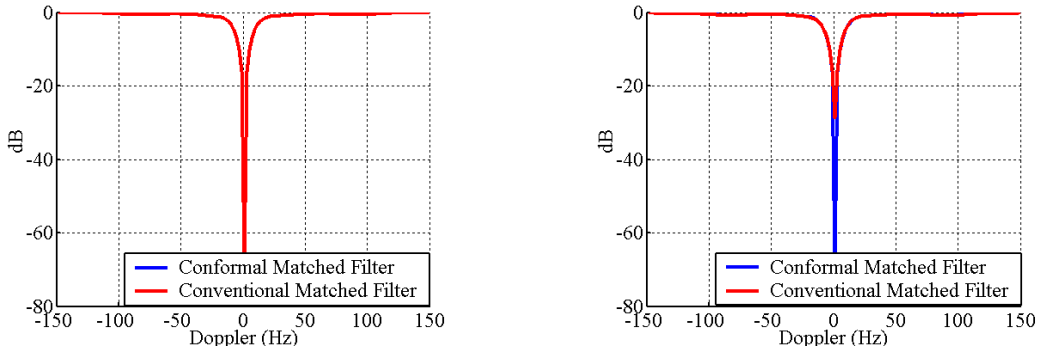

Figure 4.2. Conventional and conformal matched filter clairvoyant SINR loss responses for a circular array with constant normals.

4.4 Full-Dimension STAP Results

4.4.1 UESA Results

We present the UESA results to duplicate the findings in [17], where the author compares the STAP performance of a ULA and a circular array and finds that for conventional STAP algorithms the circular array has a loss in performance when compared with the ULA, especially at close ranges. We show the duplicated ULA and circular array geometries in Fig 4.3. The array configuration indicates the array elements, normals, pre-steered azimuth angle, and platform velocity direction.

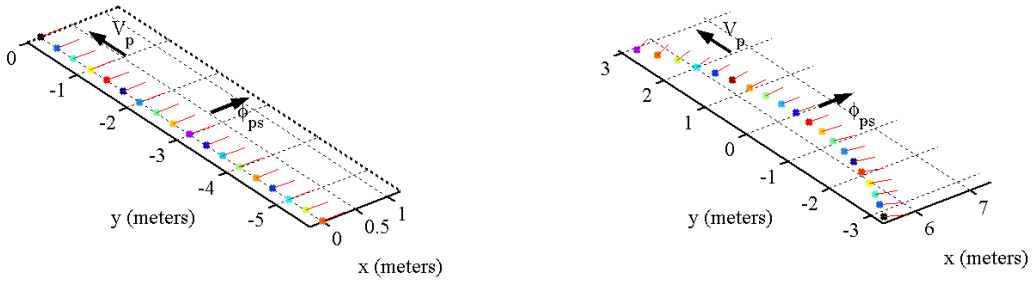

Figure 4.3. Array configurations for a side-looking ULA (left) and side-looking circular array (right) used for UESA applications.

We show simulated SINR loss results for both geometries in Figs. 4.4 and 4.5. These plots show clairvoyant loss $\left(L_{s,1}\right)$ and adaptive loss $\left(L_{s,2}\right)$ as a function of Doppler and range. Looking at the clairvoyant loss for both arrays, we see similar performance with the clutter null centered at zero Doppler as expected for the side-looking case. Looking at the adaptive losses, we see a significant difference in performance. For the ULA, we see approximately 3 dB of loss at all range and Doppler values as predicted by the RMB

rule. For the circular array, on the other hand, we see increased losses particularly at close ranges. These losses result from array induced clutter nonstationarity, where the array's angle-Doppler properties vary over the training region. This variation leads to an inaccurate space-time covariance matrix estimate, which in turn leads to increased adaptive losses. These results show excellent agreement with those reported in [17].

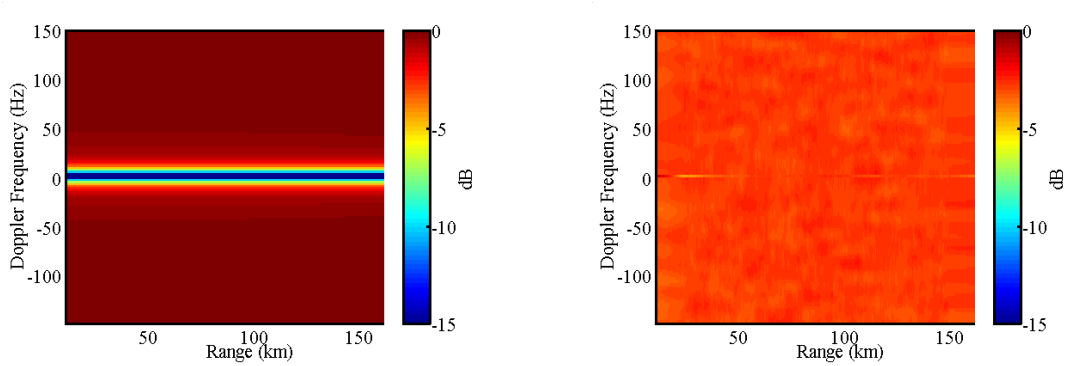

Figure 4.4. Range-Doppler maps of clairvoyant SINR loss (left) and adaptive SINR loss (right) for a ULA.

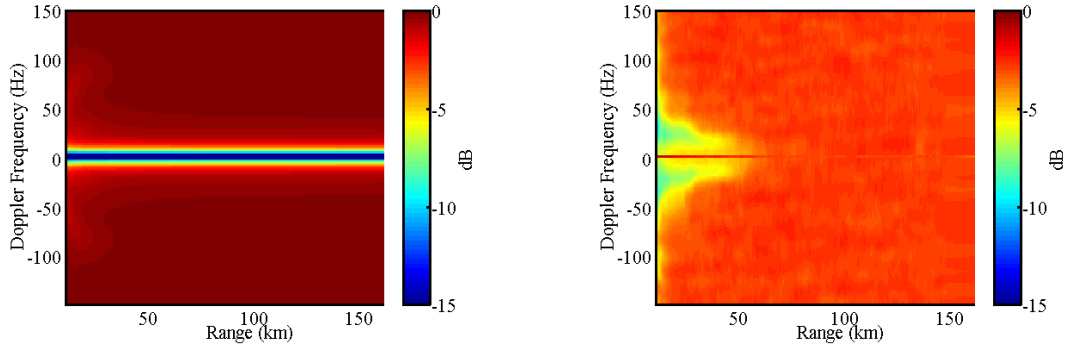

Figure 4.5. Range-Doppler maps of clairvoyant SINR loss (left) and adaptive SINR loss (right) for a circular array.

4.4.2 Surveillance Results

We show the array configuration and corresponding transmit pattern for the side-looking planar array in Fig. 4.6. We tilt the array 40° forward to focus the beam at the ranges of interest. The array configuration also shows the subarray scheme as we effectively reduce the planar array into a ULA of subarrays. The array transmit pattern corresponds to the elevation steering for data cube 2 as indicated in Table 4.3.

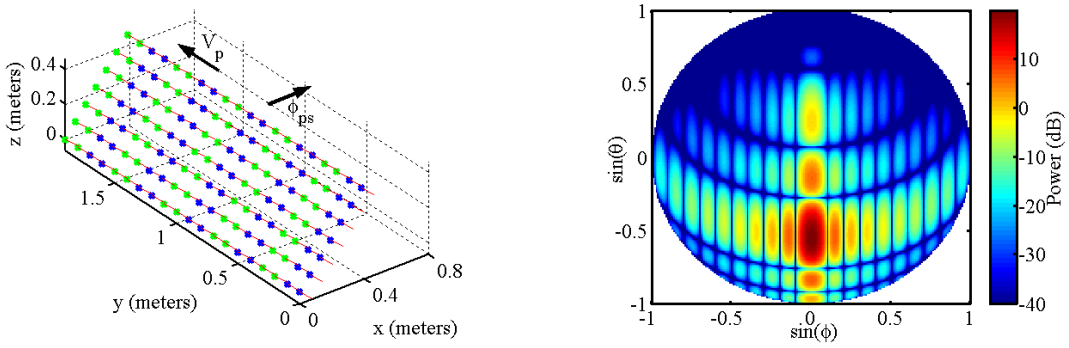

Figure 4.6. Array configuration and transmit pattern for a side-looking planar array used in surveillance applications.

Figure 4.7 shows clairvoyant and adaptive SINR loss as a function of Doppler and range. The clairvoyant loss plot shows the clutter null centered at zero Doppler for all ranges as expected as expected for the side-looking case. The adaptive loss shows approximately 3 dB of loss for data cubes 2 and 3. Data cube 1 has significantly higher losses, which result from insufficient sample support. We can eliminate this loss by applying reduced-dimension STAP techniques as discussed later in Section 4.6.1. In Fig. 4.8 we show a comparison of the known and estimated MVDR spectra at a range of 36 km. These plots clearly show the clutter ridge with linear angle-Doppler properties, as

previously theorized for the side-looking orientation. Additionally, the known and estimated spectra show excellent agreement, which again indicates the clutter is stationary.

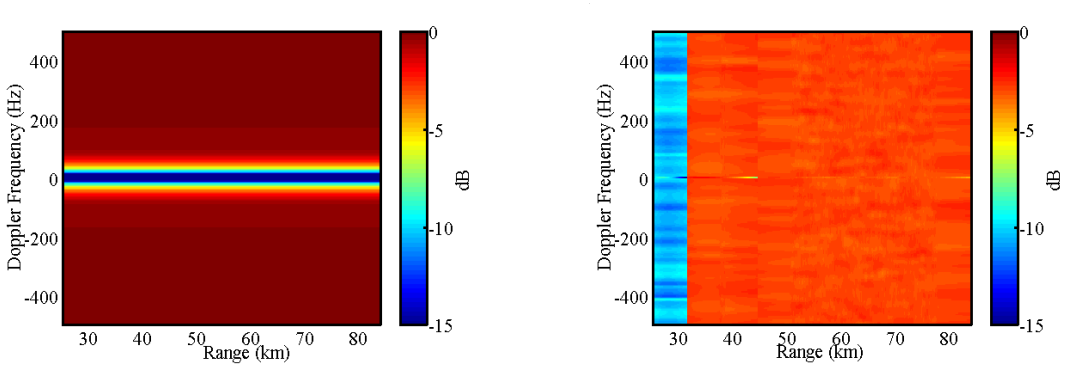

Figure 4.7. Range-Doppler maps of clairvoyant SINR loss (left) and adaptive SINR loss (right) for a side-looking planar array.

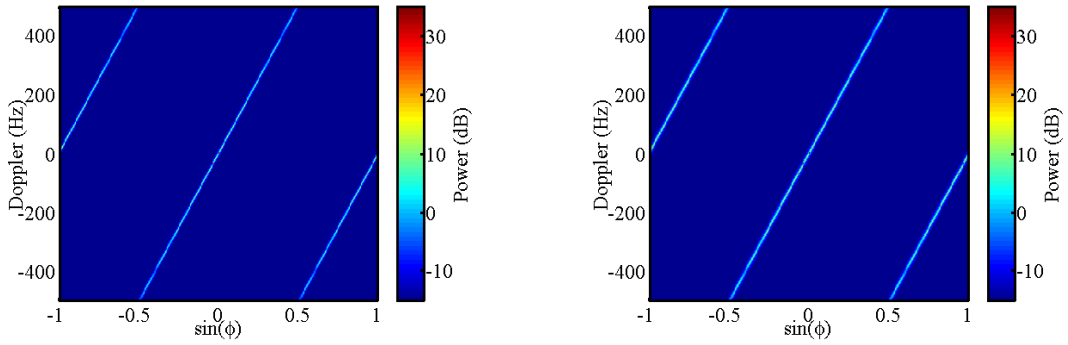

Figure 4.8. Known (left) and estimated (right) MVDR angle-Doppler spectra at a range of 36 km for a side-looking planar array.

Side winds can cause significant shifts in the velocity vector, so that an assumed side-looking array is no longer perfectly side looking. Figure 4.9 shows the surveillance planar array with an 83°-crab orientation, and Fig. 4.10 shows the corresponding SINR loss plots. As can be seen in the clairvoyant loss plot, the clutter null Doppler now varies slightly with range as a result of the crabbed orientation. This orientation also leads to

increased adaptive losses, as the clutter returns seen by the crabbed array are no longer stationary. The highest adaptive losses are at near ranges, where the clutter properties change more rapidly. At more distant ranges, the data realigns, and the adaptive losses approach the expected 3 dB value. As a final note, the discontinuities seen at 31 km and 43 km are a direct result of the bar-steering scheme, where the radar transmit steering is varied over range bars.

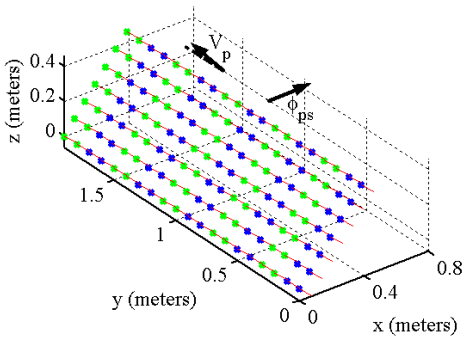

Figure 4.9. Array configuration for a crabbed planar array used in surveillance applications.

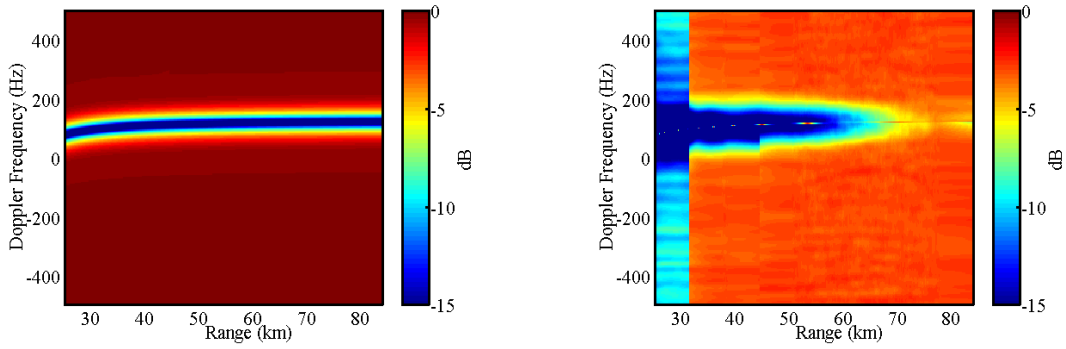

Figure 4.10. Range-Doppler maps of clairvoyant SINR loss (left) and adaptive SINR loss (right) for a crabbed planar array.

To further explore the nonstationary behavior, we show known and estimated MVDR spectra at ranges of 36 km and 70 km in Figs. 4.11 and 4.12 respectively. In all of the

plots we see an elliptical clutter ridge, which is indicative of the crabbed geometry. Additionally, at the nearer range, we see disagreement between the known and estimated spectra. The estimated spectrum shows some spreading of the clutter ridge, indicating the clutter properties are changing with range. At the far range on the other hand, the known and estimated spectra show better agreement, as expected for the stationary case.

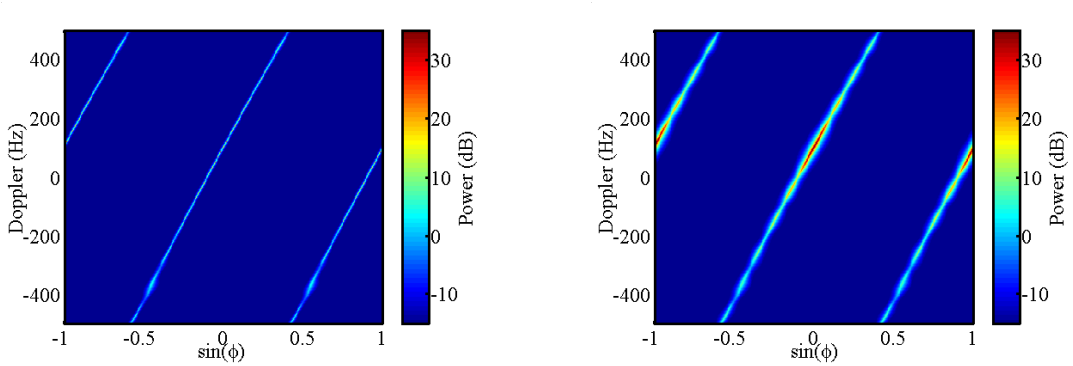

Figure 4.11. Known (left) and estimated (right) MVDR angle-Doppler spectra at a range of 36 km for a crabbed planar array.

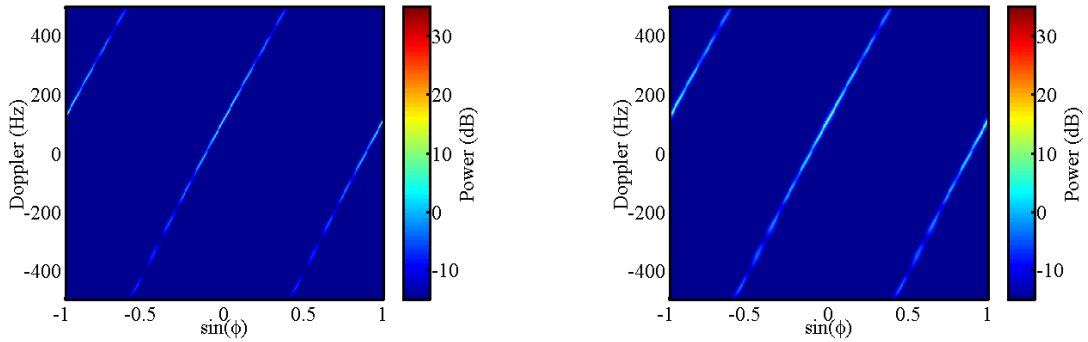

Figure 4.12. Known (left) and estimated (right) MVDR angle-Doppler spectra at a range of 70 km for a crabbed planar array.

The first conformal array we analyze is the side-looking tapered canoe, which we show with its transmit pattern in Fig. 4.13. For this conformal array we use a similar subarraying system as the previous array, but now as a result of the taper along the x-axis,

the subarrays no longer have matching patterns or uniform linear phase centers. This nonuniformity is apparent in the array's transmit pattern. We show the SINR loss results in Fig. 4.14. First looking at the clairvoyant loss, we similar performance to previously shown side-looking planar array geometry with a clutter null at zero Doppler for all ranges. For the adaptive loss, however, we see a significant increase in losses, which result from the array's nonlinear shape and changing angle properties over range.

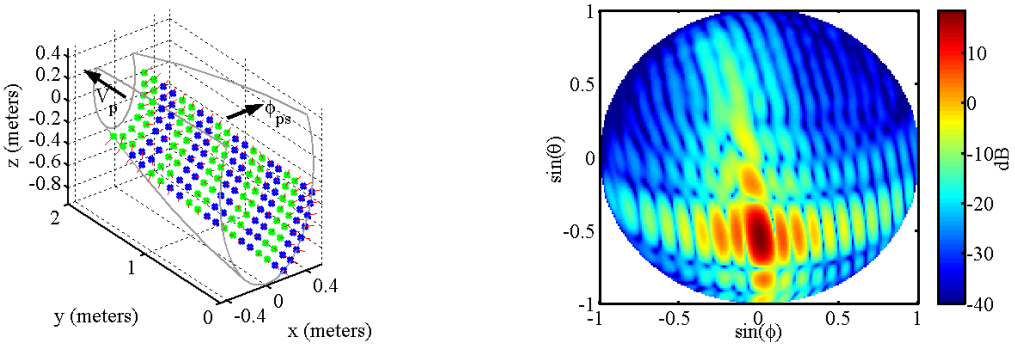

Figure 4.13. Array configuration and transmit pattern for a side-looking tapered-canoe conformal array used in surveillance applications.

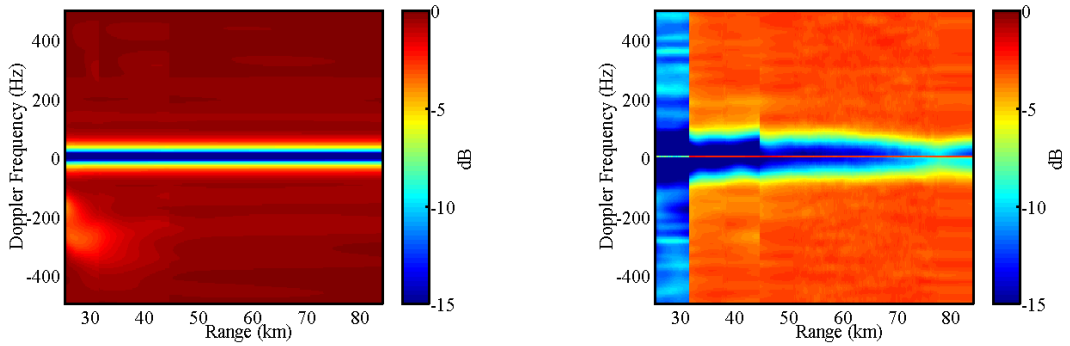

Figure 4.14. Range-Doppler maps of clairvoyant SINR loss (left) and adaptive SINR loss (right) for a side-looking tapered-canoe conformal array.

Because we have nonlinear subarray phase centers for the tapered-canoe conformal array, we must use 3-D clutter ridge plots to analyze the full MVDR spectrum. We show the known and estimated 3-D clutter ridges in Fig. 4.15 along with 2-D slices in elevation

(at $k_y = 0$) and azimuth (at $k_z = 0.55$) in Figs. 4.16 and 4.17, respectively. All of these plots are at a range of 36 km. A comparison of the known and estimated 3-D clutter ridge plots shows the spread of the clutter energy in elevation angle (k_z) for the estimated covariance matrix. We also see this spread in the 2-D elevation-Doppler slice. Looking at the 2-D azimuth-Doppler slice, we also see a small spread in azimuth and Doppler for the estimated covariance matrix.

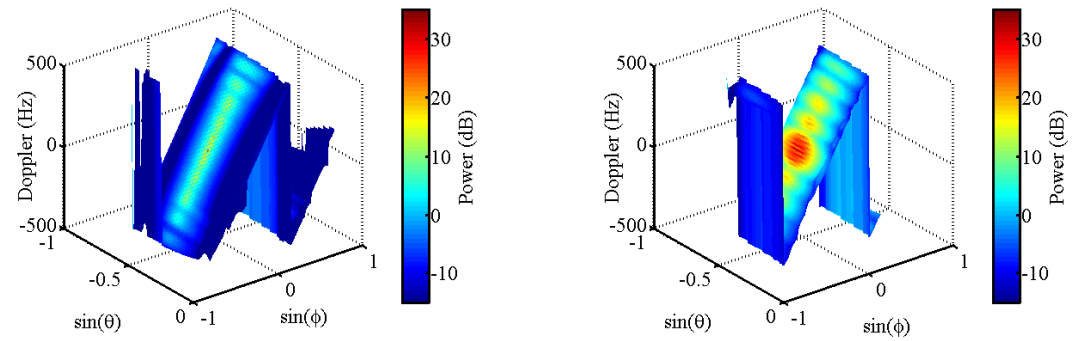

Figure 4.15. Known (left) and estimated (right) 3-D clutter ridges at a range of 36 km for a side-looking tapered-canoe conformal array.

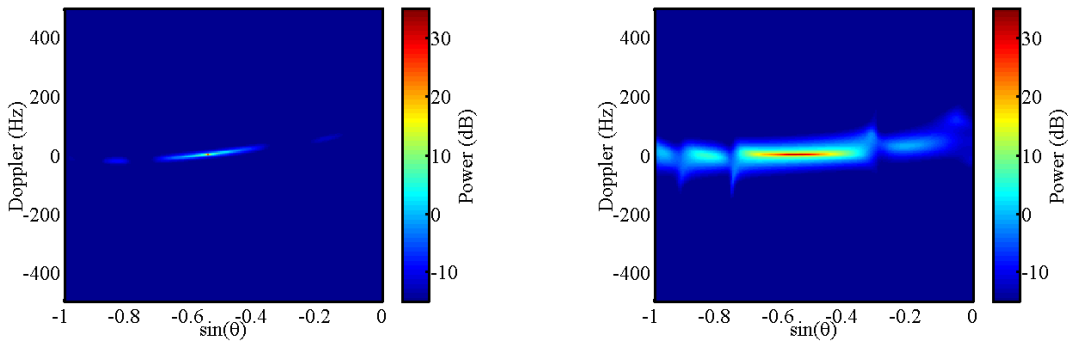

Figure 4.16. Known (left) and estimated (right) MVDR elevation-Doppler spectra at an azimuth of 0° and a range of 36 km for a side-looking tapered-canoe conformal array.

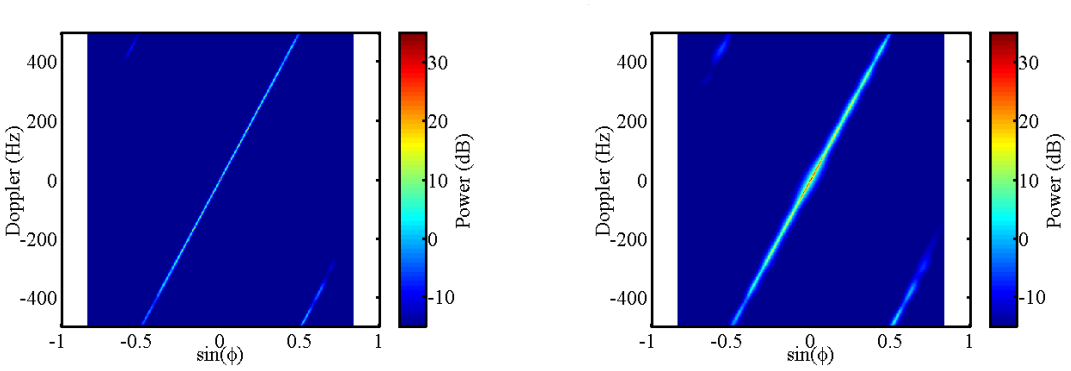

Figure 4.17. Known (left) and estimated (right) MVDR azimuth-Doppler spectra at an elevation of -33° and a range of 36 km for a side-looking tapered-canoe conformal array.

We next analyze the combined case of a nonlinear array geometry and a crabbed orientation for the crabbed tapered-canoe conformal array shown in Fig. 4.18. For this case, the crab angle between the platform velocity vector and the steered-azimuth direction is 83°. Looking at the SINR loss results shown in Fig. 4.19, we see the Doppler shift of the clutter varying with range and get the increased adaptive losses as expected. In Figs. 4.20-4.22, we show the corresponding 3-D clutter ridges as well as 2-D elevation-Doppler and azimuth-Doppler MVDR slices at a range of 36 km. These plots show similar results to those for the side-looking orientation. The one key difference is the elliptically shaped clutter ridge apparent in the azimuth-Doppler slice.

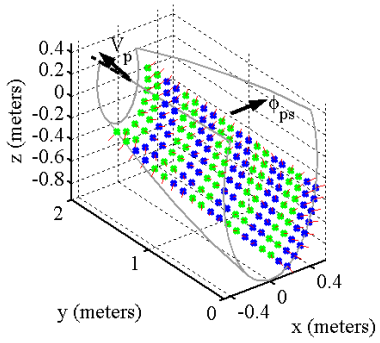

Figure 4.18. Array configuration for a crabbed tapered-canoe conformal array used in surveillance applications.

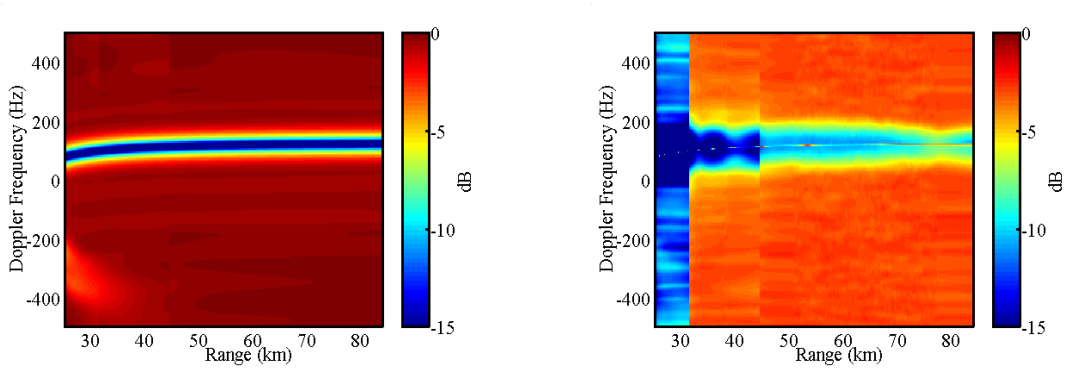

Figure 4.19. Range-Doppler maps of clairvoyant SINR loss (left) and adaptive SINR loss (right) for a crabbed tapered-canoe conformal array.

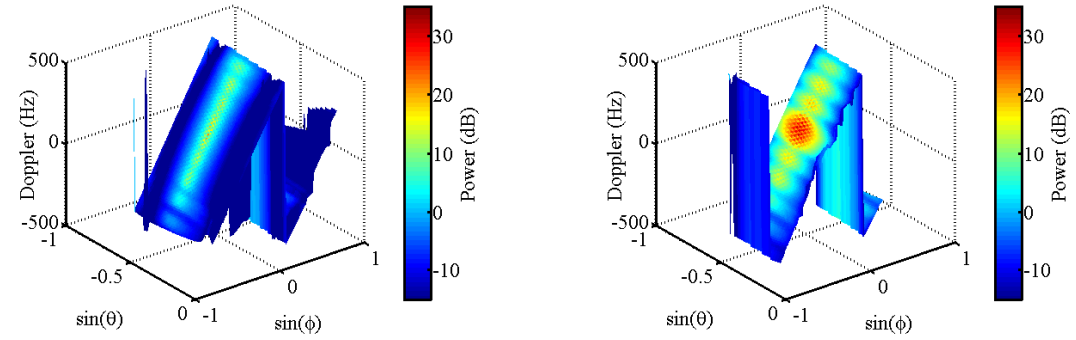

Figure 4.20. Known (left) and estimated (right) 3-D clutter ridges at a range of 36 km for a crabbed tapered-canoe conformal array.

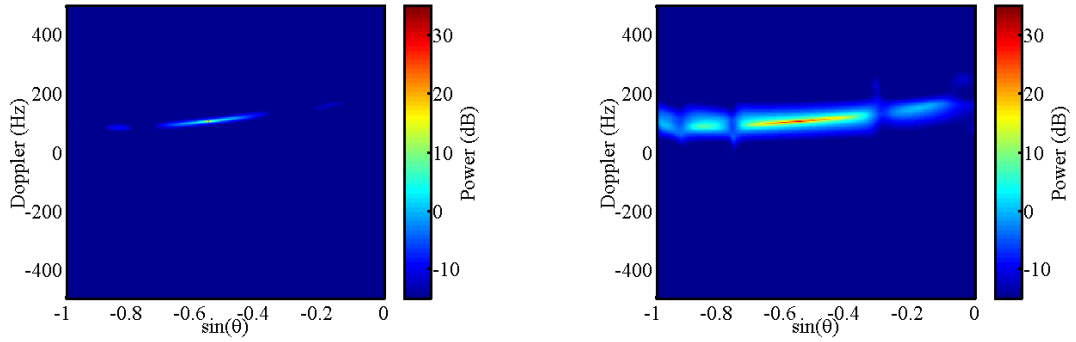

Figure 4.21. Known (left) and estimated (right) MVDR elevation-Doppler spectra at an azimuth of 0° and a range of 36 km for a crabbed tapered-canoe conformal array.

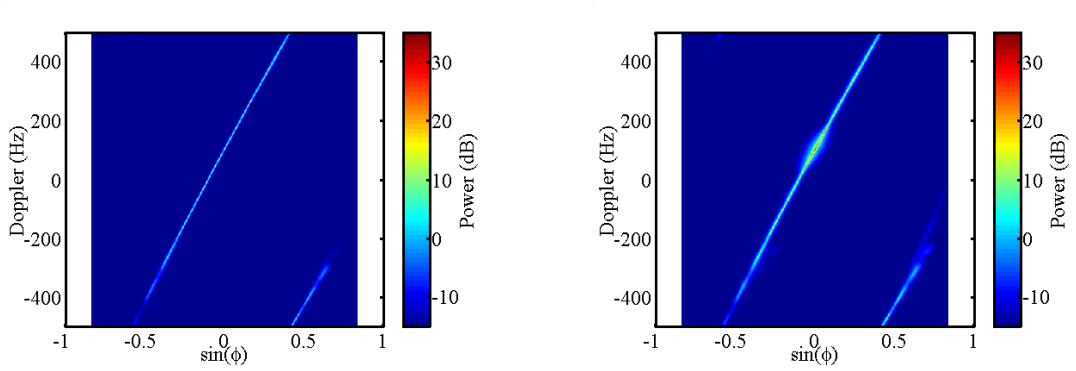

Figure 4.22. Known (left) and estimated (right) MVDR azimuth-Doppler spectra at an elevation of -33° and a range of 36 km for a crabbed tapered-canoe conformal array.

4.4.3 Nose-Mounted Results

Our first nose-mounted application is a forward-looking planar array shown with its transmit pattern in Fig. 4.23. For this geometry, we generate subarrays so that we have both azimuth and elevation DOF. This allows for accurate comparisons with the cone and chined conformal arrays. As a result we do not have a ULA as in the previous planar array geometry. Figure 4.24 shows the SINR loss results. The results are similar to the forward-looking airfoil in that we see very poor adaptive performance indicating a high degree of clutter nonstationarity. We also see the nonstationary behavior in the MVDR spectra shown at a range of 25 km in Figs. 4.25-4.27. The estimated spectra show a spreading of energy in both elevation angle and Doppler, indicating that both elevation angle and Doppler properties are varying with range.

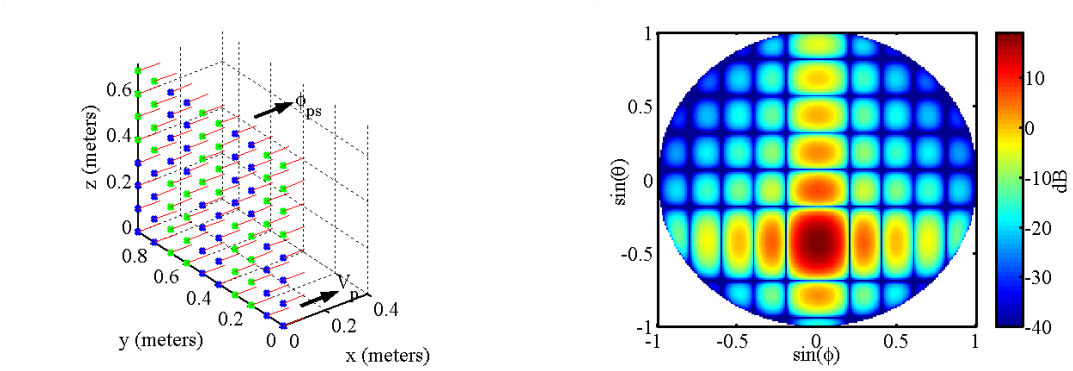

Figure 4.23. Array configuration and transmit pattern for a forward-looking planar array used in nose-mounted applications.

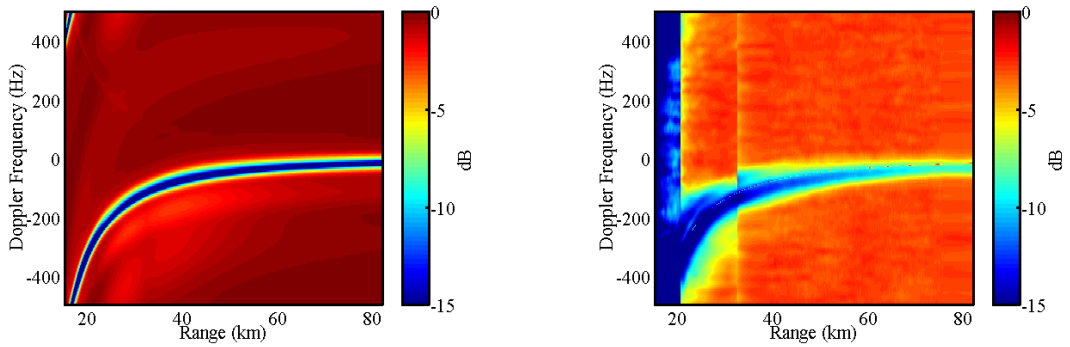

Figure 4.24. Range-Doppler maps of clairvoyant SINR loss (left) and adaptive SINR loss (right) for a forward-looking planar array.

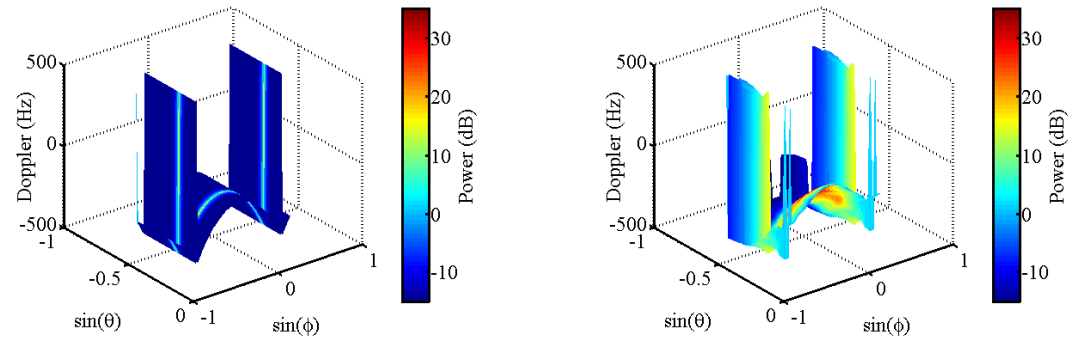

Figure 4.25. Known (left) and estimated (right) 3-D clutter ridges at a range of 25 km for a forward-looking planar array.

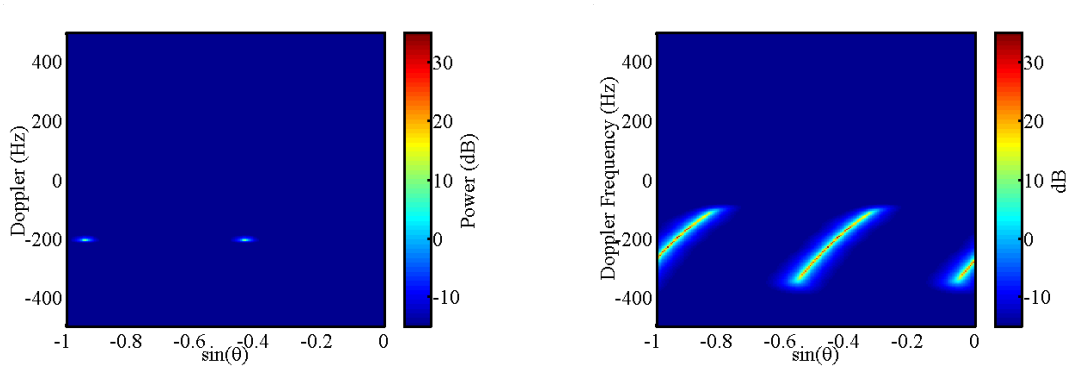

Figure 4.26. Known (left) and estimated (right) MVDR elevation-Doppler spectra at an azimuth of 0° and a range of 25 km for a forward-looking planar array.

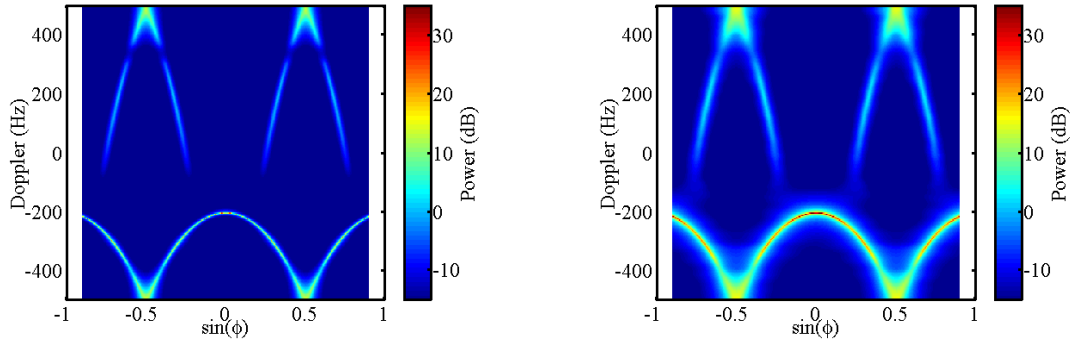

Figure 4.27. Known (left) and estimated (right) MVDR azimuth-Doppler spectra at an elevation of -26° and a range of 25 km for a forward-looking planar array.

For the nose-mounted conformal applications, we look at a more complicated chined conformal array. We present the chined geometry, transmit pattern, SINR loss results, and MVDR spectra in Figs. 4.28-4.32. The main distinction in these results from the previous forward-looking planar array is the poorer transmit pattern quality. The irregular shape of the chined array results in a broader beamwidth with higher sidelobe levels (SLLs). The SINR loss results and MVDR spectra all show similar performance to the previous planar array example, where the high degree of clutter nonstationarity leads to poor adaptive performance. This array does show a slight increase in adaptive losses

when compared to the previous forward-looking planar array, which is a result of the nonlinear array geometry combined with the forward-looking orientation.

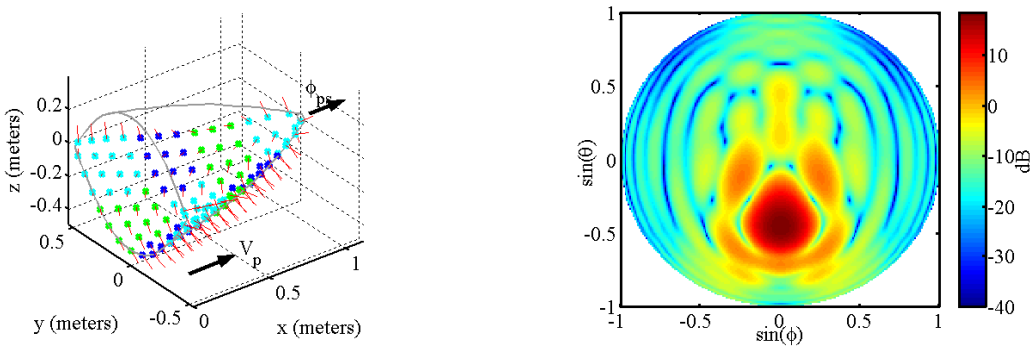

Figure 4.28. Array configuration and transmit pattern for a forward-looking chined conformal array used in nose-mounted applications.

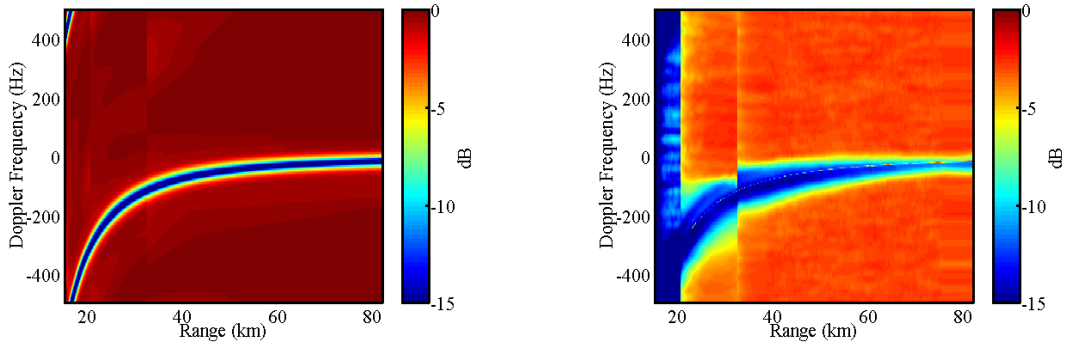

Figure 4.29. Range-Doppler maps of clairvoyant SINR loss (left) and adaptive SINR loss (right) for a forward-looking chined conformal array.

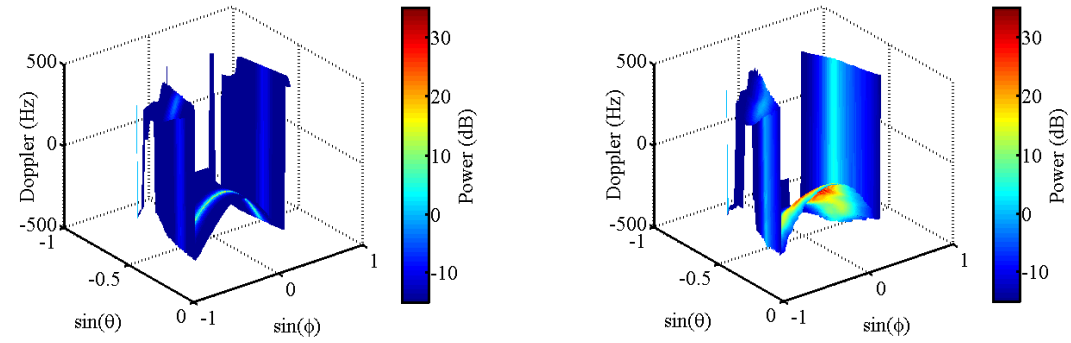

Figure 4.30. Known (left) and estimated (right) 3-D clutter ridges at a range of 25 km for a forward-looking chined conformal array.

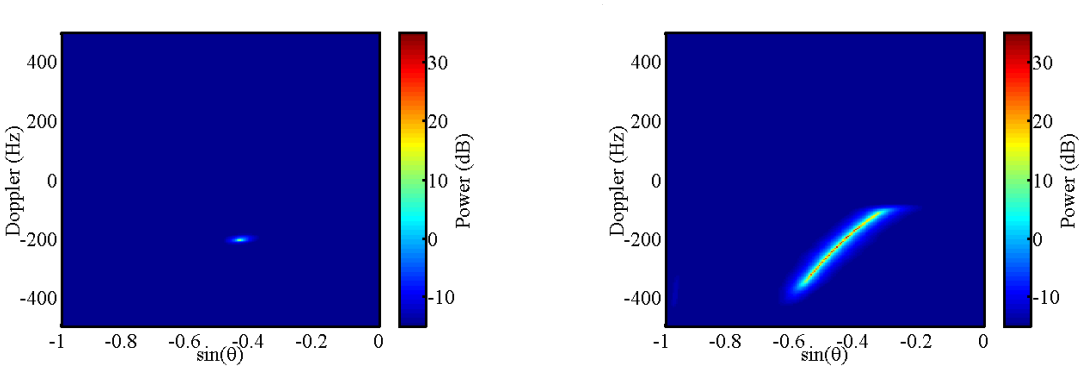

Figure 4.31. Known (left) and estimated (right) MVDR elevation-Doppler spectra at an azimuth of 0° and a range of 25 km for a forward-looking chined conformal array.

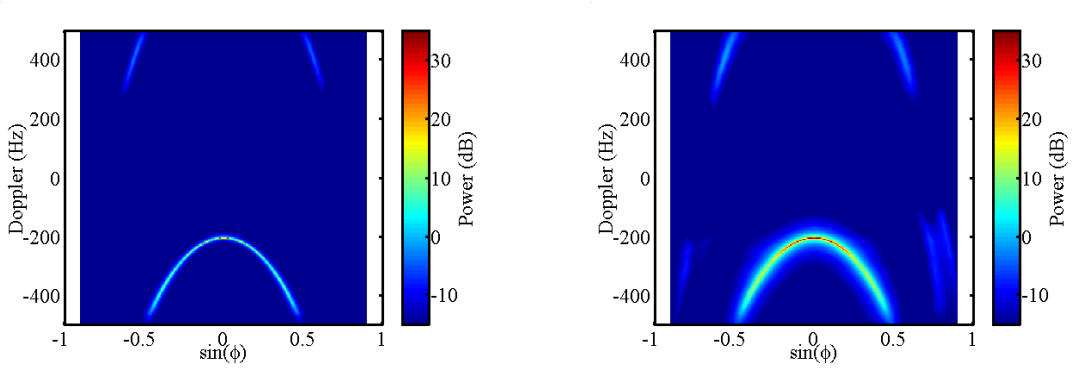

Figure 4.32. Known (left) and estimated (right) MVDR azimuth-Doppler spectra at an elevation of -26° and a range of 25 km for a forward-looking chined conformal array.

4.5. Nonadaptive Processing

Given the high estimation losses in adaptive processing, we consider nonadaptive processing as a possible solution. For the nonadaptive case, the optimal weight vector is the space-time matched filter, $\mathbf{s}_{\text{s-t,cfa}}$. This gives the clairvoyant loss term as

$$L_{s,1} = \frac{\text{SINR}_{\text{opt}}}{\text{SNR}} = \sigma_n^2 \frac{\mathbf{s}_{\text{s-t,cfa}}^H \mathbf{s}_{\text{s-t}}}{\mathbf{s}_{\text{s-t,cfa}}^H \mathbf{R}_k \mathbf{s}_{\text{s-t,cfa}}}. \tag{4.3}$$

We have no adaptive losses, since no covariance matrix estimate is required.

For this analysis, we examine two conformal geometries, the side-looking tapered canoe and the forward-looking chined radome. In Figs. 4.33, we compare total SINR loss ($L_{s,1} \cdot L_{s,2}$) for the adaptive and nonadaptive cases for the tapered-canoe array at a range of 36 km. In Fig. 4.34, we make the same comparison for the chined array at a range of 25 km. Both these results show, that even with the high estimation losses, the adaptive case still outperforms the nonadaptive case. Adaptivity is essential for acceptable performance.

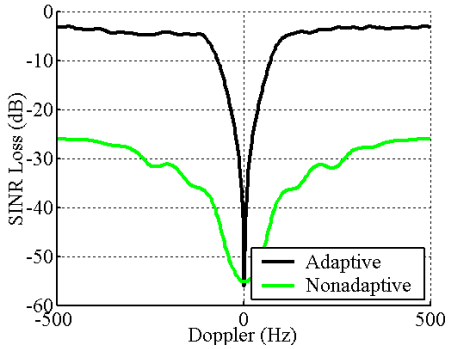

Figure 4.33. Comparison of total SINR loss for conventional adaptive and nonadaptive processing for a side-looking tapered-canoe conformal array.

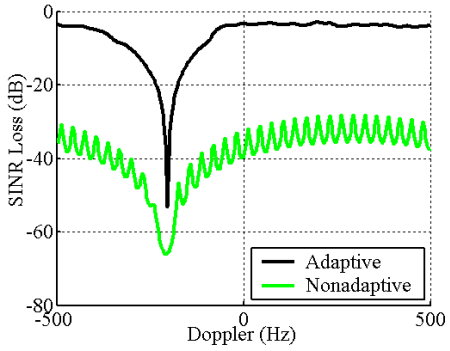

Figure 4.34. Comparison of total SINR loss for conventional adaptive and nonadaptive processing for a forward-looking chined conformal array.

4.6. Reduced-Dimension STAP

4.6.1 Formulation

A possible adaptive solution to the clutter nonstationarity problem is to use a more localized training method, resulting from the application of reduced-dimension STAP for instance, which is proposed as a possible solution to similar challenges in heterogeneous clutter environments [29-34] and bistatic STAP applications [35-37]. These techniques reduce the dimensionality of the space-time covariance matrix, leading to an implementation requiring less training data and allowing for a more local covariance-matrix estimate.

Reduced-dimension STAP algorithms traditionally come in two forms, pre-Doppler and post-Doppler. Pre-Doppler algorithms apply a dimension reduction directly in channel-pulse space. This dimension reduction lowers the DOF at the cost of Doppler and spatial resolution. Post-Doppler algorithms on the other hand, transform to Doppler and/or angle space before applying the dimension reduction. In [17], the author shows that post-Doppler reduced-dimension STAP algorithms outperform their pre-Doppler counterparts. Herein, we examine two popular post-Doppler reduced-dimension STAP techniques, the extended factored algorithm (EFA) and joint-domain localization (JDL).

In the EFA, we transform the space-time data cube to a space-Doppler data cube using standard Doppler processing methods. We then construct the space-time covariance matrix estimate using all spatial channels and a reduced number of Doppler bins as illustrated in Fig. 4.35. As a result, we preserve the Doppler resolution and effectively reduce the dimensionality of the covariance matrix [45].

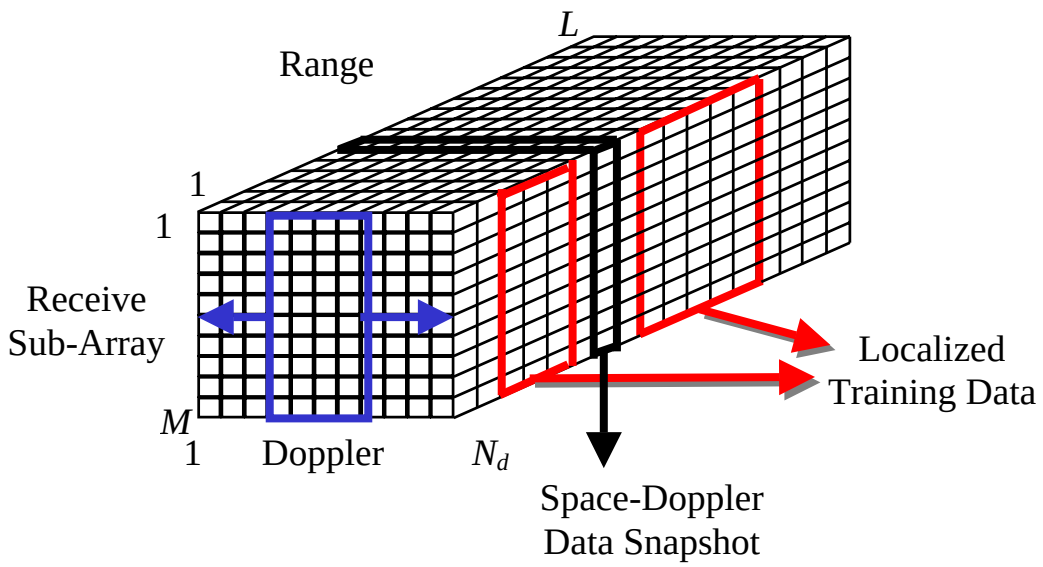

Figure 4.35. Space-Doppler covariance matrix estimation applying EFA.

For JDL, in addition to the same pulse to Doppler transformation as in EFA, we also apply a spatial transformation, wherein we transfer the spatial channel data to a reduced number of angle bins. We then construct the space-time covariance matrix using the reduced number of angle bins and a reduced number of Doppler bins as illustrated in Fig. 4.36 [46-48].

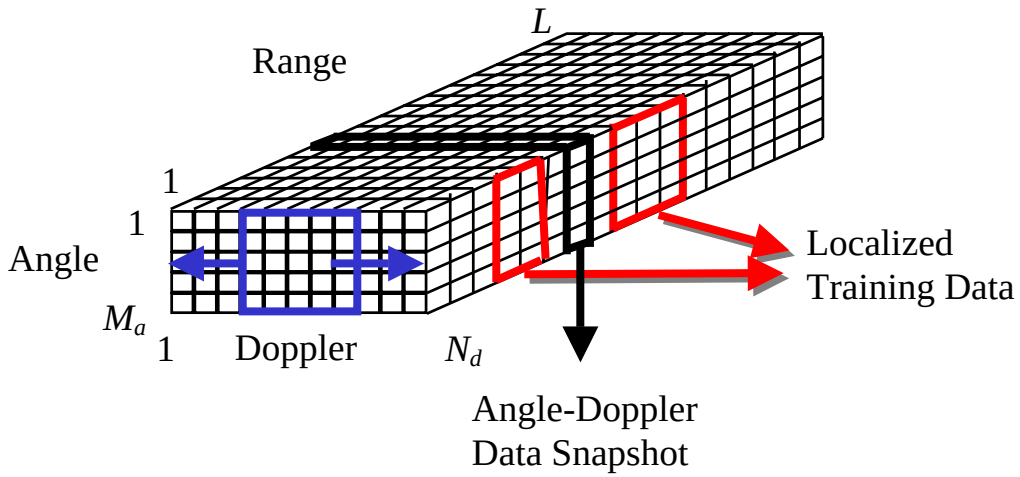

Figure 4.36. Angle-Doppler covariance matrix estimation applying JDL.

4.6.2 Results

To show the impact of reduced-dimension STAP and localized training, we analyze the following array geometries:

- Side-looking planar array
- Side-looking tapered-canoe conformal array
- Forward-looking chined conformal array

We show a comparison of full-dimension joint-domain STAP (JDSTAP), EFA, and JDL training parameters in Table 4.4.

Table 4.4. Training parameters for JDSTAP, EFA, and JDL.

Algorithm	Spatial DOF	Temporal DOF	Total DOF	Training Bins (when available)
JD STAP	10	32	320	640
EFA	10	5	50	100
JDL	5	5	25	50

As previously discussed, the side-looking planar array shown in Fig. 4.8 generates stationary clutter returns at all ranges. In the first data cube (see Table 4.3) however, we lack sufficient range bins to accurately estimate the space-time covariance matrix. A potential solution is reduced-dimension STAP. In Fig. 4.37, we compare clairvoyant and adaptive losses at a range of 28 km for JDSTAP, EFA, and JDL. First looking at the clairvoyant loss, we see slight losses in optimum performance for EFA and JDL, which result from the dimension reduction and a loss of DOF. When we look at the adaptive losses however, we see great improvement for both EFA and JDL, as we now have

adequate data to properly train. Comparing the total SINR loss shown in Fig. 4.38, we see both EFA and JDL show significant improvement.

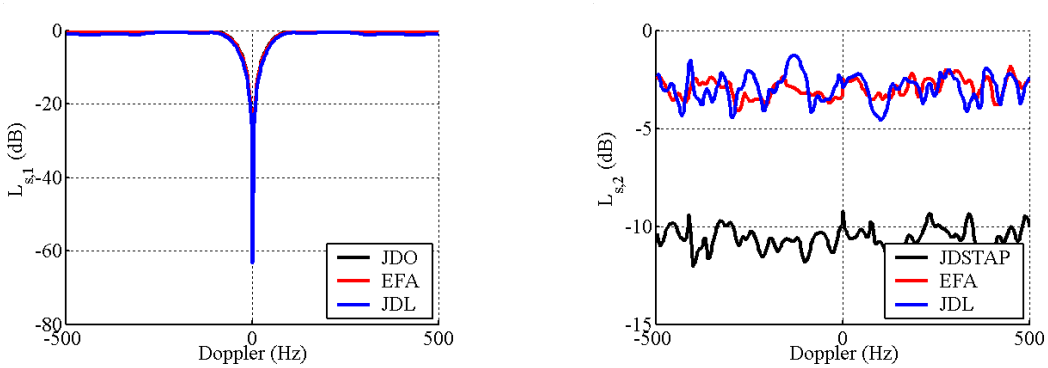

Figure 4.37. Comparison of clairvoyant and adaptive SINR loss for JDSTAP, EFA, and JDL for a side-looking planar array at a range of 28 km.

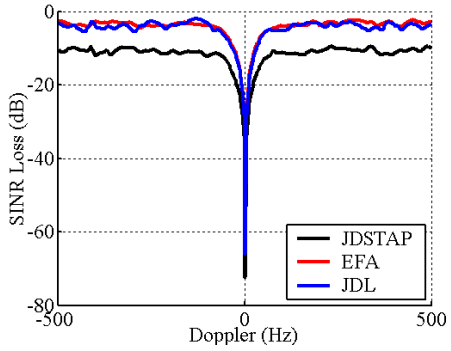

Figure 4.38. Comparison of total SINR loss for JDSTAP, EFA, and JDL for a side-looking planar array at a range of 28 km.

We show clairvoyant and adaptive SINR loss for the side-looking tapered-canoe conformal array at a range of 36 km in Fig. 4.39. The localized training results in slightly improved adaptive losses and overall losses, which we show in Fig. 5.40. We present similar results for the forward-looking chined conformal array at a range of 25 km in Figs. 4.41 and 4.42. EFA again gives some improvement in adaptive performance, whereas JDL suffers some instability and actually lowers the adaptive performance. In summary, localized training shows some improvement in mitigating nonstationary clutter. However, there is room for further improvement.

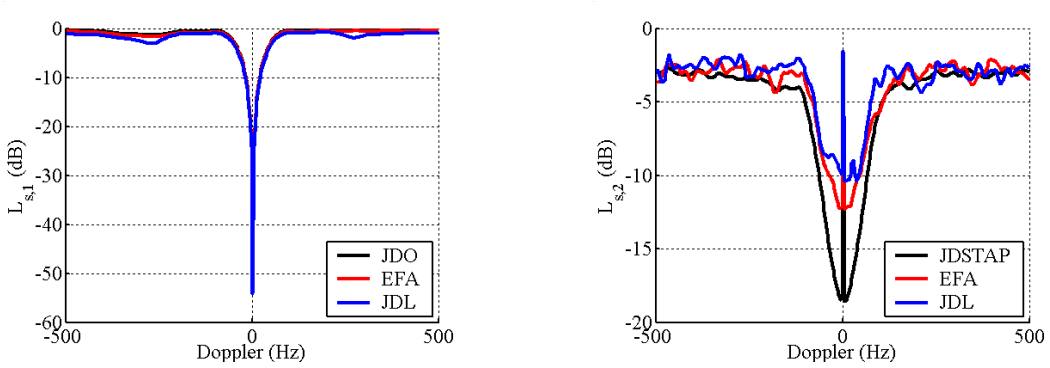

Figure 4.39. Comparison of clairvoyant and adaptive SINR loss for JDSTAP, EFA, and JDL for a side-looking tapered-canoe conformal array at a range of 36 km.

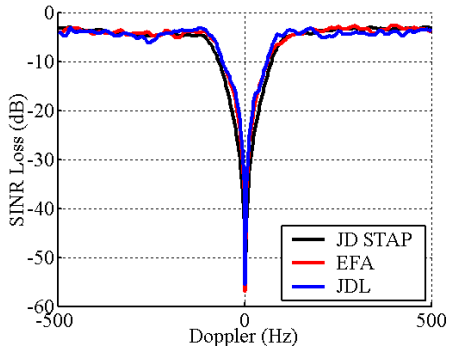

Figure 4.40. Comparison of total SINR loss for JDSTAP, EFA, and JDL for a side-looking tapered-canoe conformal array at a range of 36 km.

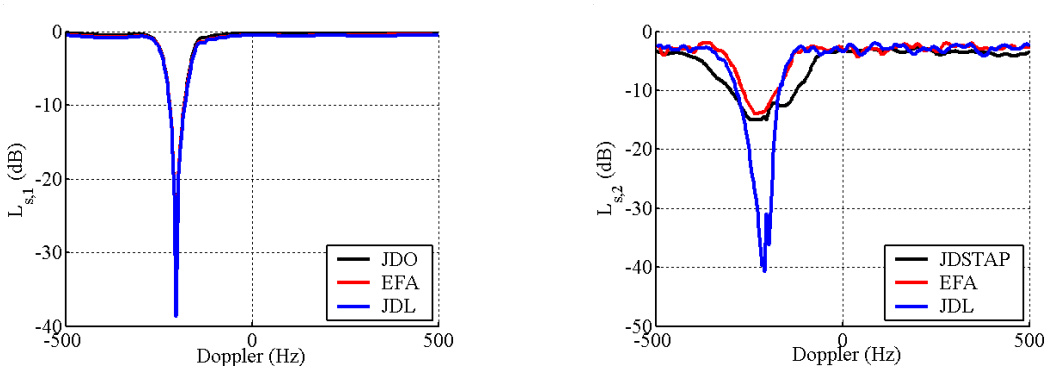

Figure 4.41. Comparison of clairvoyant and adaptive SINR loss for JDSTAP, EFA, and JDL for a forward-looking chined conformal array at a range of 25 km.

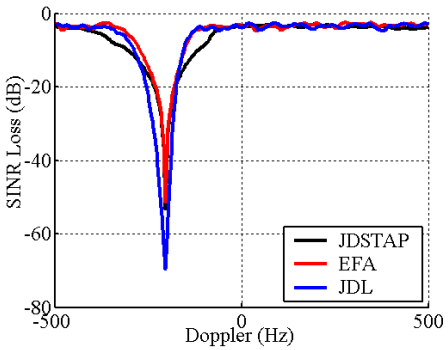

Figure 4.42. Comparison of total SINR loss for JDSTAP, EFA, and JDL for a forward-looking chined conformal array at a range of 25 km.

4.7. Time-Varying Weights

4.7.1 Formulation

In the method of time-varying weights, we modify the adaptive weight vector to allow for linear variation of the weights over range [17,49-50]. We extend both the weight vector and the data vector to include range-varying components such that the new filter has the form

$$
\begin{aligned}
y_{tv/k} &= \mathbf{w}_{\mathbf{tv}}^{H}\mathbf{x}_{\mathbf{tv}/k}; \\
\mathbf{w}_{\mathbf{tv}} &= \begin{bmatrix} \mathbf{w_0} \\ \Delta\mathbf{w} \end{bmatrix}; \\
\mathbf{x}_{\mathbf{tv}} &= \begin{bmatrix} \mathbf{x}_k \\ \gamma k\mathbf{x}_k \end{bmatrix},
\end{aligned}
\tag{4.4}
$$

where γ is a scalar [17]. We estimate the adaptive range-varying weight vector as

$$
\hat{\mathbf{w}}_{\mathbf{tv}} = \mu\hat{\mathbf{R}}_{\mathbf{tv}/k}^{-1}\begin{bmatrix} \mathbf{v}_{\mathbf{s-t,cfa}} \\ \mathbf{0} \end{bmatrix}, \tag{4.5}
$$

where $\hat{\mathbf{R}}_{\mathbf{tv},k} = \frac{1}{K}\sum_{m=1}^{K}\mathbf{x}_{\mathbf{tv}}\mathbf{x}_{\mathbf{tv}}^{H}$ is the estimate extended space-time covariance matrix, which is double the dimension of the original [17]. In summary, this extended formulation allows for linear variations over range, but at the cost of requiring twice as much training data.

4.7.2 Results

We first compare the SINR loss results for JDSTAP with and without time-varying weights. For the time-varying weights method, we require $4NM$ (1280) training bins. We show results for the chined conformal array at a range of 46 km in Fig. 4.43. This range is in data cube 3 (see Table 4.3), where we have adequate range bins available for training. The clairvoyant losses in both cases are the same, as we are not changing the optimum performance. Looking at the adaptive loss, we see excellent performance for the time-varying processor as the weights vary linearly at this range. We show similar results at a range of 25 km in Fig. 4.44. This range is in data cube 2, where we only have 650 range bins available for training. Here we see very poor adaptive performance for the time-varying weight method as we lack adequate data for training.

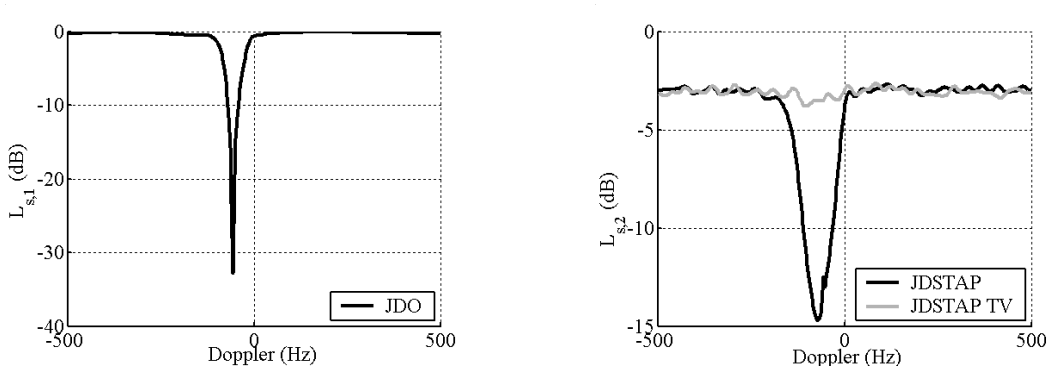

Figure 4.43. Clairvoyant and adaptive SINR loss for JDSTAP with and without time-varying weights for a forward-looking chined conformal array at a range of 46 km.

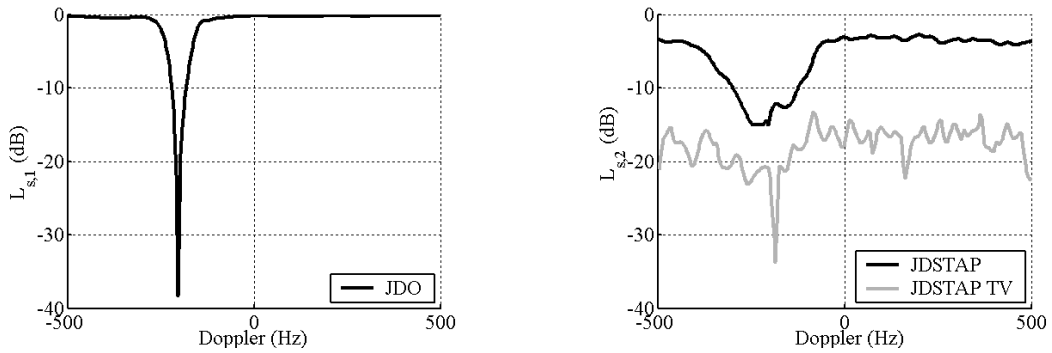

Figure 4.44. Clairvoyant and adaptive SINR loss for JDSTAP with and without time-varying weights for a forward-looking chined conformal array at a range of 25 km.

To avoid the sample support problems of time-varying weights, we can combine it with previously discussed localized-training methods. Figure 4.45 shows a comparison of JDSTAP, EFA with time-varying weights, and JDL with time-varying weights at a range of 25 km. The combination of localized training and time-varying weights gives the expected 3 dB of loss for this case, as the variation is nearly linear over this local region. We also see great improvement in the total SINR loss shown in Fig. 4.46. Looking at a closer range of 16 km as shown in Figs. 4.47 and 4.48, we again see significant improvement in the adaptive performance. At this range however, we do not

fully compensate for the clutter nonstationarity as the adaptive losses exceed 3 dB. Additionally, we see a significant loss in optimum performance, resulting from the loss of DOF from the dimension reduction.

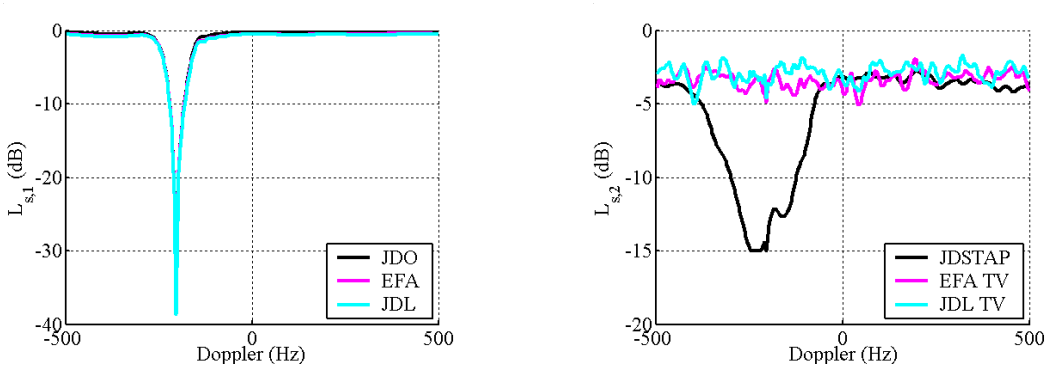

Figure 4.45. Clairvoyant and adaptive SINR loss for JDSTAP and EFA and JDL with time-varying weights for a forward-looking chined conformal array at a range of 25 km.

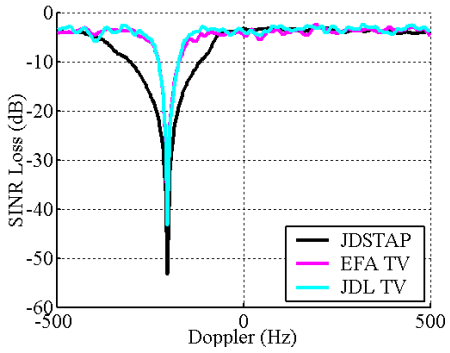

Figure 4.46. Total SINR loss for JDSTAP and EFA and JDL with time-varying weights for a forward-looking chined conformal array at a range of 25 km.

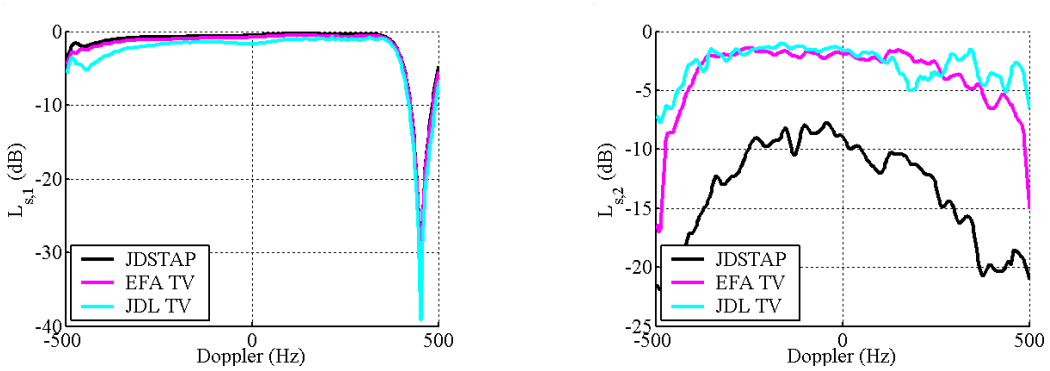

Figure 4.47. Clairvoyant and adaptive SINR loss for JDSTAP and EFA and JDL with time-varying weights for a forward-looking chined conformal array at a range of 16 km.

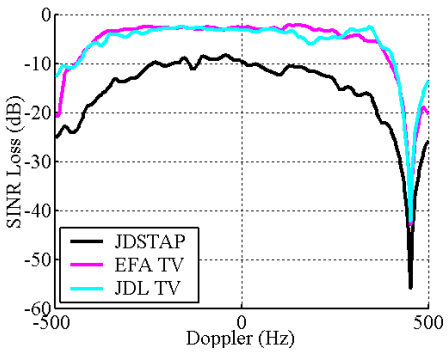

Figure 4.48. Total SINR loss for JDSTAP and EFA and JDL with time-varying weights for a forward-looking chined conformal array at a range of 16 km.

In summary, the combination of localized training and time-varying weights shows significant improvement in adaptive performance. However, these techniques alone cannot fully mitigate the nonstationary clutter, particularly at close ranges where the nonstationary behavior is highly nonlinear.

CHAPTER 5

EQUIVALENT-ULA TRANSFORMATIONS

5.1 Overview

Equivalent-ULA techniques transform non-ULA data to an equivalent-ULA form. In the literature, these techniques have been applied to sparse arrays for spatial smoothing and direction finding applications [51-53]. We extend their application to conformal arrays. Our goal is to transform nonstationary conformal array data to a stationary equivalent ULA form. We then analyze the new data as if it were a ULA. In this chapter, we present the standard equivalent ULA formulation and our application to conformal arrays. We show results for two conformal array geometries in varying orientations and conclude with some summary remarks.

5.2 Equivalent-ULA Formulation

We derive the equivalent-ULA transformation as a transformation from a set of spatial steering vectors for the given array to a set of spatial steering vectors for a new virtual ULA, i.e.,

$$\mathbf{V}_{\mathbf{s,ula}}(\boldsymbol{\theta}) = \mathbf{T}_{\mathbf{ula}}\mathbf{V}_{\mathbf{s}}(\boldsymbol{\theta}), \tag{5.1}$$

where $\boldsymbol{\theta} = \begin{bmatrix} \theta_1 & \theta_2 & \dots & \theta_{M_a} \end{bmatrix}$ is a set of M_a angles and

$\mathbf{V}_{\mathbf{s}} = \begin{bmatrix} \mathbf{v}_{\mathbf{s}}(\theta_1) & \mathbf{v}_{\mathbf{s}}(\theta_2) & \dots & \mathbf{v}_{\mathbf{s}}(\theta_{M_a}) \end{bmatrix}$ is the corresponding set of spatial steering vectors [51]. There is no restriction on the number of constraint angles we use. In the over-

constrained case where $M_a > M$, we calculate the transformation matrix using the least squares solution having the form

$$\mathbf{T_{ula}} = \mathbf{V_{s,ula}}(\boldsymbol{\Psi})\left(\mathbf{V_s}(\boldsymbol{\Psi})\right)^{\dagger}, \tag{5.2}$$

where † denotes the pseudoinverse [54].

We can apply the same transformation to the spatial snapshot to find equivalent ULA data, i.e.,

$$\mathbf{x_{s,ula}} = \mathbf{T_{ula}}\mathbf{x_s}. \tag{5.3}$$

Additionally, we can calculate the equivalent ULA spatial covariance matrix using the similar formulation

$$\mathbf{R_{s,ula}} = \mathbf{T_{ula}}\mathbf{R_s}\mathbf{T_{ula}^H}. \tag{5.4}$$

5.3 Equivalent-ULA Application to Conformal Arrays

For conformal arrays, we must consider both amplitude and phase in the equivalent-ULA transformation, giving a constraint of the form

$$\mathbf{V_{s,ula}}(\boldsymbol{\Psi}) = \mathbf{T_{ula}}\mathbf{V_{s,cfa}}(\boldsymbol{\Psi}) \tag{5.5}$$

with the least squares solution

$$\mathbf{T_{ula}} = \mathbf{V_{s,ula}}(\boldsymbol{\Psi})\left(\mathbf{V_{s,cfa}}(\boldsymbol{\Psi})\right)^{\dagger}, \tag{5.6}$$

where the angle matrix $\boldsymbol{\Psi} = \left[\boldsymbol{\psi}_1 \quad \boldsymbol{\psi}_2 \quad \ldots \quad \boldsymbol{\psi}_{M_A}\right]$ is a set of azimuth and elevation angles.

There are two critical factors in the implementation of this technique, the position of the virtual ULA phase centers and the choice of angle constraints. For our applications,

we choose a ULA with the same number of channels and similar aperture to the conformal array. The array orientation can vary, as we show in the next section, but in general we orient the ULA so the array normal is aligned with the conformal array's pre-steered direction. The selection of angle constraints is of particular interest for the conformal array case, since we must sample the full 3-D space taking into account both azimuth and elevation. For the conformal array case, we find it best to sample each range at its own elevation angle with a fixed set of azimuth angles, such that each range has its own transformation of the form

$$\begin{aligned} \mathbf{T}_{\mathbf{ula}/k} &= \mathbf{V}_{\mathbf{s,ula}}\left(\boldsymbol{\Psi}_k\right)\left(\mathbf{V}_{\mathbf{s,cfa}}\left(\boldsymbol{\Psi}_k\right)\right)^{\dagger}; \\ \boldsymbol{\Psi}_k &= \begin{bmatrix} \boldsymbol{\varphi} \\ \boldsymbol{\theta}_{\mathbf{k}} \end{bmatrix} = \begin{bmatrix} \phi_1 & \phi_2 & \dots & \phi_{M_A} \\ \theta_k & \theta_k & \dots & \theta_k \end{bmatrix}, \end{aligned} \tag{5.7}$$

where θ_k is the elevation angle corresponding to range k.

5.4 Results

We first look at a side-looking tapered-canoe conformal array, which we show with its phase centers and virtual-ULA phase centers in Fig. 5.1. We apply the equivalent-ULA transformation from (5.7) for the following three sets of azimuth angles:

- Case 1: $\boldsymbol{\varphi} = \begin{bmatrix} -16^\circ & -12^\circ & \dots & 16^\circ & 20^\circ \end{bmatrix}$, $M_a = M = 10$
- Case 2: $\boldsymbol{\varphi} = \begin{bmatrix} -48^\circ & -36^\circ & \dots & 48^\circ & 60^\circ \end{bmatrix}$, $M_a = M = 10$
- Case 3: $\boldsymbol{\varphi} = \begin{bmatrix} -60^\circ & -56^\circ & \dots & 56^\circ & 60^\circ \end{bmatrix}$, $M_a = 31$

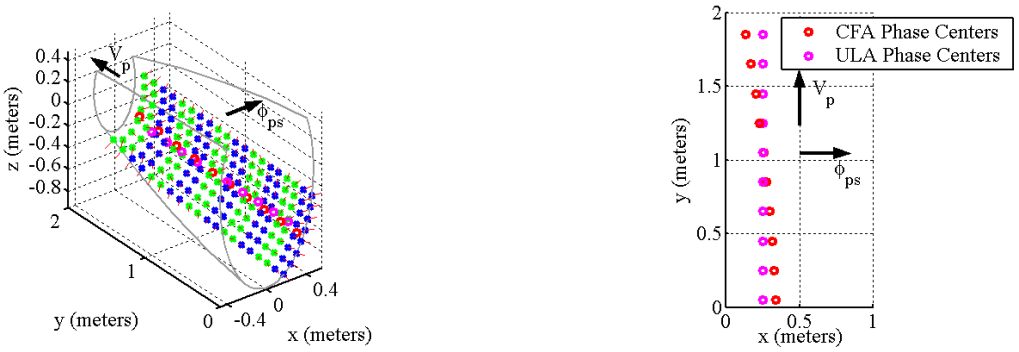

Figure 5.1. Side-looking tapered-canoe conformal array with indicated phase centers and its corresponding side-looking virtual ULA.

We first look at case 1, where we choose the number of constraint angles equal to the number of subarrays over a small angle interval. We show a comparison of clairvoyant and adaptive SINR loss at a range of 36 km for JDSTAP and the equivalent-ULA method in Fig. 5.2. The clairvoyant loss shows a perfect match between JDSTAP and the equivalent-ULA method. The adaptive loss, on the other hand, shows significant improvement for the equivalent-ULA method as we nearly achieve the 3 dB level expected for stationary data. Only at the higher Dopplers do we see a slight decrease in performance, which is a result of the limited range of the constraint angles.

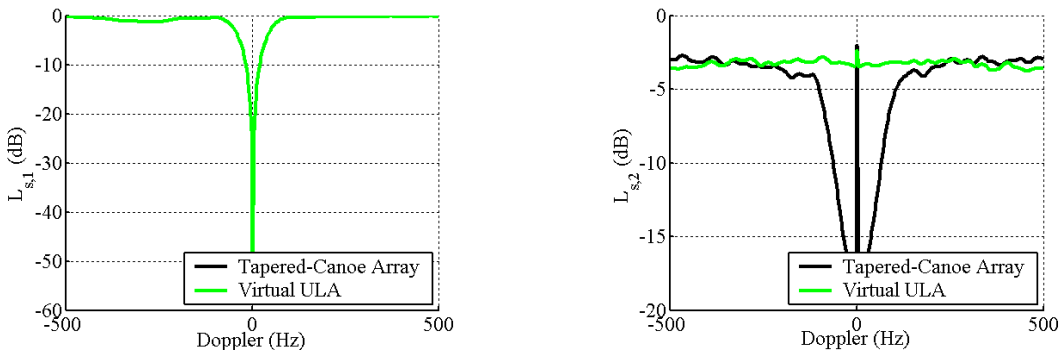

Figure 5.2. Clairvoyant (left) and adaptive (right) SINR loss at 36 km for a side-looking tapered-canoe conformal array with and without an equivalent-ULA transformation using a localized set of constraint angles.

We show the improvement further using the known and estimated MVDR spectra. We show azimuth-Doppler MVDR spectra slices for conventional processing in Fig. 5.3, and the MVDR spectra for the virtual ULA in Fig. 5.4. As discussed previously in Chapter 4, the conventional estimated spectra shows significant spreading in energy over Doppler and elevation when compared to the known spectra. For the virtual ULA however, we see a good match between the known and estimated spectra. Additionally, we see the effect of the localized angle selection, as the clutter energy appears to be centered only over the constrained angles (and the corresponding grating lobes). The JDSTAP spectra on the other hand, shows clutter energy distributed over all azimuth.

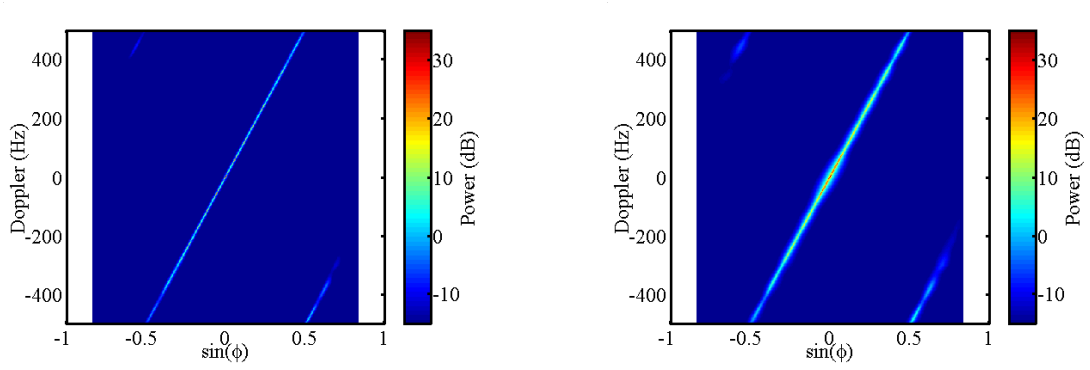

Figure 5.3. Known (left) and estimated (right) azimuth-Doppler MVDR spectra slices for a side-looking tapered-canoe conformal array.

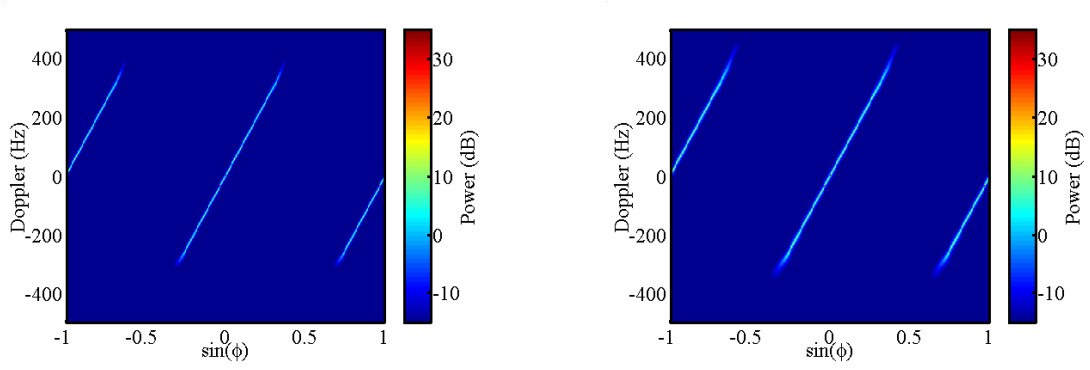

Figure 5.4. Known (left) and estimated (right) spectra for a side-looking tapered-canoe array with an equivalent-ULA transformation using a localized set of constraint angles.

To attempt to improve SINR loss performance at the higher Dopplers, we use the angle constraints for case 2, where cover a larger range of angles, while keeping the number of constraints equal to the number of subarrays. We show the clairvoyant and adaptive SINR loss plots in Fig. 5.5 and the known and estimated MVDR spectra in Fig. 5.6. Just as in the previous case, the clairvoyant loss shows a perfect match between the conventional JDSTAP and equivalent-ULA methods, whereas the adaptive loss shows improvement for the equivalent-ULA method, although not nearly as significant as the previous angle set. Looking at the known and estimated MVDR spectra, we see poor performance at the unconstrained angles, as the low angle sampling is evident.

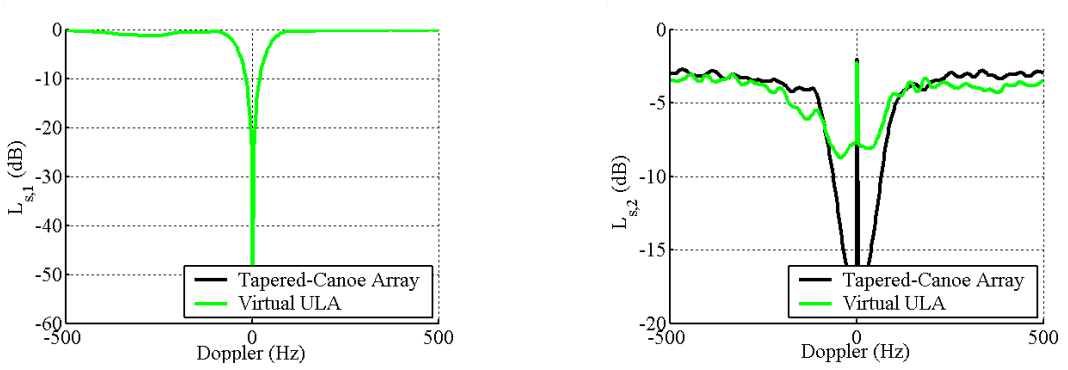

Figure 5.5. Clairvoyant (left) and adaptive (right) SINR loss at 36 km for a side-looking tapered-canoe conformal array with and without an equivalent-ULA transformation using a broad set of constraint angles.

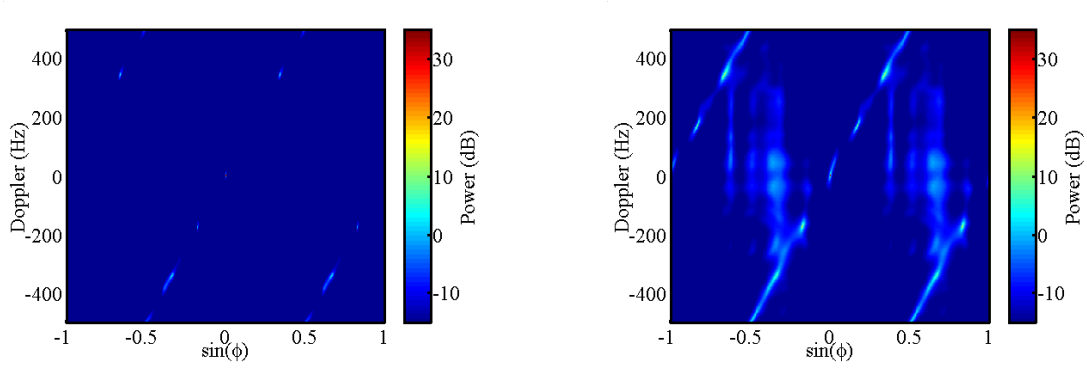

Figure 5.6. Known (left) and estimated (right) spectra for a side-looking tapered canoe array with an equivalent-ULA transformation using a broad set of constraint angles.

To attempt to keep a high angular sampling, while still covering a large angular range, we use the larger angle set for case 3. We show the clairvoyant and adaptive SINR loss plots in Fig. 5.7 and the known and estimated MVDR spectra in Fig. 5.8. The clairvoyant loss shows a significant loss in CNR for the equivalent ULA method. This loss results from steering vector mismatch caused by the least squares solution of the over-constrained problem. Looking at the MVDR spectra, we see a similar situation, where the clutter power is greatly reduced.

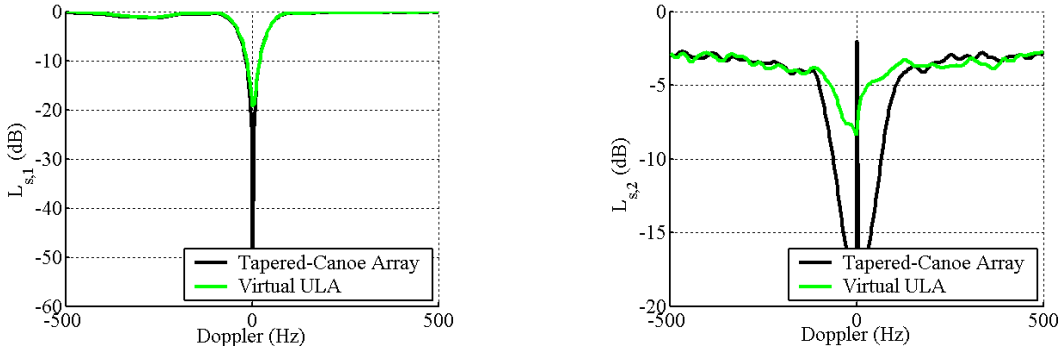

Figure 5.7. Clairvoyant (left) and adaptive (right) SINR loss at 36 km for a side-looking tapered-canoe conformal array with and without an equivalent-ULA transformation using a large number of constraint angles.

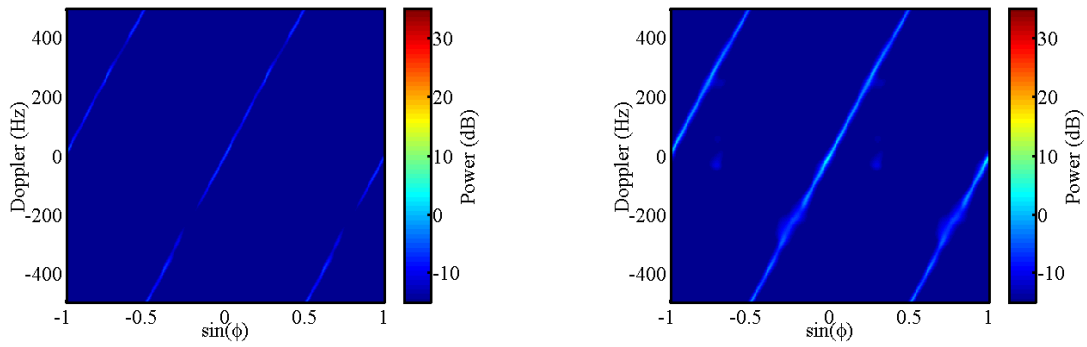

Figure 5.8. Known (left) and estimated (right) spectra for a side-looking tapered-canoe conformal array with an equivalent-ULA transformation using a large number of constraint angles.

Comparing the results for all of the angle constraint cases, we see case 1 with a local angle selection and small number of constraints has the best performance. We use this set of angle constraints in the remainder of this section.

For our next results, we again look at the tapered-canoe conformal array, but now we rotate the array 7° forward to an 83°-crab orientation as shown in Fig. 5.9. We keep the equivalent ULA the same as in the previous case, so that it also is crabbed 83°. We show clairvoyant and adaptive SINR loss results at a range of 36 km for both JDSTAP and the equivalent-ULA method in Fig. 5.10. We see no improvement in adaptive loss, since the virtual ULA itself has nonstationary clutter returns. We show the azimuth-Doppler MVDR spectra slices for JDSTAP in Fig. 5.11 and the full MVDR spectra for the equivalent-ULA method in Fig. 5.12. The estimated spectra for both cases show the spreading of clutter energy in angle and Doppler, as both the original array and the virtual ULA induce nonstationary clutter returns.

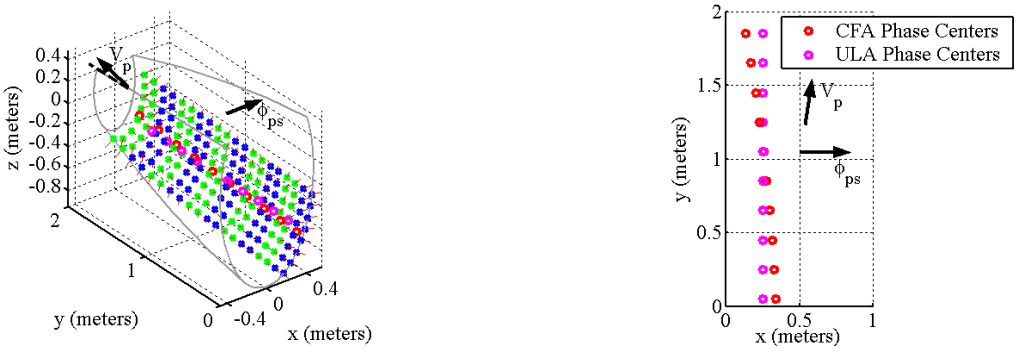

Figure 5.9. 83°-crabbed tapered-canoe conformal array with indicated phase centers and its corresponding 83°-crabbed virtual ULA.

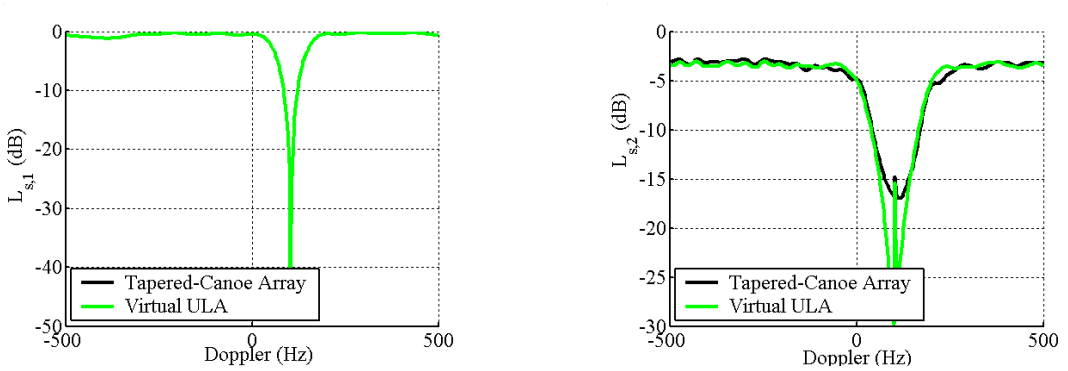

Figure 5.10. Clairvoyant (left) and adaptive (right) SINR loss at 36 km for an 83°-crabbed tapered-canoe conformal array with and without an equivalent-ULA transformation.

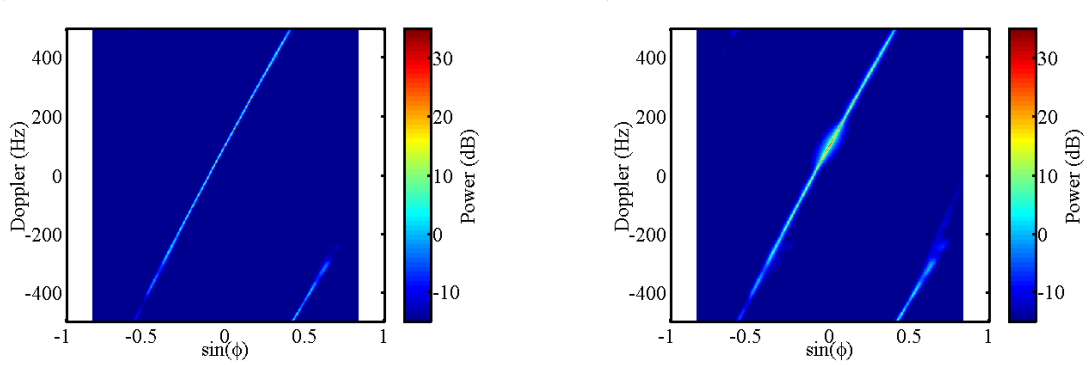

Figure 5.11. Known (left) and estimated (right) azimuth-Doppler MVDR spectra slices for an 83°-crabbed tapered-canoe conformal array.

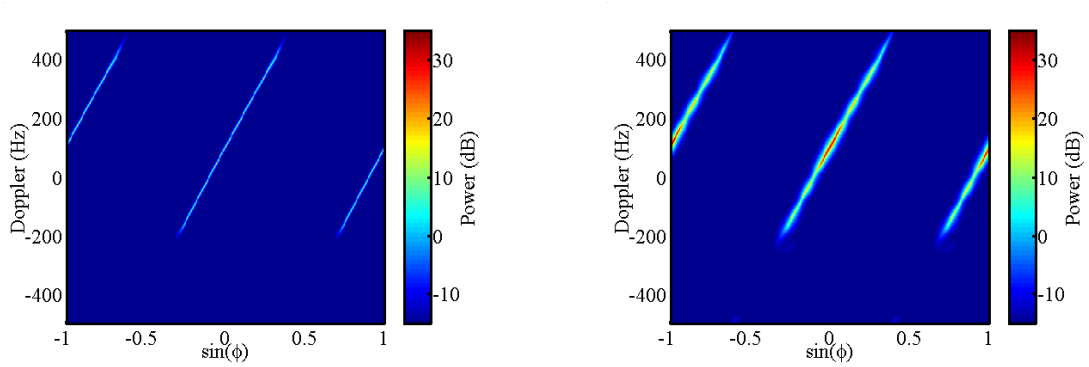

Figure 5.12. Known (left) and estimated (right) MVDR spectra for the 83°-crabbed virtual ULA of an 83°-crabbed tapered-canoe conformal array.

To compensate for the crabbed orientation of the tapered-canoe conformal array, we generate a virtual ULA rotated 7° forward so we now have a side-looking ULA. We show the new virtual ULA in Fig. 5.13. We still pre-steer the rotated equivalent ULA array at an azimuth angle of 0°, which causes the beam to be squinted 7° off boresight. We show the SINR loss results for the new virtual ULA in Fig. 5.14. The adaptive loss shows nearly stationary behavior as the loss approaches the 3 dB level. Looking at the MVDR spectra in Fig. 5.15, we again see stationary behavior as the known and estimated spectra show good agreement.

Figure 5.13. 83°-crabbed tapered-canoe conformal array with indicated phase centers and its corresponding side-looking virtual ULA.

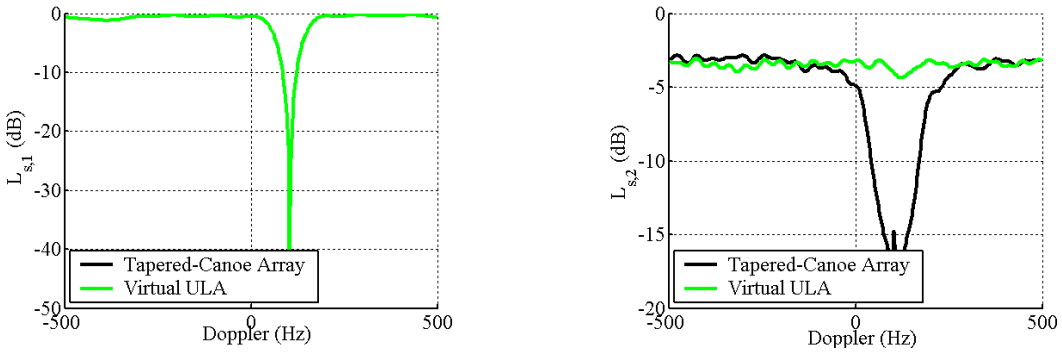

Figure 5.14. Clairvoyant (left) and adaptive (right) SINR loss at 36 km for an 83°-crabbed tapered-canoe conformal array with and without an equivalent-ULA transformation accounting for the crabbed orientation.

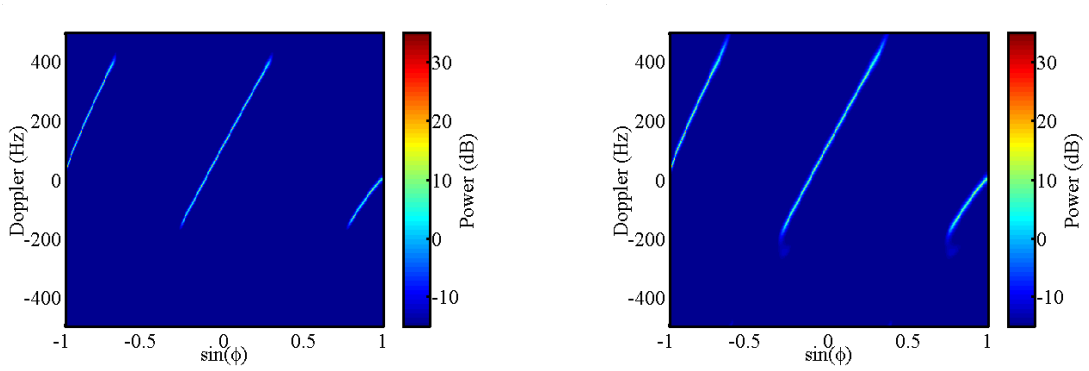

Figure 5.15. Known (left) and estimated (right) MVDR spectra for the side-looking virtual ULA of an 83°-crabbed tapered-canoe conformal array.

For the next case, we look at the forward-looking chined conformal array shown with its virtual ULA in Fig. 5.16. For comparison purposes, we also analyze the two forward-looking planar geometries shown in Fig. 5.17. For the first planar array we generate subarrays so that we have both azimuth and elevation DOF. For the second planar array, we generate subarrays so that we have only azimuth DOF, effectively making it a forward-looking ULA.

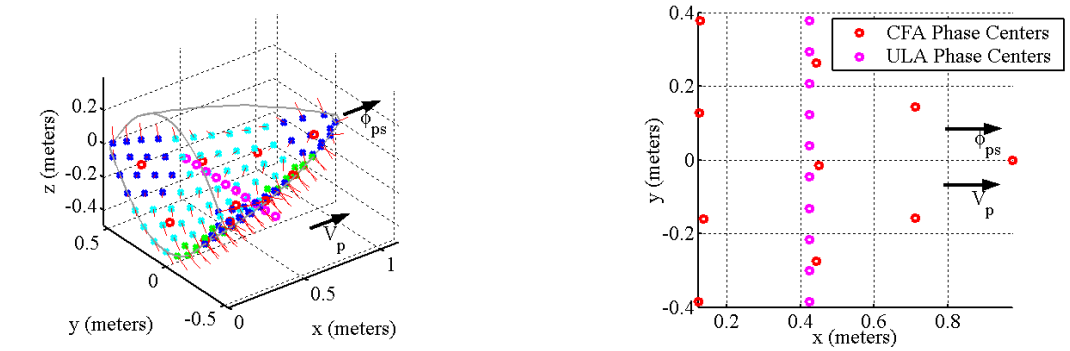

Figure 5.16. Forward-looking chined conformal array with indicated phase centers and its corresponding forward-looking equivalent-ULA.

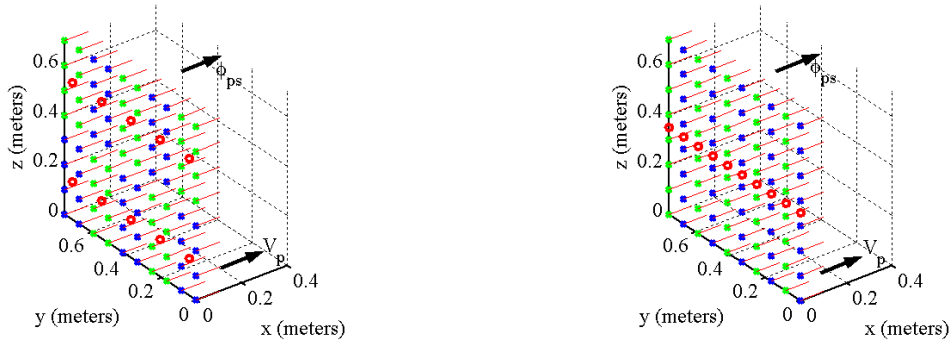

Figure 5.17. Forward-looking planar array with two different subarray schemes.

We show clairvoyant and adaptive SINR loss for the natural chined array, the equivalent-ULA-transformed chined array, the natural planar array, and the natural ULA in Fig. 5.18. First looking at the clairvoyant loss, we see similar performance for all four cases. The planar array has a slightly poorer performance than the rest, which is a result of the decreased azimuth DOF. Looking at the adaptive losses however, we see drastic differences. The natural chined array and the planar array show similar performance, whereas the virtual-ULA and the natural ULA both show higher losses. At first glance, it appears the equivalent-ULA transformation is hurting the adaptive performance. This loss, however, is somewhat misleading, as it only accounts for one look direction

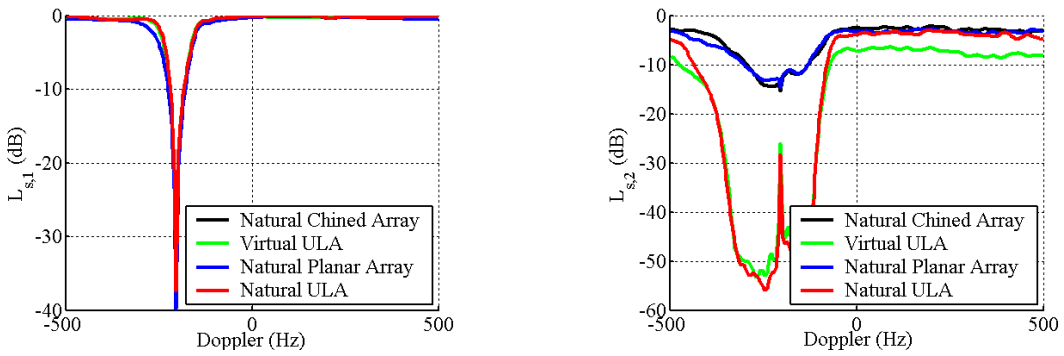

Figure 5.18. Clairvoyant (left) and adaptive (right) SINR loss at 25 km for a forward-looking chined conformal array, its corresponding forward-looking virtual array, a forward-looking planar array, and a forward-looking ULA.

We can analyze the effects of the equivalent-ULA transformation more accurately by looking at the MVDR spectra. We show the known and estimated MVDR spectra for the natural chined conformal array in Fig. 5.19. For this we include both the 3-D clutter ridge plots and an azimuth-Doppler slice at the peak elevation return. We show the known and estimated MVDR spectra for the virtual ULA in Fig. 5.20. For the natural chined array, the variation in Doppler is spread out over multiple elevation angles, whereas the virtual ULA shows the Doppler variation all in one slice. The equivalent-ULA transformation removes the elevation spread and effectively projects all returns into one ambiguous elevation angle. We see similar results in the MVDR spectra for the natural planar array and natural ULA shown in Figs. 5.21 and 5.22.

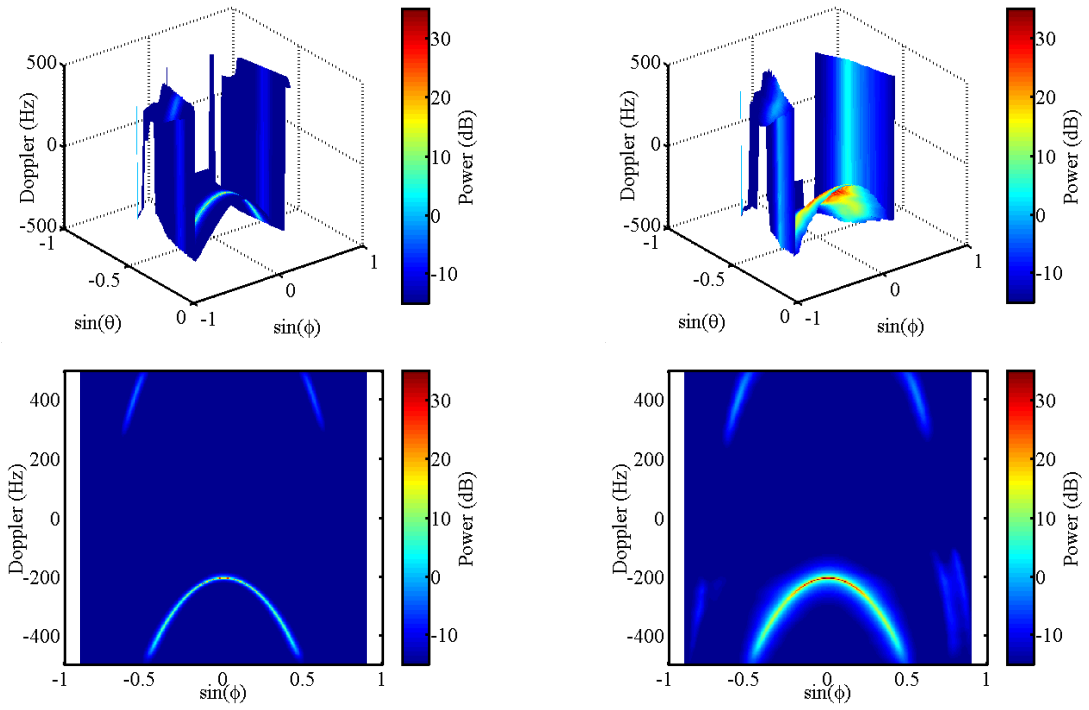

Figure 5.19. Known 3-D clutter ridge (top left), estimated 3-D clutter ridge (top right), known azimuth-Doppler MVDR slice (bottom left), and estimated azimuth-Doppler MVDR slice (bottom right) for a forward-looking chined conformal array.

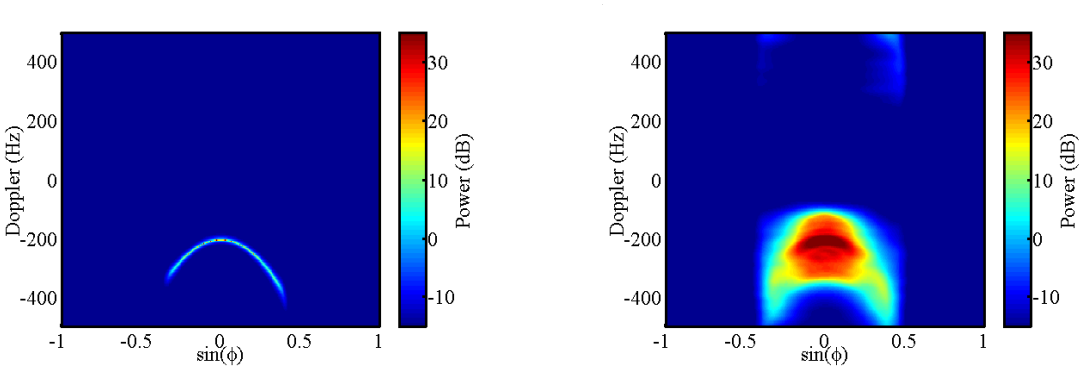

Figure 5.20. Known (left) and estimated (right) MVDR spectra for the forward-looking virtual ULA of a forward-looking chined conformal array.

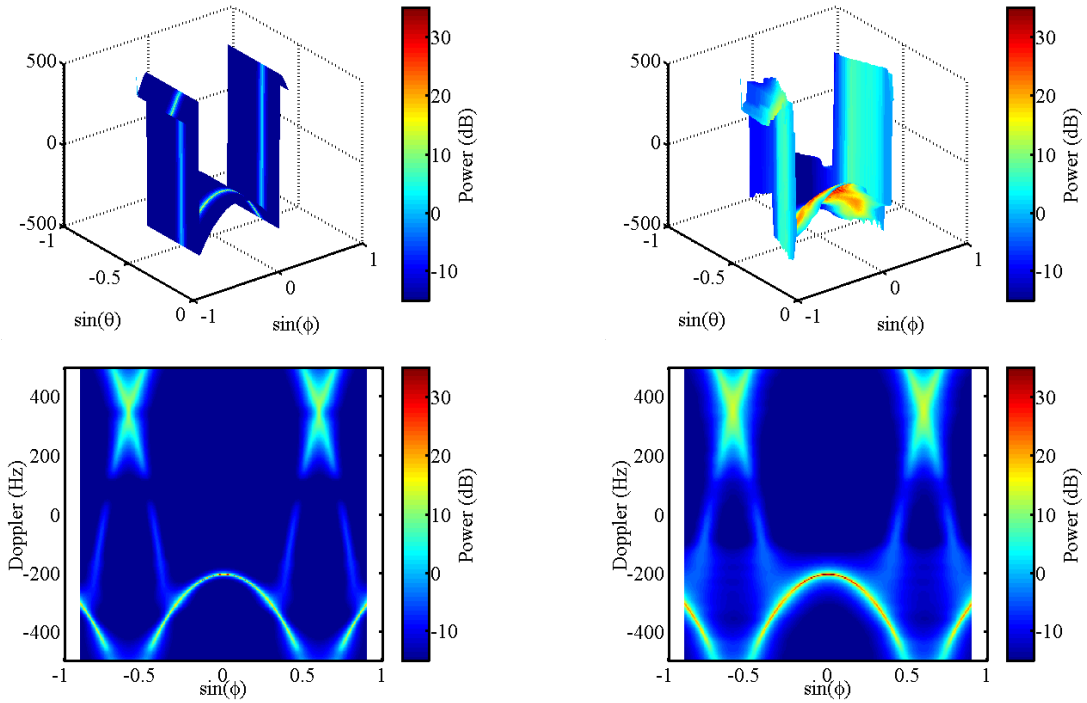

Figure 5.21. Known 3-D clutter ridge (top left), estimated 3-D clutter ridge (top right), known azimuth-Doppler MVDR slice (bottom left), and estimated azimuth-Doppler MVDR slice (bottom right) for a forward-looking planar array.

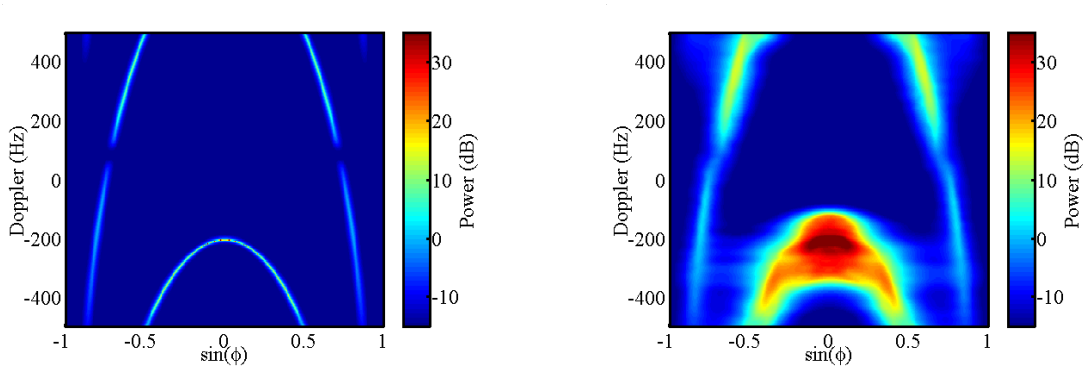

Figure 5.22. Known (left) and estimated (right) MVDR spectra for the forward-looking natural ULA.

As previously attempted for the crabbed tapered-canoe conformal array, we define the virtual ULA in a stationary side-looking orientation as shown in Fig. 5.23. For this case however, this presents a problem as we now steer the virtual ULA in an end-fire fashion, where we have very limited aperture. We show a comparison of the SINR loss results in Fig. 5.24. As expected, we see poor adaptive performance for the virtual ULA. We see this further in the virtual-ULA known and estimated MVDR spectra shown in Fig. 5.25.

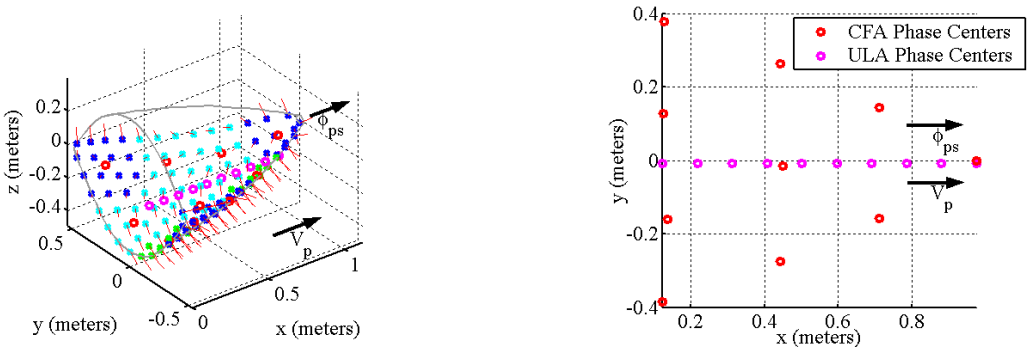

Figure 5.23. Forward-looking chined conformal array with indicated phase centers and its corresponding side-looking equivalent-ULA.

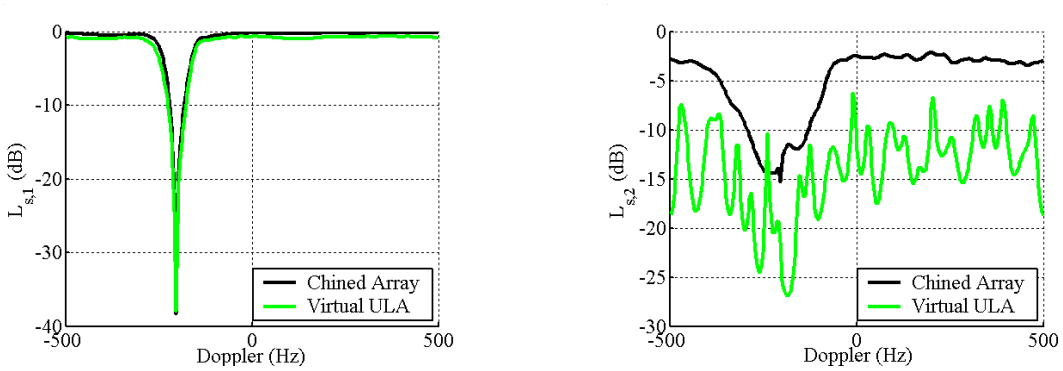

Figure 5.24. Clairvoyant (left) and adaptive (right) SINR loss at 25 km for a forward-looking chined conformal array with and without an equivalent-ULA transformation.

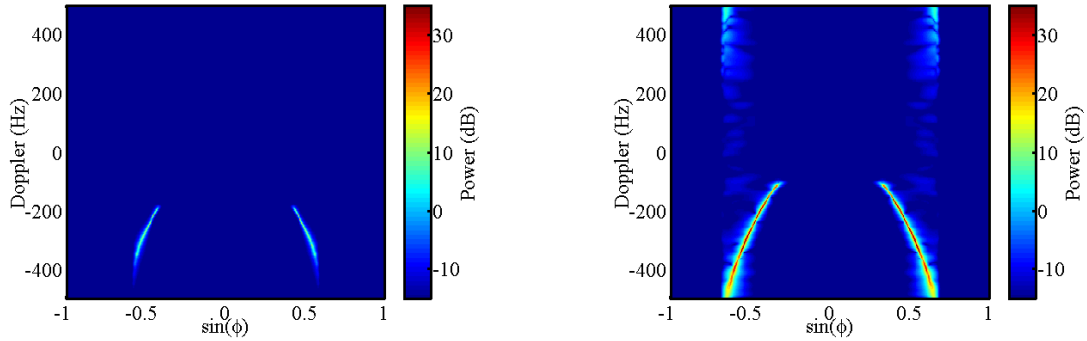

Figure 5.25. Known (left) and estimated (right) MVDR spectra for the side-looking virtual ULA of a forward-looking chined conformal array.

5.5 Summary

In this Chapter we presented equivalent-ULA transformations as a possible solution to conformal array induced nonstationary clutter returns. This transformation is very effective for the perfectly side-looking array geometries. However, if we add unknown crab, we see little improvement in performance, since the virtual ULA itself has nonstationary clutter returns. We can compensate for the array crab by defining a virtual ULA in a stationary orientation, but this requires knowledge of the array orientation, which may be inaccurate because of varying wind conditions. A potential solution to this

problem is adaptively estimating the array orientation from the clutter data. We present this technique in further detail for the angle-Doppler compensation methods discussed in Chapter 6. For the forward-looking geometries, we show the equivalent-ULA method is ineffective in mitigating the nonstationary clutter even when we define the virtual ULA in a stationary orientation.

CHAPTER 6

ANGLE-DOPPLER COMPENSATION

6.1 Overview

Angle-Doppler compensation techniques apply shifts in angle and Doppler to the secondary training data to align it with a reference. In this chapter we present a variety of angle-Doppler compensation techniques and results for conformal arrays. We begin by presenting an overview of compensation techniques as they apply to both the general array and the conformal array cases. For each compensation technique, we require knowledge of the clutter's angle-Doppler properties. In the following section, we present a variety of techniques by which we can estimate these parameters. We then present compensation results using both theoretical and adaptive estimates. Finally, we show an overall performance evaluation combining angle-Doppler compensation with those techniques discussed in previous chapters.

6.2 Angle-Doppler Compensation Techniques

6.2.1 Clutter Ridge Classes

We present two classes of clutter ridges. The first, a more complicated case, is for a general clutter ridge having no clearly defined angle-Doppler structure. We show typical synthetic 2-D and 3-D clutter ridges for this class in Figs. 6.1 and 6.2. The 2-D case corresponds to a linear array, where we can fully characterize the array spatially using a single angle. The 3-D case corresponds to any nonlinear array, where we require 2

angles to fully characterize the 3-D space. For each of these cases we show both a reference and a secondary ridge. In all of our angle-Doppler compensation strategies, we apply transformations to the secondary clutter ridge to align it with the reference.

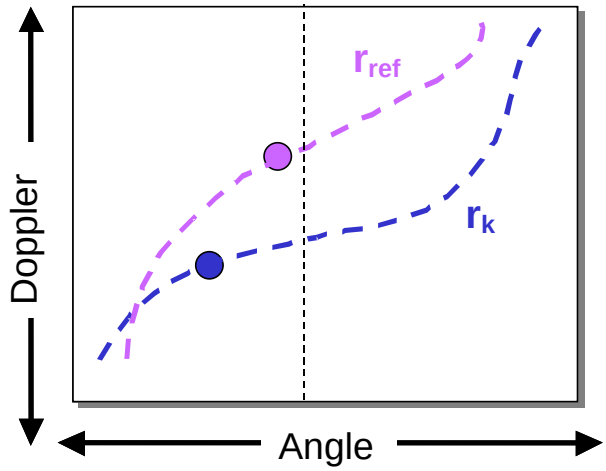

Figure 6.1. Synthetic 2-D general clutter ridge for a linear array.

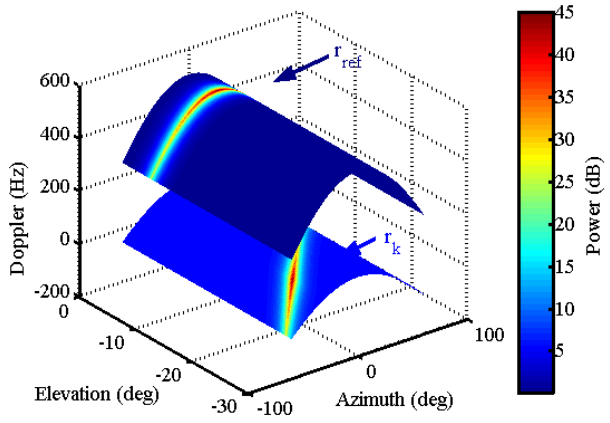

Figure 6.2. Synthetic 3-D general clutter ridge for a nonlinear array.

The second class of clutter ridge is for the active monostatic radar case, where we see clearly defined clutter angle-Doppler properties. We show example synthetic 2-D and 3-D clutter ridges for this class in Figs. 6.3 and 6.4. The 2-D example shows possible clutter characteristics for a forward-looking ULA, whereas the 3-D example represents a forward-looking conformal array. We make the assumption that these arrays have a nearly constant azimuth profile and refer to this class as such.

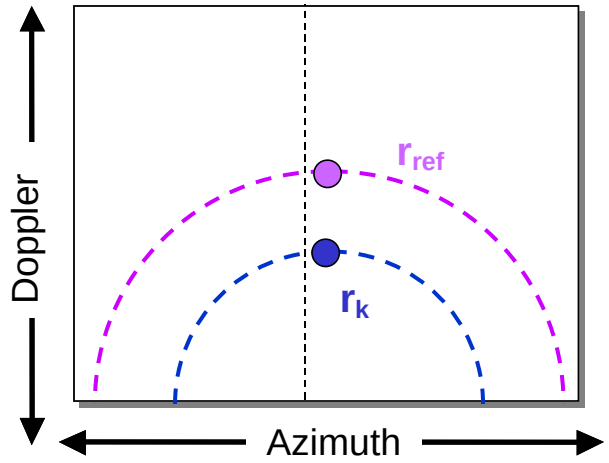

Figure 6.3. Synthetic 2-D clutter with constant-azimuth profile ridge for a linear array.

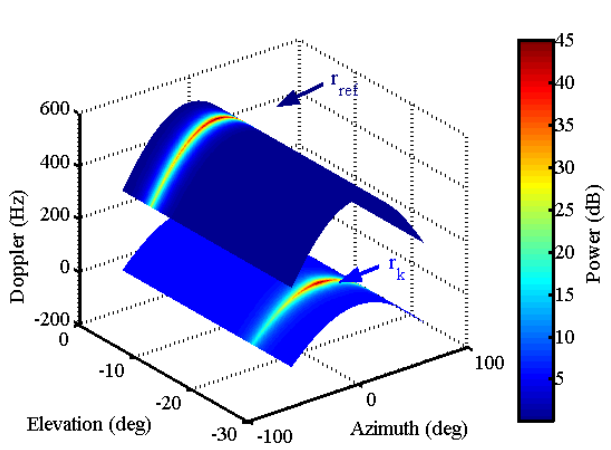

Figure 6.4. Synthetic 3-D clutter with constant-azimuth profile ridge for a nonlinear array.

6.2.2 Overview of Compensation Methods

We present a summary of angle-Doppler compensation methods in Table 6.1. For each application we select the appropriate compensation technique based on the clutter structure, array geometry, and severity of the clutter nonstationarity. For completeness, we describe all of these techniques in detail in the following sections. For of our problem, however, we only need the results for the highlighted methods.

Table 6.1. Overview of angle-Doppler compensation techniques.

Clutter Structure	Array Type	Compensation Technique	Description
General	Linear	Single-Peak Angle-Doppler Compensation	Shift a single peak in both angle and Doppler
		Multiple-Peak Angle-Doppler Compensation	Shift multiple peaks in both angle and Doppler
	Nonlinear	Single-Peak Elevation-Azimuth-Doppler Compensation	Shift a single peak in azimuth, elevation, and Doppler
		Multiple-Peak Elevation-Azimuth-Doppler Compensation	Shift multiple peaks in azimuth, elevation, and Doppler
Constant Azimuth Profile	Linear	Doppler Warping	Shift in Doppler only at a single azimuth angle
		Higher-Order Doppler Warping	Shift in Doppler only at multiple azimuth angles
	Nonlinear	Single-Azimuth Elevation-Doppler Compensation	Shift in both elevation and Doppler at a single azimuth angle
		Multiple-Azimuth Elevation-Doppler Compensation	Shift in both elevation and Doppler at multiple azimuth angles
		Hybrid Elevation-Doppler Compensation	Shift in elevation at a single azimuth angle and in Doppler at multiple azimuth angles

6.2.3 2-D Single-Peak Angle-Doppler Compensation

We illustrate the principle of 2-D single-peak angle-Doppler compensation in Fig. 6.5. We shift the peak of the secondary clutter ridge in both angle and Doppler to align it with a point on the reference clutter ridge [37,55]. Expressing this as a shift on the space-time data vector at secondary range k, we get a shifted data vector of the form

$$\mathbf{x}'_k = \mathbf{x}_k \odot \left(\mathbf{v}_{\text{s-t}}\left(f_{d/ref}, \phi_{ref} \right) ./ \mathbf{v}_{\text{s-t}}\left(f_{d/k}, \phi_k \right) \right), \tag{6.1}$$

where $f_{d/ref}$ is the reference Doppler, ϕ_{ref} is the reference angle, $f_{d/k}$ is the peak secondary Doppler, ϕ_k is the peak secondary Doppler, and $./$ indicates element-wise division [55].

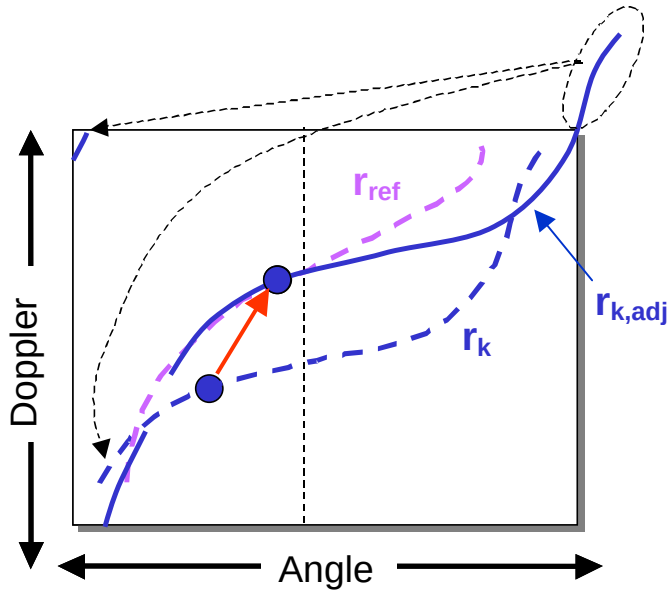

Figure 6.5. Illustration of 2-D single-peak angle-Doppler compensation.

This techniques offers the advantage that it is easy to implement, only requiring knowledge of the peak clutter Doppler and peak clutter angle. However, this technique

only aligns the clutter ridge peak, whereas other points on the clutter ridge may not be aligned.

6.2.4 3-D Single-Peak Azimuth-Elevation-Doppler Compensation

We extend the previous case to nonlinear arrays using the 3-D clutter ridge shift shown in Fig. 6.6. This technique is similar to the 2-D case in that we shift the secondary peak to align with a reference. In this case however, we must account for a shift in both azimuth and elevation as well as the varying channel gains of the spatial steering vector. Applying these shifts gives the adjusted space-time data vector as

$$\mathbf{x}'_k = \mathbf{x}_k \odot \left(\mathbf{v}_{\mathbf{s\text{-}t,cfa}} \left(f_{d/ref}, \phi_{ref}, \theta_{ref} \right) ./ \mathbf{v}_{\mathbf{s\text{-}t,cfa}} \left(f_{d/k}, \phi_k, \theta_k \right) \right), \tag{6.2}$$

where ϕ_{ref} is the reference azimuth, θ_{ref} is the reference elevation, ϕ_k is the peak secondary azimuth, and θ_k is the peak secondary elevation. Just as in the 2-D case, this technique is easy to implement, but again only aligns the clutter ridge peaks.

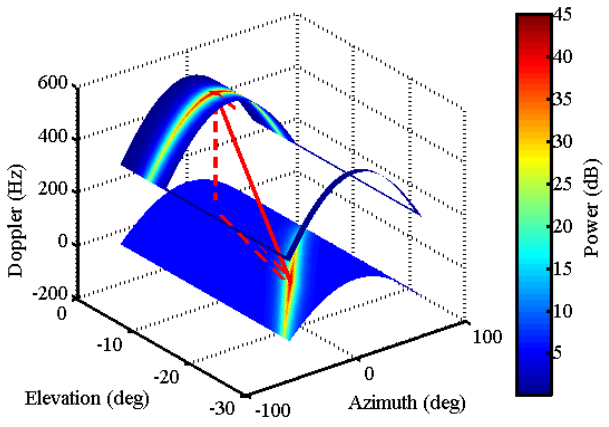

Figure 6.6. Illustration of 3-D single-peak azimuth-elevation-Doppler compensation.

6.2.5 2-D Multiple-Peak Angle-Doppler Compensation

We illustrate the principle of 2-D multiple-peak angle-Doppler compensation in Fig. 6.7. In this technique, ideally we independently shift multiple peaks in both angle and Doppler to align with multiple references. This technique presents many challenges. First, we must find and properly sort multiple peaks in the secondary clutter ridge. This requires either extensive *a priori* knowledge of the clutter characteristics or an exhaustive local maximum search. Second, shifting each peak independently requires either the use of orthogonal projections or complicated mappings [56-57].

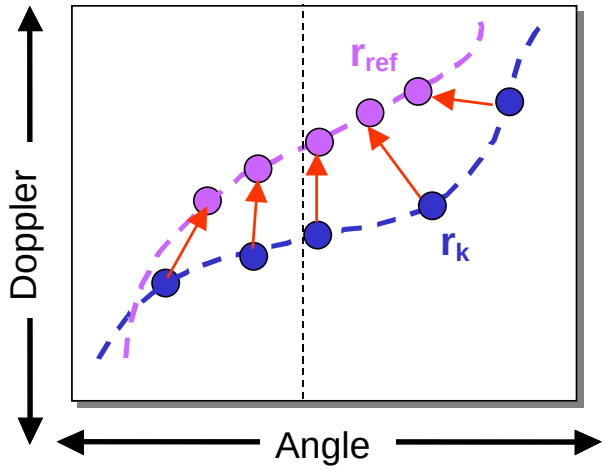

Figure 6.7. Illustration of 2-D multiple peak angle-Doppler compensation.

6.2.6 3-D Multiple-Peak Azimuth-Elevation-Doppler Compensation

We extend the previous case to nonlinear arrays using multiple 3-D shifts as shown in Fig. 6.8. In this technique we again shift multiple peaks to align with multiple references, but now require an angular shift in both azimuth and elevation. Similar to the previous

method, implementing this technique presents many challenges and is more complicated than needed to obtain suitable performance.

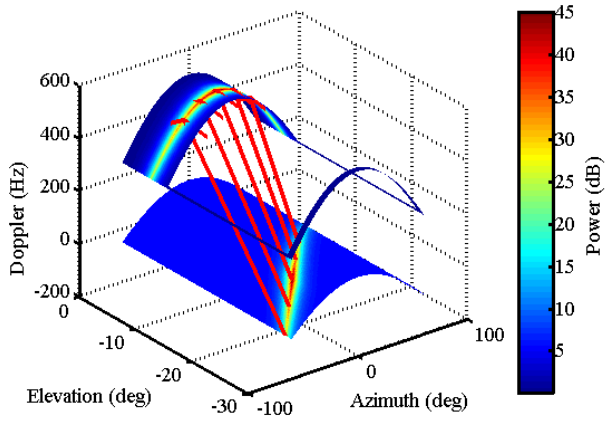

Figure 6.8. Illustration of 3-D multiple-peak azimuth-elevation-Doppler compensation.

6.2.7 2-D Doppler Warping

Thus far, all the described techniques have relied upon shifting secondary peaks to align with a reference. For this and all of the following techniques, we assume a constant-azimuth profile over range. As a result, we are now able to shift azimuth beams in lieu of peaks.

As shown in Fig. 6.9, the Doppler warping technique applies a single Doppler shift to all angles [58-60]. As a result, we align the clutter Doppler with a reference at a single azimuth angle. Expressing this as a frequency shift on the temporal snapshot at secondary range k, we get a transformation of the form

$$\mathbf{x}'_{\mathbf{t}/k} = \mathbf{x}_{\mathbf{t}/k} \odot \left(\mathbf{v}_{\mathbf{t}} \left(f_{d/ref} \right) ./ \mathbf{v}_{\mathbf{t}} \left(f_{d/k} \left(\phi_{oi} \right) \right) \right), \tag{6.3}$$

where $f_{d/k}(\phi_{oi})$ is the peak clutter Doppler at the azimuth of interest ϕ_{oi}. This technique is easy to implement and only requires knowledge of the peak clutter Doppler at the chosen angle.

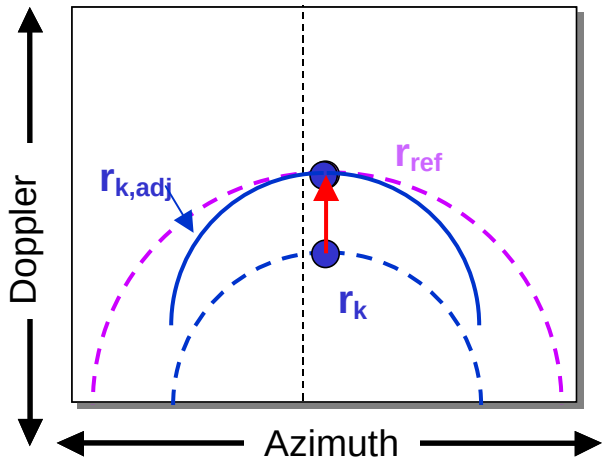

Figure 6.9. Illustration of 2-D Doppler warping.

6.2.8 3-D Single-Azimuth Elevation-Doppler Compensation

Extending Doppler warping to nonlinear arrays, we get the single-azimuth elevation-Doppler method depicted in Fig. 6.10, which gives a transformation on the space-time data vector of the form

$$\mathbf{x}'_k = \mathbf{x}_k \odot \left(\mathbf{v}_{\text{s-t,cfa}}\left(f_{d/ref}, \phi_{oi}, \theta_{ref} \right) ./ \mathbf{v}_{\text{s-t,cfa}}\left(f_{d/k}(\phi_{oi}), \phi_{oi}, \theta_k \right) \right). \tag{6.4}$$

This transformation is slightly more complicated than Doppler warping, as it requires knowledge of both peak elevation angle and the peak Doppler at the azimuth of interest.

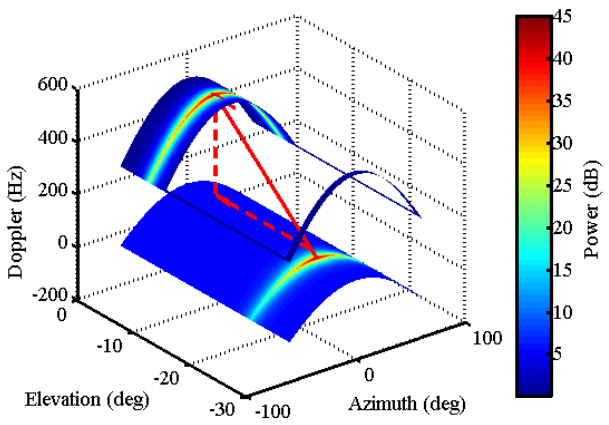

Figure 6.10. Illustration of 3-D single-azimuth elevation-Doppler compensation.

6.2.9 2-D Higher-Order Doppler Warping

Extending Doppler warping to multiple azimuth angles, we get a technique known in the literature as higher-order Doppler warping (HODW) [61]. We illustrate this technique as it is applied to a linear array in Fig. 6.11. In this technique, we align the peak clutter Doppler at multiple azimuth angles. Implementing the multiple Doppler shifts requires a transformation to beamspace of the form

$$\mathbf{B}_k = \mathbf{v}_{\mathbf{s}}^H\left(\boldsymbol{\varphi}_{\mathbf{oi}}\right)\mathbf{X}_k, \tag{6.5}$$

where $\mathbf{B}_k$ is a matrix of beamspace data, $\boldsymbol{\varphi}_{\mathbf{oi}}$ is a length M_a vector of azimuth angles, and $\mathbf{X}_k$ is the space-time data snapshot in matrix form. Next, we apply Doppler shifts to the beamspace data giving a transformation of the form

$$\mathbf{B}'_k = \mathbf{B}_k \odot \mathbf{T}_{\mathbf{d}}\left(\boldsymbol{\varphi}_{\mathbf{oi}}\right), \tag{6.6}$$

where $\mathbf{T}_{\mathbf{d}}\left(\boldsymbol{\varphi}_{\mathbf{oi}}\right)$ is a matrix of temporal steering vectors of the form

$$\mathbf{T_d}\left(\boldsymbol{\varphi}_{\mathbf{oi}}\right)=\begin{bmatrix}\left(\mathbf{v_t}\left(f_{d/ref}\left(\left[\boldsymbol{\varphi}_{\mathbf{oi}}\right]_1\right)\right)./\,\mathbf{v_t}\left(f_{d/k}\left(\left[\boldsymbol{\varphi}_{\mathbf{oi}}\right]_1\right)\right)\right)^T\\ \left(\mathbf{v_t}\left(f_{d/ref}\left(\left[\boldsymbol{\varphi}_{\mathbf{oi}}\right]_2\right)\right)./\,\mathbf{v_t}\left(f_{d/k}\left(\left[\boldsymbol{\varphi}_{\mathbf{oi}}\right]_2\right)\right)\right)^T\\ \vdots\\ \left(\mathbf{v_t}\left(f_{d/ref}\left(\left[\boldsymbol{\varphi}_{\mathbf{oi}}\right]_{M_a}\right)\right)./\,\mathbf{v_t}\left(f_{d/k}\left(\left[\boldsymbol{\varphi}_{\mathbf{oi}}\right]_{M_a}\right)\right)\right)^T\end{bmatrix}. \tag{6.7}$$

Finally, we get the shifted space-time data by transforming back from beamspace, i.e.,

$$\mathbf{X}'_k=\left[\mathbf{s}_{\mathbf{s}}^H\left(\boldsymbol{\varphi}_{\mathbf{oi}}\right)\right]^{\dagger}\mathbf{B}'_k. \tag{6.8}$$

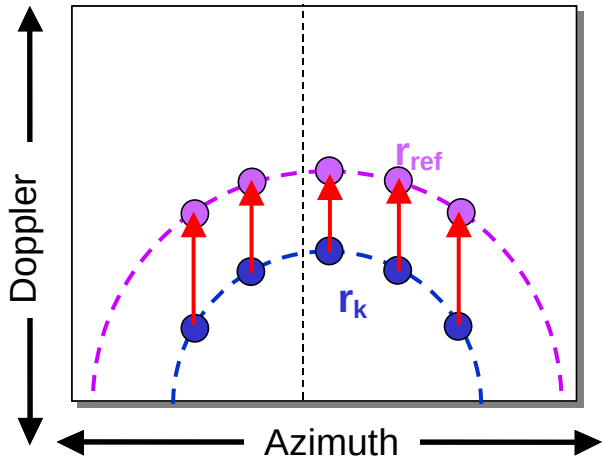

Figure 6.11. Illustration of 2-D HODW.

6.2.10 3-D Multiple-Azimuth Elevation-Doppler Compensation

We extend HODW to the 3-D case as shown in Fig. 6.12. Here we shift multiple azimuth angles in both Doppler and elevation. As was the case for the multiple peak compensation techniques described earlier, this compensation is difficult to implement, requiring complicated orthogonal projection or mapping techniques. For our problem at

hand, we do not require this level of compensation accuracy. However, we do apply the principle behind this technique in a hybrid technique described in the following section.

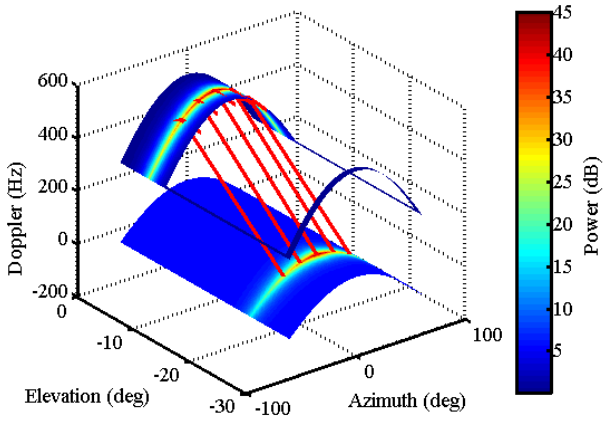

Figure 6.12. Illustration of 3-D multiple-azimuth elevation-Doppler compensation.

6.2.11 3-D Hybrid Elevation-Doppler Compensation

We present a hybrid technique as a computationally efficient way of implementing 3-D multiple-azimuth elevation-Doppler compensation. As a result of the fast-time sampling for our radar geometry, we can associate the clutter returns from each range with a limited span of elevation angles, which are also azimuth independent. This allows us to compensate the spatial snapshot in elevation using a single-azimuth transformation of the form

$$\mathbf{x}'_{\mathbf{s}/k} = \mathbf{x}_{\mathbf{s}/k} \odot \left(\mathbf{v}_{\mathbf{s,cfa}} \left(\phi_{oi}, \theta_{ref} \right) ./ \mathbf{v}_{\mathbf{s,cfa}} \left(\phi_{oi}, \theta_k \right) \right). \tag{6.9}$$

This transformation is not completely accurate, since the spatial steering vector varies over azimuth. However, we generally choose a localized azimuth span for compensation, where the change in the spatial steering vector is negligible.

After applying the single-azimuth elevation shift, we apply a multiple-azimuth Doppler shift as depicted in Fig. 6.13. Updating the HODW transformation for the nonlinear array case, we get the beamspace transformation

$$\mathbf{B}_k = \mathbf{v}_{\mathbf{s,cfa}}^H \left(\boldsymbol{\varphi}_{\mathbf{oi}}, \theta_{ref} \right) \mathbf{X}'_k. \tag{6.10}$$

We then apply the Doppler transformation from (6.6) and transform back from beamspace to get the final doubly shifted data

$$\mathbf{X}''_k = \left[\mathbf{s}_{\mathbf{s,cfa}}^H \left(\boldsymbol{\varphi}_{\mathbf{oi}}, \theta_{ref} \right) \right]^{\dagger} \mathbf{B}'_k. \tag{6.11}$$

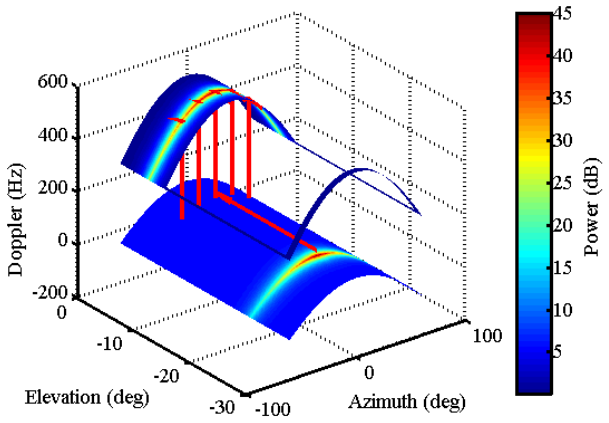

Figure 6.13. Illustration of 3-D hybrid elevation-Doppler compensation.

6.3 Parameter Estimation Techniques

As shown in the previous section, angle-Doppler compensation techniques require some knowledge of the clutter ridge. In this section, we present the following two approaches for estimating these parameters:

- Theoretical: Calculate parameters from theoretical equations and *a priori* knowledge
- Adaptive: Estimate parameters from space-time data

6.3.1 Theoretical Estimates

For the theoretical estimates, we use *a priori* knowledge of the platform height, slant range, and velocity vector to calculate the required parameters. We apply this technique to the constant azimuth profile clutter class compensation methods, where we are given a vector of azimuth angles of interest, $\boldsymbol{\varphi}_{\mathbf{oi}}$.

For the elevation angle calculation, we assume that we have a smooth spherical earth with radius R_E. Taking into account the platform height h and the slant range r_k, gives an elevation angle of

$$\theta_k = \cos^{-1}\left(\frac{h^2 + 2R_E h + r_k^{\,2}}{2r_k\left(h + R_E\right)}\right) - \frac{\pi}{2}. \tag{6.12}$$

We calculate the peak clutter Doppler frequency using the platform velocity vector $\mathbf{v}_\mathbf{p}$, the calculated elevation angle θ_k, and the given azimuth angles, which gives

$$f_{d/k,m} = \frac{2}{\lambda}\mathbf{v}_\mathbf{p}^T\mathbf{k}\left(\theta_k, \left[\boldsymbol{\varphi}_{\mathbf{oi}}\right]_m\right). \tag{6.13}$$

These calculations provide a straightforward means of estimating the required parameters. In a simulation environment, they offer an excellent means of testing and evaluating the performance of the angle-Doppler compensation methods. In a real data environment however, they may suffer from insufficient and/or inaccurate *a priori* information.

6.3.2 Adaptive Estimates

For conformal-array angle-Doppler compensation, we require estimates of the peak clutter elevation angle and the peak clutter Doppler at the given azimuth angles. In this section, we present fully adaptive techniques for estimating these parameters. We first show a singe effective technique for estimating the peak clutter elevation angle and then show several techniques for estimating the peak clutter Doppler.

The clutter elevation angle is the easier parameter to estimate, as the clutter returns for each range bin are generally constrained to a limited range of elevation angles. To estimate the peak clutter elevation angle, we construct a spatial covariance matrix estimate over the N pulses, i.e.,

$$\hat{\mathbf{R}}_{\mathbf{s}} = \frac{1}{N}\sum_{n=1}^{N} \mathbf{x}_{\mathbf{s}/n}\mathbf{x}_{\mathbf{s}/n}^{H}, \tag{6.14}$$

where $\mathbf{x}_{\mathbf{s}/n}$ is a spatial data snapshot from pulse n. For an accurate estimate, we require more pulses than spatial channels, which generally is the case for most radar systems. In the event that we have insufficient pulses for an accurate estimate, we can either apply reduced-dimension methods or use multiple range bins. Of course by using multiple range bins, we create some bias in our results, as the elevation angle properties vary with range. After forming the estimated spatial covariance matrix, we estimate the peak elevation angle using

$$\theta_{\max} = \arg\max_{\theta} \mathbf{w}_{\mathbf{s}}^{H}\left(\theta,\phi_{ps}\right)\hat{\mathbf{R}}_{\mathbf{s}}\mathbf{w}_{\mathbf{s}}\left(\theta,\phi_{ps}\right), \tag{6.15}$$

where the spatial weight vector $\mathbf{w}_{\mathbf{s}}$ can be calculated by one of several techniques (conventional beamforming, MVDR, MUSIC) [24].

The clutter Doppler, on the other hand, varies significantly over azimuth angle. This complicates the estimation problem greatly, as we have greater diversity in each local space-time data snapshot. We propose the three estimation techniques shown in Table 6.2.

Table 6.2. Overview of adaptive Doppler estimation techniques.

Estimation Technique	Covariance Matrix Estimate	Comments
Doppler Processing	Form temporal covariance matrix estimate over all spatial channels	Estimates peak Doppler over all azimuth angles giving no azimuth control
Independent Space-Time Processing	Beamform spatial data to a single azimuth beam and form temporal covariance matrix estimate	Requires temporal dimension reduction and training over multiple ranges
Joint Space-Time Processing	Form space-time covariance matrix estimate over channels and pulses	Requires dimension reduction in channels and pulses and ULA geometry

For the Doppler processing technique, we estimate the temporal covariance matrix over all spatial channels. Since we typically have more pulses than channels, we must use a reduced number of pulses and/or train over multiple ranges. This gives a temporal covariance matrix of the form

$$\begin{aligned} \hat{\mathbf{R}}_{\mathbf{t}} &= \frac{1}{KM\left(N-N_r+1\right)}\sum_{k=1}^{K}\sum_{m=1}^{M}\sum_{n=1}^{N-N_r+1}\mathbf{x}_{\mathbf{t},\mathbf{r}/k,m,n}\mathbf{x}_{\mathbf{t},\mathbf{r}/k,m,n}^{H}; \\ \mathbf{x}_{\mathbf{t},\mathbf{r}/k,m,n} &= \left[\begin{bmatrix}\mathbf{x}_{\mathbf{t}/k,m}\end{bmatrix}_{n} \quad \begin{bmatrix}\mathbf{x}_{\mathbf{t}/k,m}\end{bmatrix}_{n+1} \quad \cdots \quad \begin{bmatrix}\mathbf{x}_{\mathbf{t}/k,m}\end{bmatrix}_{n+N_r-1}\right]^{T}, \end{aligned} \tag{6.16}$$

where N_r is the reduced number of pulses, $\mathbf{x}_{\mathbf{t},\mathbf{r}/k,m,n}$ is a reduced version of the temporal snapshot $\mathbf{x}_{\mathbf{t}/k,m}$ at range bin k and channel m. We estimate the peak Doppler in a manner similar to the spatial case, i.e.,

$$f_{d,\max} = \arg\max_{f_d} \mathbf{w}_{\mathbf{t}}^H(f_d)\hat{\mathbf{R}}_{\mathbf{t}}\mathbf{w}_{\mathbf{t}}(f_d), \tag{6.17}$$

which again can be calculated from one of several techniques.

As previously stated, the clutter Doppler varies over azimuth. This Doppler processing technique is independent of azimuth and only estimates the peak clutter Doppler over all azimuth. As a result, we only estimate the azimuth in the pre-steer direction (the typical location of the peak). Additionally, this technique generally has very poor performance because of the wide range of clutter Doppler.

For the independent space-time processing technique, we first beamform the data to the specified angle of interest, i.e.,

$$\mathbf{b}_{\mathbf{t}} = \left(\mathbf{v}_{\mathbf{s,cfa}}^H(\boldsymbol{\psi}_{\mathbf{oi}})\mathbf{X}\right)^T, \tag{6.18}$$

where $\mathbf{b}_{\mathbf{t}}$ is a temporal snapshot at angle $\boldsymbol{\psi}_{\mathbf{oi}}$ and $\mathbf{X}$ is the space-time data snapshot in matrix form. We then form a temporal covariance matrix again estimating over a reduced number of pulses and multiple ranges, i.e.,

$$\begin{aligned}\hat{\mathbf{R}}_{\mathbf{t}} &= \frac{1}{K(N-N_r+1)}\sum_{k=1}^{K}\sum_{n=1}^{N-N_r+1}\mathbf{b}_{\mathbf{t,r}/k,n}\mathbf{b}_{\mathbf{t,r}/k,n}^H; \\ \mathbf{b}_{\mathbf{t,r}/k,n} &= \left[\left[\mathbf{b}_{\mathbf{t}/k}\right]_n \quad \left[\mathbf{b}_{\mathbf{t}/k}\right]_{n+1} \quad \cdots \quad \left[\mathbf{b}_{\mathbf{t}/k}\right]_{n+N_r-1}\right]^T.\end{aligned} \tag{6.19}$$

Finally we estimate the peak clutter Doppler from (6.17).

This technique has an advantage over the prior one in that we have a smaller range of clutter Doppler over which to estimate. Additionally, we can estimate the peak Doppler at varying azimuth angles. However, this technique greatly reduces the quantity of local training data, and we must train over a more reduced temporal space and/or over more ranges.

For the joint space-time technique, we form a joint-domain space-time covariance matrix estimate as described in [55]. We use both a reduced number of spatial channels and a reduced number of pulses to form the estimate. The spatial dimension reduction requires a ULA geometry, since the channel phase shifts must be constant between adjacent channels. As a result, for non-ULA geometries, we must first apply an equivalent-ULA transformation as described in Chapter 5. After applying the equivalent ULA transformation, we form a space-time covariance matrix of the form

$$\hat{\mathbf{R}} = \frac{1}{K\left(M - M_r + 1\right)\left(N - N_r + 1\right)} \sum_{k=1}^{K} \sum_{m=1}^{(M-M_r+1)} \sum_{n=1}^{N-N_r+1} \mathbf{x}_{\mathbf{s-t,r}/k,m,n} \mathbf{x}_{\mathbf{s-t,r}/k,m,n}^{H};$$

$$\mathbf{x}_{\mathbf{s-t,r}/k,m,n} = \mathrm{vec}\begin{bmatrix} [\mathbf{X}]_{m,n} & [\mathbf{X}]_{m,n+1} & \cdots & [\mathbf{X}]_{m,n+N_r-1} \\ [\mathbf{X}]_{m+1,n} & [\mathbf{X}]_{m+1,n+1} & \cdots & [\mathbf{X}]_{m+1,n+N_r-1} \\ \vdots & \vdots & \ddots & \vdots \\ [\mathbf{X}]_{m+M_r-1,n} & [\mathbf{X}]_{m+M_r-1,n+1} & \cdots & [\mathbf{X}]_{m+M_r-1,n+N_r-1} \end{bmatrix}, \tag{6.20}$$

where the vec operation concatenates the matrix columns into a single column vector. From this space-time covariance matrix estimate, we find the peak clutter Doppler at the angle of interest ϕ_{oi} using the joint space-time formulation

$$f_{d,\max} = \arg\max_{f_d} \mathbf{w}_{\mathbf{s-t}}^{H}\left(f_d, \phi_{oi}\right) \hat{\mathbf{R}} \mathbf{w}_{\mathbf{s-t}}\left(f_d, \phi_{oi}\right). \tag{6.21}$$

This technique offers the advantage of a joint space-time formulation, which generally performs better than its cascade counterparts [46]. For general conformal array geometries however, this technique requires an equivalent-ULA transformation, which can create some instabilities as previously discussed in Chapter 5.

6.4 Parameter Estimation Results

6.4.1 Elevation Angle Estimates

In this section, we present theoretical and adaptive estimate results of the peak clutter elevation angle for the planar and chined arrays shown in Fig. 6.14. We evaluate the performance of each technique in terms of the adaptive estimate root mean square (RMS) error with respect to the theoretical value. For computational reasons, Monte Carlo simulations are not feasible for these calculations. As an alternative, we average the errors over the training region. We show the error results in Table 6.3.

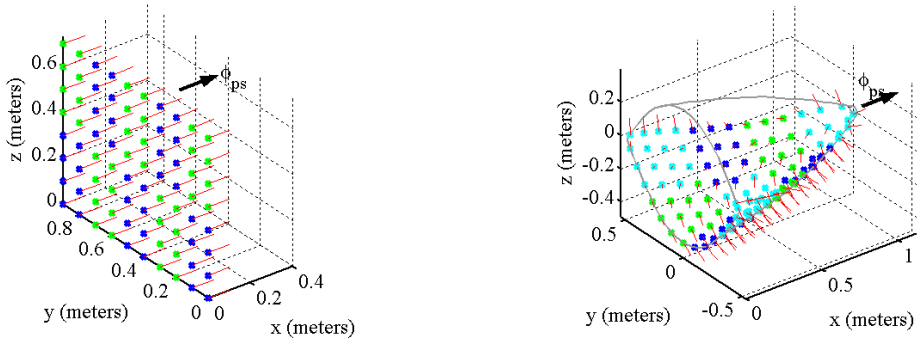

Figure 6.14. Array geometries used for adaptive clutter elevation angle estimates.

Table 6.3. RMS errors of adaptive clutter elevation angle estimates.

Array Geometry	Estimation Technique	Estimate RMS Error
Planar	Conventional	0.04°
	MVDR	0.05°
	MUSIC	0.05°
Chined	Conventional	0.25°
	MVDR	0.08°
	MUSIC	0.06°

We show theoretical and adaptive elevation angle estimate results for the planar array in Fig. 6.15. For the adaptive results, we apply conventional nonadaptive beamforming, MVDR, and MUSIC. The first plot shows output power over elevation angle at a range of 25 km. For all three techniques, we see grating lobes, which result from the spacing between the subarray phase centers. Applying very limited *a priori* knowledge, we can properly select the correct peak. The plot on the right shows the actual elevation angle estimates over the training region. All three adaptive cases show excellent agreement with the theoretical values, which is reflected by the low RMS errors shown in Table 6.3.

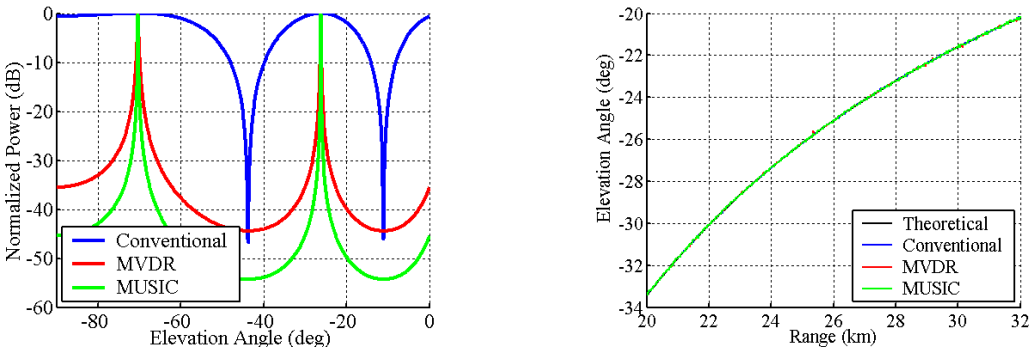

Figure 6.15. Adaptive elevation power plots (left) and range estimates (right) for a planar array.

We show theoretical and adaptive elevation angle estimate results for the chined conformal array in Fig. 6.16. First looking at the power plots, we see greatly reduced grating lobes. For this array, the subarray phase centers are spaced at a distance greater than $\lambda/2$, but the nonlinear positioning minimizes the grating-lobe effect. Looking at the range-estimate plot, we see varying performances for the estimation techniques.

MVDR and MUSIC both perform well, whereas conventional beamforming shows higher errors.

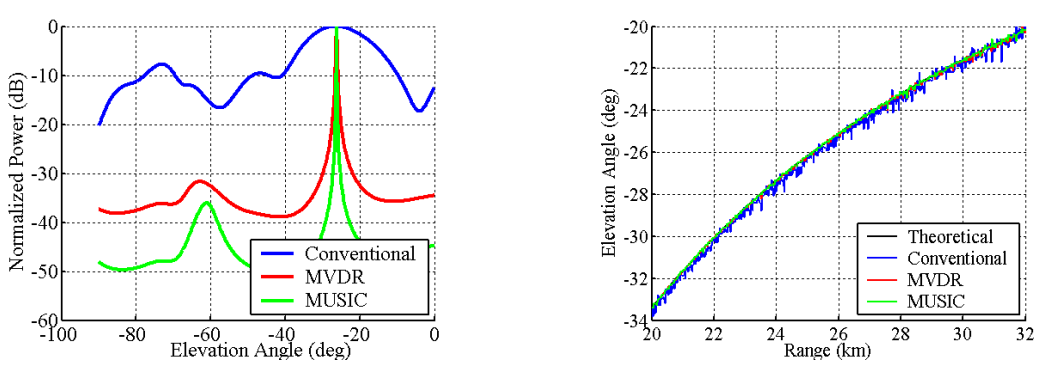

Figure 6.16. Adaptive elevation power plots (left) and range estimates (right) for a chined conformal array.

6.4.2 Single-Peak-Azimuth Doppler Estimates

In this section, we present estimation results of the peak clutter Doppler at the peak azimuth angle. We calculate the theoretical estimates from (6.13) using perfect *a priori* information and obtain the adaptive estimates using the estimation techniques shown in Table 6.4. We analyze the estimation performance of the four array geometries shown in Fig. 6.17 and show a summary of the performance results in Table 6.5.

Table 6.4. Parameters for adaptive clutter Doppler estimates.

Number	Estimation Technique	Peak Search	Temporal DOF	Spatial DOF	Training Ranges
1	Doppler Processing	MVDR	16	N/A	5
2	Independent Space-Time Processing	MVDR	16	N/A	15
3	Joint Space-Time Processing	MVDR	16	5	5

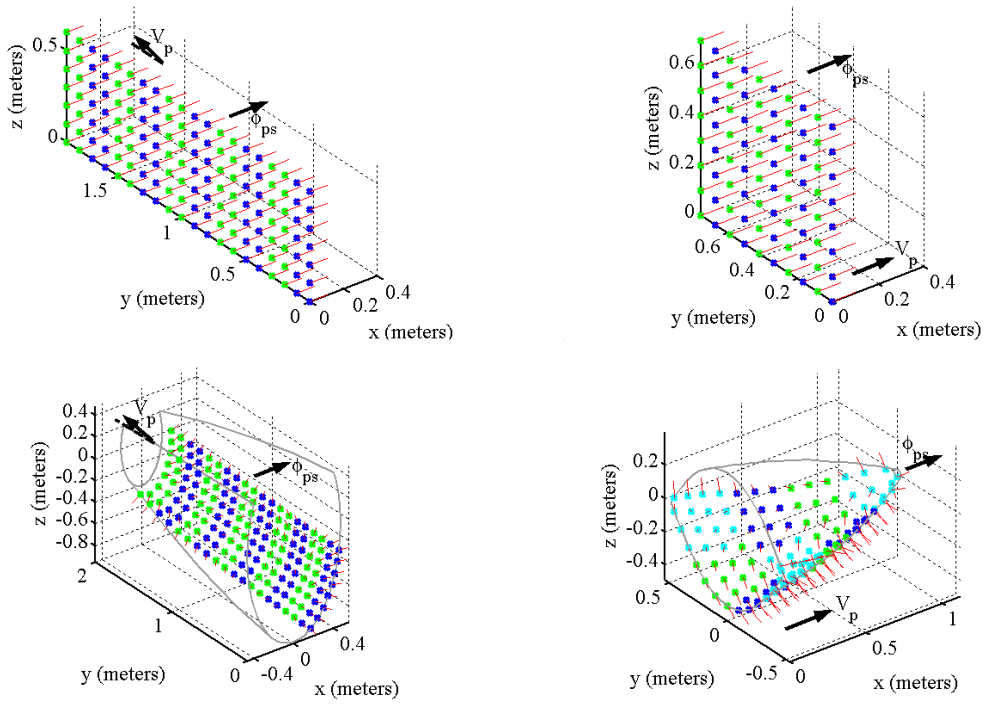

Figure 6.17. Array geometries used for adaptive clutter Doppler estimates.

Table 6.5. RMS errors of adaptive clutter Doppler estimates.

Array Geometry	Estimation Technique	Estimate RMS Error
Crabbed Planar	Doppler Processing	18.08 Hz
	Independent Space-Time Processing	9.82 Hz
	Joint Space-Time Processing with No Equivalent ULA	0.23 Hz
Crabbed Tapered Canoe	Doppler Processing	17.89 Hz
	Independent Space-Time Processing	7.85 Hz
	Joint Space-Time Processing with No Equivalent ULA	5.40 Hz
	Joint Space-Time Processing with an Equivalent ULA	0.23 Hz
Forward-Looking Planar	Doppler Processing	3.96 Hz
	Independent Space-Time Processing	1.92 Hz
	Joint Space-Time Processing with No Equivalent ULA	0.37 Hz
Forward-Looking Chined	Doppler Processing	3.79 Hz
	Independent Space-Time Processing	2.15 Hz
	Joint Space-Time Processing with No Equivalent ULA	5.55 Hz
	Joint Space-Time Processing with an Equivalent ULA	1.73 Hz

We show the Doppler estimate results for the 83°-crabbed ULA in Fig. 6.18. Doppler processing alone shows poor performance, as we are attempting to estimate the peak over a broad range of clutter Doppler frequencies. Limiting the Doppler processing to a single azimuth beam (independent space-time processing) shows some improvement, however the RMS error is still significant. Joint space-time processing gives excellent performance, as the natural ULA geometry allows for easy implementation of this technique.

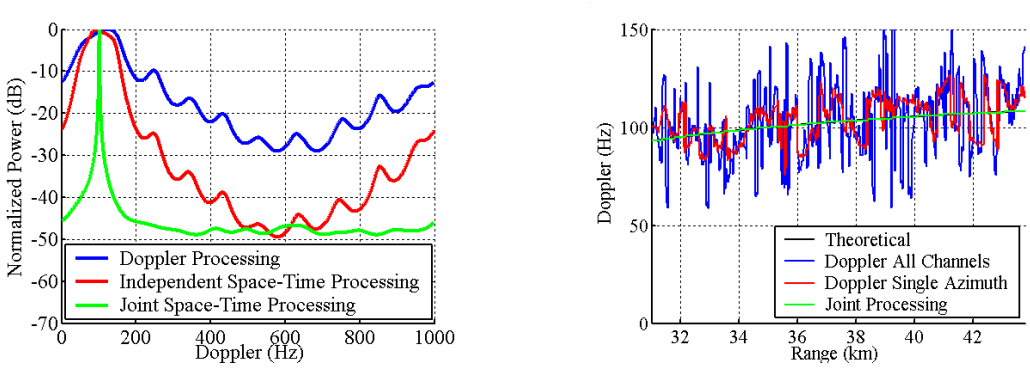

Figure 6.18. Adaptive Doppler power plots (left) and range estimates (right) for a crabbed ULA.

We next look at the Doppler estimation performance of the slightly nonlinear tapered-canoe conformal array. We present the Doppler estimation results for this array in Fig. 6.19. Just as for the ULA, Doppler processing and independent space-time processing techniques result in high RMS errors. Additionally, if we attempt to apply the joint space-time approach directly on the slightly nonlinear phase centers, we again see very poor performance in the form of a biased estimate. However, if we apply joint space-time approach after first applying an equivalent-ULA transformation, we see excellent performance, similar to that of the natural ULA.

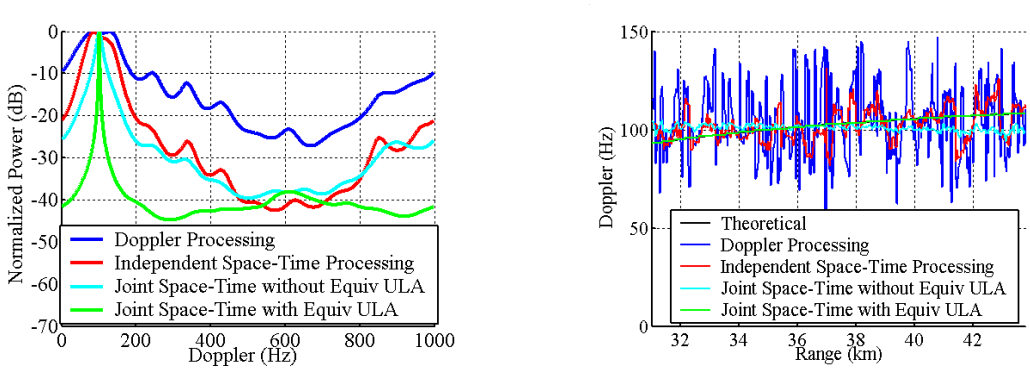

Figure 6.19. Adaptive Doppler power plots (left) and range estimates (right) for a crabbed tapered-canoe conformal array.

We now look at forward-looking applications, starting with a ULA. The forward-looking applications actually present an easier clutter Doppler estimation problem because the mainbeam clutter Doppler range is at its minimum. We see this in the improved Doppler estimation results shown in Fig. 6.20. Both the Doppler processing and independent space-time processing techniques show significant improvement compared to the previous side-looking cases shown in Figure 6.18. The joint space-time processing technique again shows excellent estimation performance.

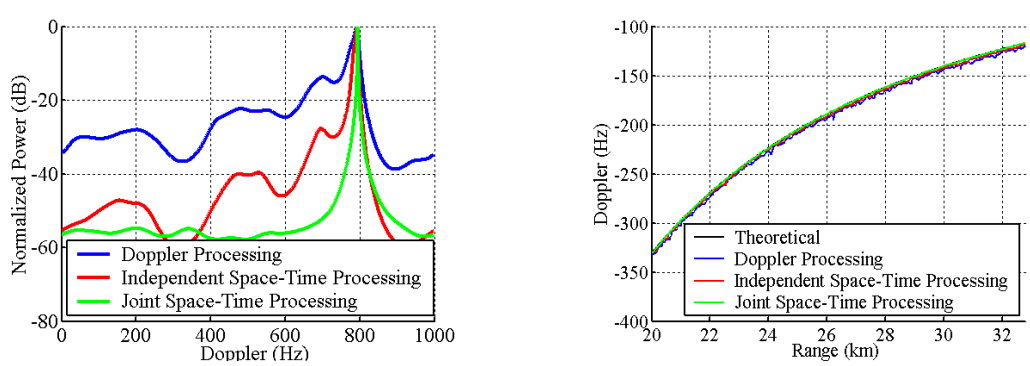

Figure 6.20. Adaptive Doppler power plots (left) and range estimates (right) for a forward-looking ULA.

For our final case, we look at the forward-looking chined conformal array. We show the Doppler estimation results in Fig. 6.21. The Doppler processing and independent space-time processing techniques show similar performance to the previously discussed forward-looking ULA. Additionally, attempting joint space-time processing without an equivalent-ULA transformation results in the expected poor performance. Joint space-time processing with an equivalent-ULA transformation shows significant improvement, however we do not see the same performance as in the previous cases. This is most likely a result of the highly nonlinear subarray phase centers, which do not transform well to a ULA.

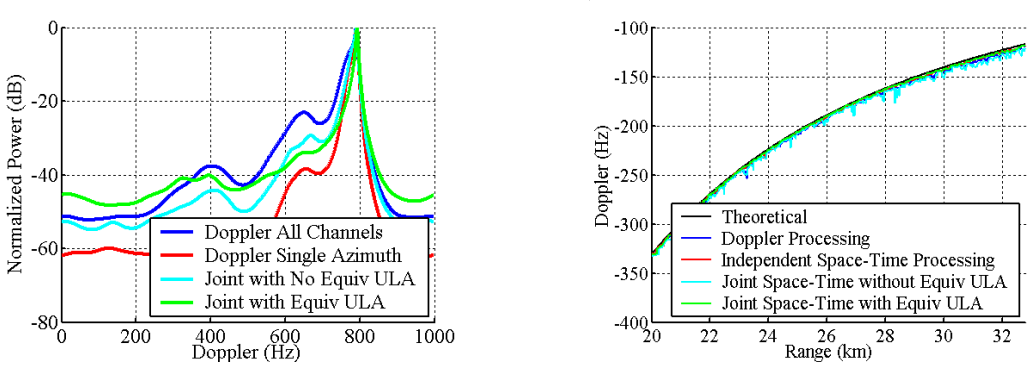

Figure 6.21. Adaptive Doppler power plots (left) and range estimates (right) for a forward-looking chined conformal array.

6.4.3 Multiple-Azimuth Doppler Estimates

The more complicated compensation techniques require Doppler estimates at varying azimuth angles. In this section, we present theoretical and adaptive results for the forward-looking ULA and the forward-looking chined array previously shown in Fig. 6.17. For the multiple azimuth estimates, we cannot apply the Doppler processing

technique, as it has no azimuth control. We can however use the independent space-time processing and joint space-time processing techniques.

In Fig. 6.22 we show theoretical and adaptive results for independent space-time processing for a forward-looking ULA. The estimate at the peak azimuth angle (0°) shows good agreement with the theoretical value. The estimates at the other angles do not show much change from the peak estimate, indicating little sensitivity to the selected azimuth angle. This technique clearly does not work well for multiple azimuth angle estimates.

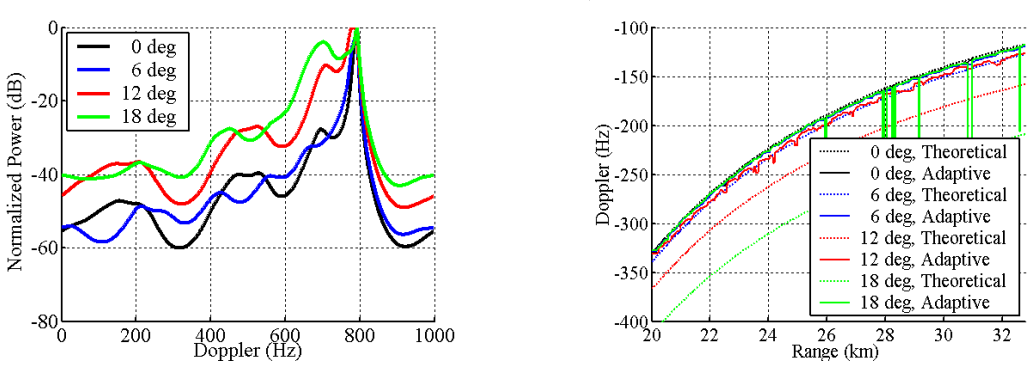

Figure 6.22. Adaptive Doppler power plots (left) and range estimates (right) applying Doppler processing on the given azimuth beam for a forward-looking ULA.

In Fig. 6.23 and Table 6.6 we show theoretical and adaptive results for joint space-time processing at multiple azimuth angles for a forward-looking ULA. The theoretical and adaptive results show good agreement, particularly at the azimuth angles near boresight. At angles further off bore sight, we start to see some degradation in performance and some noticeable bias.

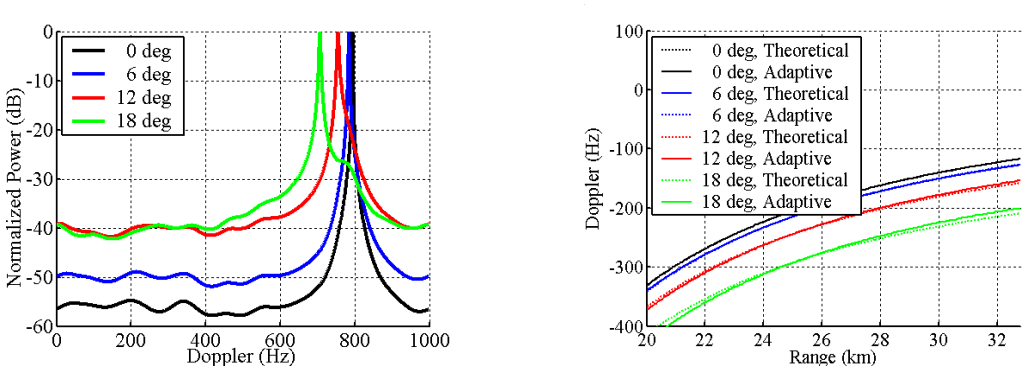

Figure 6.23. Adaptive Doppler power plots (left) and range estimates (right) applying joint space-time processing for a forward-looking ULA.

Table 6.6. RMS errors of adaptive clutter Doppler estimates at varying azimuth angels.

Azimuth Angle	Forward-Looking Planar Array Estimate RMS Error	Forward-Looking Chined Array Estimate RMS Error
0°	0.37 Hz	1.73 Hz
2°	0.38 Hz	1.71 Hz
4°	0.54 Hz	1.70 Hz
6°	0.80 Hz	2.35 Hz
8°	1.25 Hz	3.68 Hz
10°	1.91 Hz	5.62 Hz
12°	2.78 Hz	9.14 Hz
14°	3.67 Hz	16.47 Hz
16°	4.75 Hz	27.92 Hz
18°	6.08 Hz	38.11 Hz
20°	7.51 Hz	36.41 Hz

For our final case, we look at joint space-time processing with an equivalent ULA transformation applied to a forward-looking chined conformal array. We show the multiple-azimuth Doppler estimation results in Fig. 6.24 and again in Table 6.6. These results show significantly poorer performance than the previously discussed ULA. This is most likely a result of the limited angle constraints in the equivalent-ULA transformation.

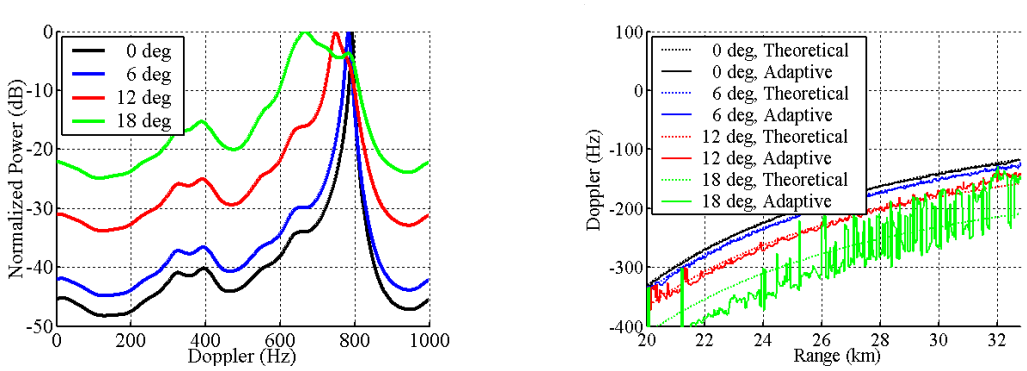

Figure 6.24. Adaptive Doppler power plots (left) and range estimates (right) applying joint space-time processing for a forward-looking ULA.

6.5 Theoretical Angle-Doppler Compensation Results

In this section, we use theoretical estimation techniques with perfect *a priori* knowledge to test the effectiveness of the various angle-Doppler compensation techniques.

For our first case, we apply the Doppler warping technique to an 83°-crabbed ULA. As previously shown in Chapter 4, the clutter returns from this array are moderately nonstationary because the array orientation is not side looking. In Fig. 6.25 we show the adaptive SINR loss with and without Doppler warping. Doppler warping realigns the nonstationary data and gives the expected 3 dB of loss. We see the aligning effect of Doppler warping by comparing the known, estimated, and estimated with Doppler warping MVDR spectra shown in Fig. 6.26. The estimated spectra shows significant spreading in Doppler. The Doppler warping alignment minimizes this effect.

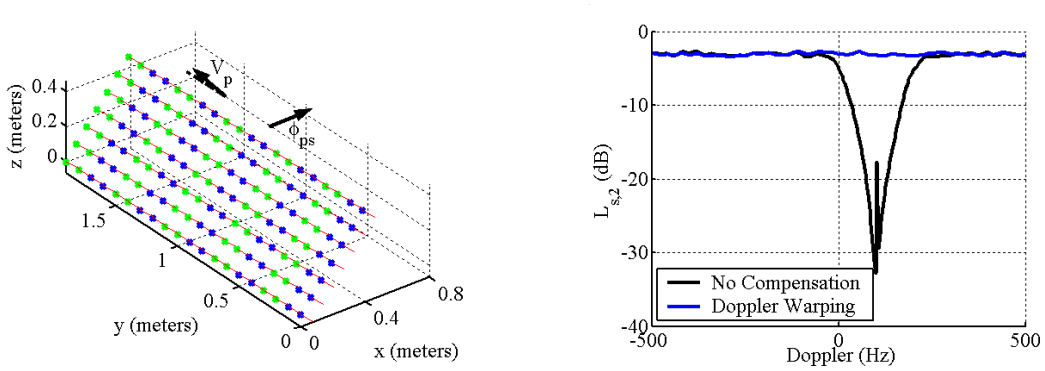

Figure 6.25. Adaptive SINR loss with and without theoretical Doppler warping at a range of 36 km for a crabbed ULA.

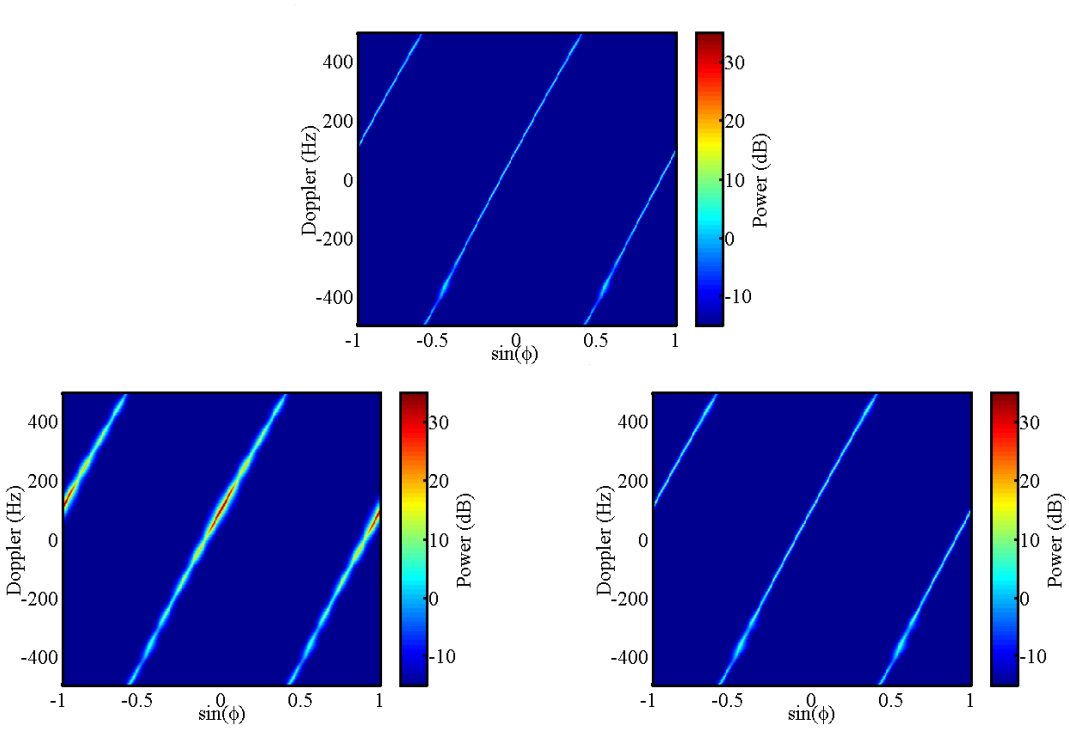

Figure 6.26. Known (top), estimated (bottom left), and estimated with theoretical Doppler warping (bottom right) MVDR spectra for a crabbed ULA.

For the next case, we look at the 83°-crabbed tapered-canoe conformal array, which is a combined case of a nonlinear array geometry and a non-side-looking orientation. In Fig. 6.27 we show adaptive SINR loss for no compensation, Doppler warping only, angle

compensation only, and angle-Doppler compensation. The combined angle-Doppler compensation technique is the only one to fully align the nonstationary data, giving 3 dB of loss over all Doppler. The other techniques have little or no effect. We again analyze this further with the MVDR spectra. In Fig. 6.28 we show known, estimated, Doppler warping, angle compensation, and angle-Doppler compensation 3-D clutter ridge plots. We show the same scenarios for azimuth-Doppler MVDR spectra slices in Fig. 6.29. These plots show how each technique aligns the data. Doppler warping aligns the data in Doppler, but not in elevation. Angle compensation aligns the data in elevation but not in Doppler. Angle-Doppler compensation aligns both angle and Doppler giving the best performance.

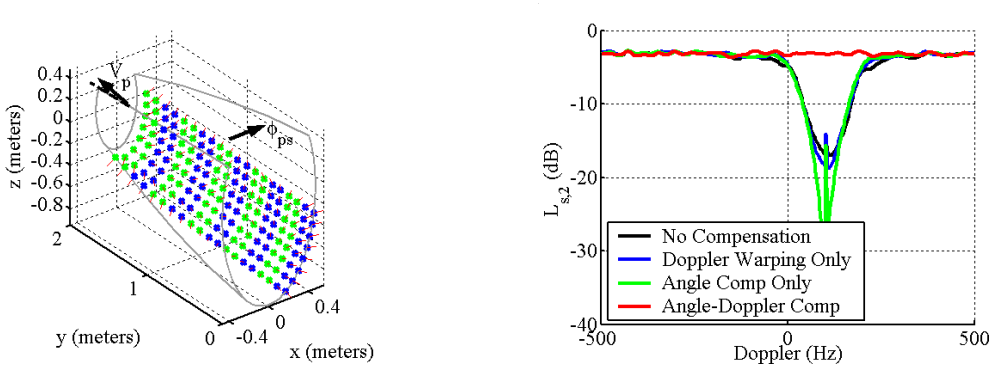

Figure 6.27. Adaptive SINR loss with no compensation, with Doppler warping, with elevation compensation, and with elevation-Doppler compensation at a range of 36 km for a crabbed tapered-canoe conformal array.

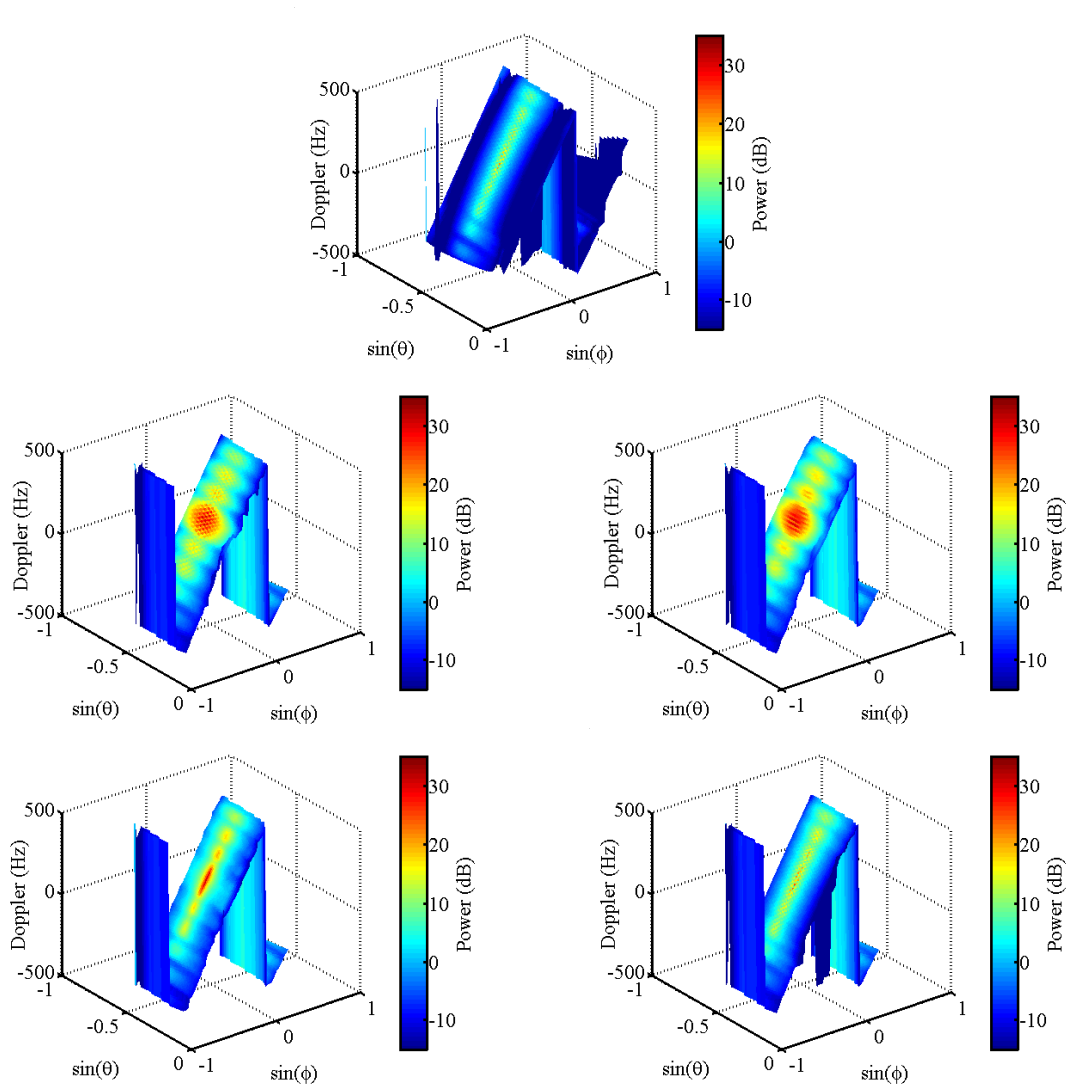

Figure 6.28. Known (top), estimated (middle left), estimated with Doppler warping (middle right), estimated with elevation compensation (bottom left), and estimated with elevation-Doppler compensation (bottom right) 3-D clutter ridges for a crabbed tapered-canoe conformal array.

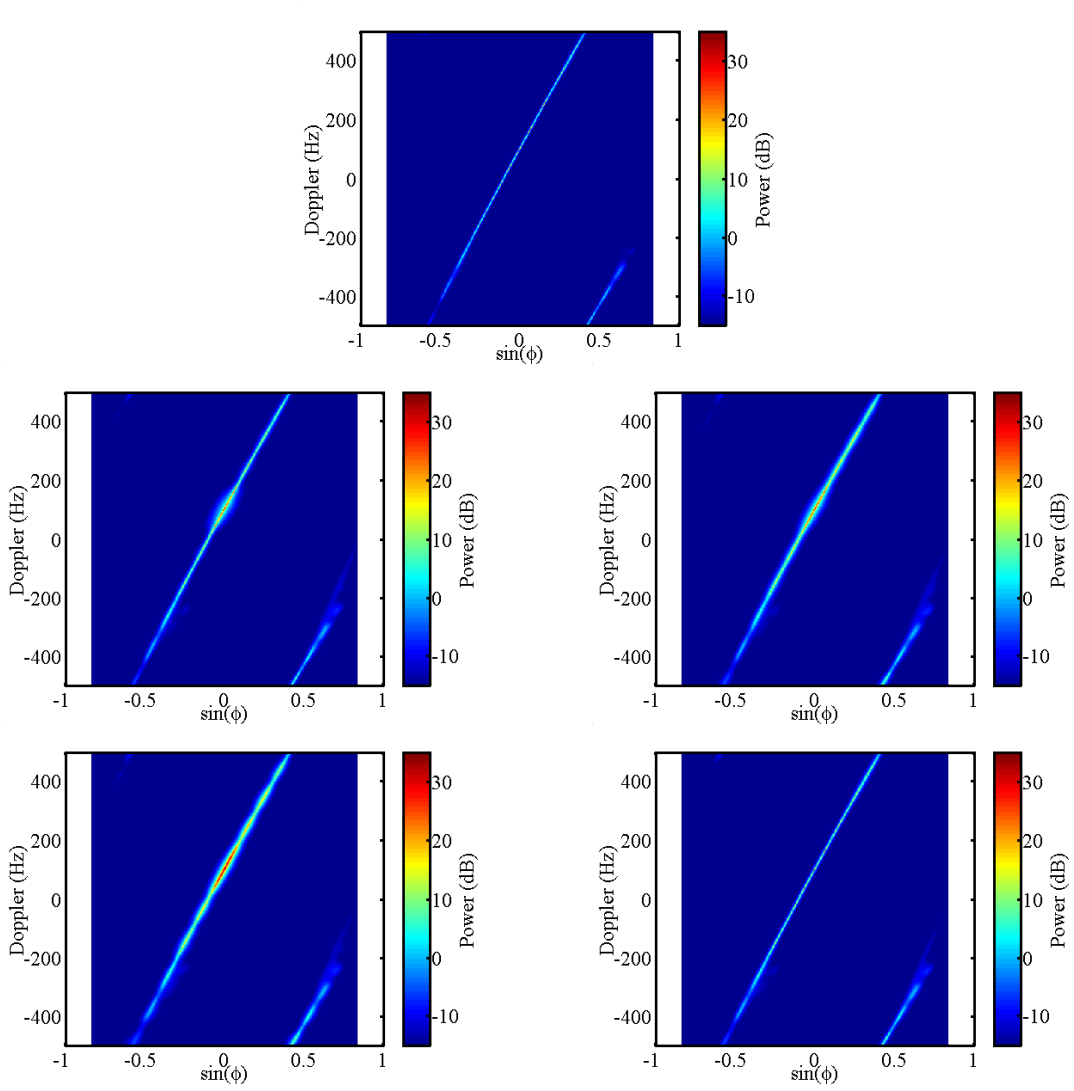

Figure 6.29. Known (top), estimated (middle left), estimated with Doppler warping (middle right), estimated with elevation compensation (bottom left), and estimated with elevation-Doppler compensation (bottom right) azimuth-Doppler MVDR spectra for a crabbed tapered-canoe conformal array.

We next compare the effects of Doppler warping and HODW on a forward-looking ULA. We show adaptive SINR loss for the no compensation, Doppler warping, and HODW cases in Fig. 6.30. Neither Doppler warping nor HODW is able to fully mitigate the nonstationary clutter. Both techniques do, however, show significant improvement. We see this further looking at the MVDR spectra in Fig. 6.31. The estimated spectra shows spreading in Doppler, which is corrected by both Doppler warping and HODW. One drawback of HODW is that it only constrains a limited set of angles. For this result, we choose a localized set of angles and thus angles outside this range show poorer performance. This effect is evident in the MVDR spectra, where we see distortions at high angles $\left(\left|\sin\phi\right| > 0.5\right)$.

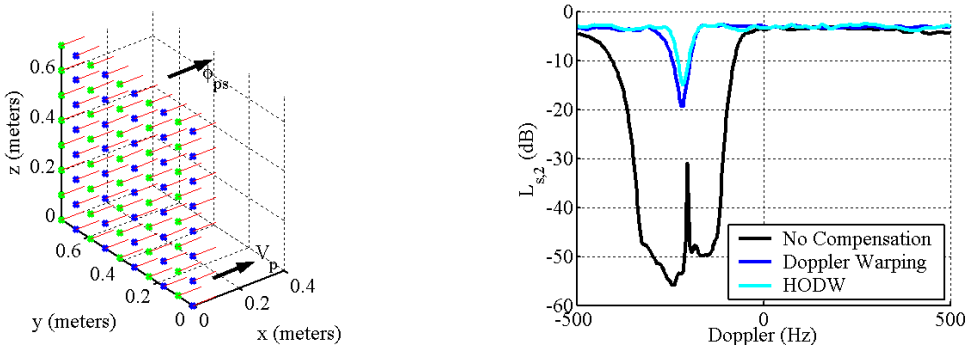

Figure 6.30. Adaptive SINR loss with no compensation, with Doppler warping, and with HODW at a range of 25 km for a forward-looking ULA.

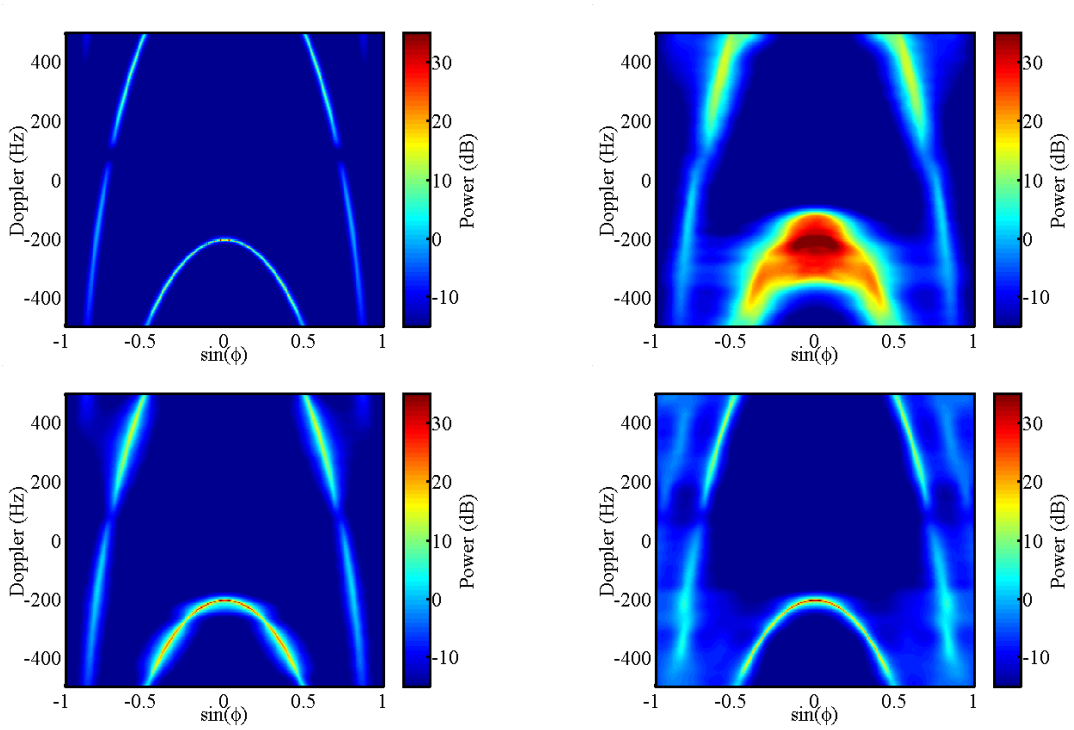

Figure 6.31. Known (top left), estimated (top right), estimated with Doppler warping (bottom left), and estimated with HODW (bottom right) MVDR spectra for a forward-looking ULA.

For our final theoretical case, we compare single-azimuth elevation-Doppler compensation and hybrid elevation-Doppler compensation for a forward-looking chined conformal array. We show this array geometry and adaptive SINR loss in Fig. 6.32. The single-azimuth compensation shows significant improvement in adaptive performance, and the hybrid technique nearly fully mitigates the nonstationary clutter. We again see this effect further in the MVDR spectra shown in Figs. 6.33 and 6.34. Looking at the 3-D spectra, the single-peak and hybrid techniques show similar performance in aligning the clutter elevation angle. Looking at the 2-D azimuth-Doppler slices, however, we see better performance by the hybrid technique, which explains the lower adaptive losses.

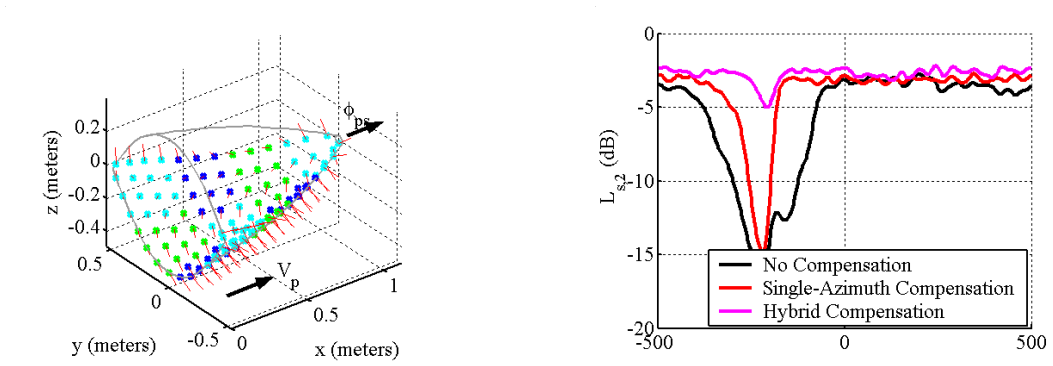

Figure 6.32. Adaptive SINR loss with no compensation, with single-azimuth elevation-Doppler compensation, and with hybrid elevation-Doppler compensation at a range of 25 km for a forward-looking chined conformal array.

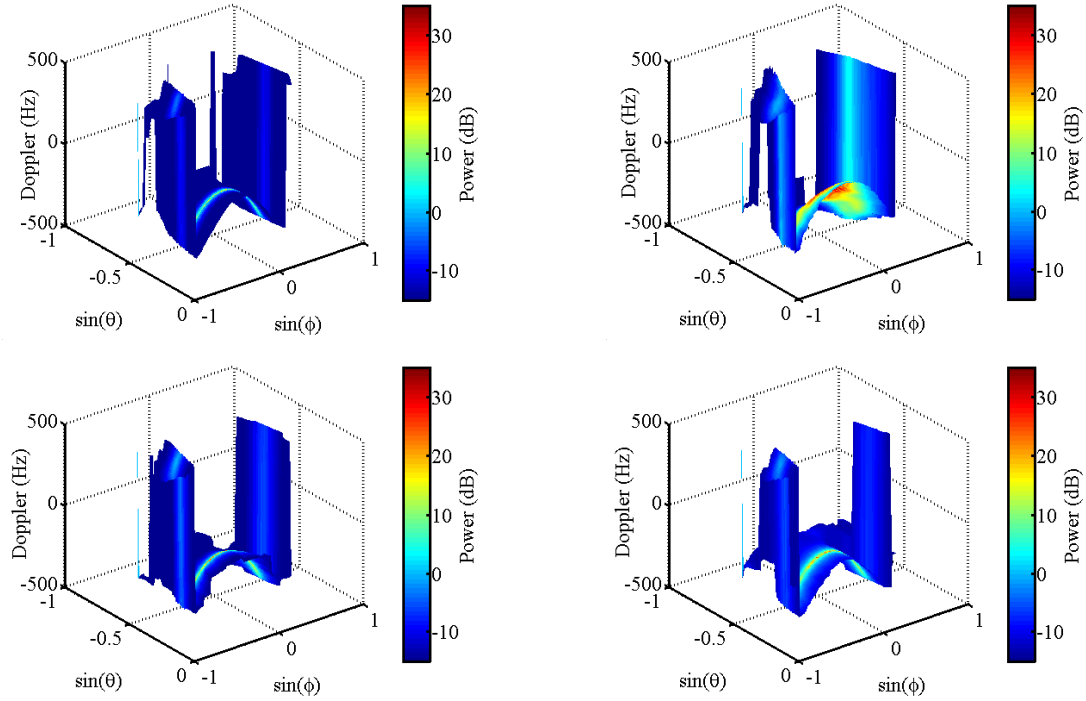

Figure 6.33. Known (top left), estimated (top right), estimated with single-azimuth elevation-Doppler compensation (bottom left), and estimated with multiple-azimuth elevation-Doppler compensation (bottom right) 3-D clutter ridges for a forward-looking chined conformal array.

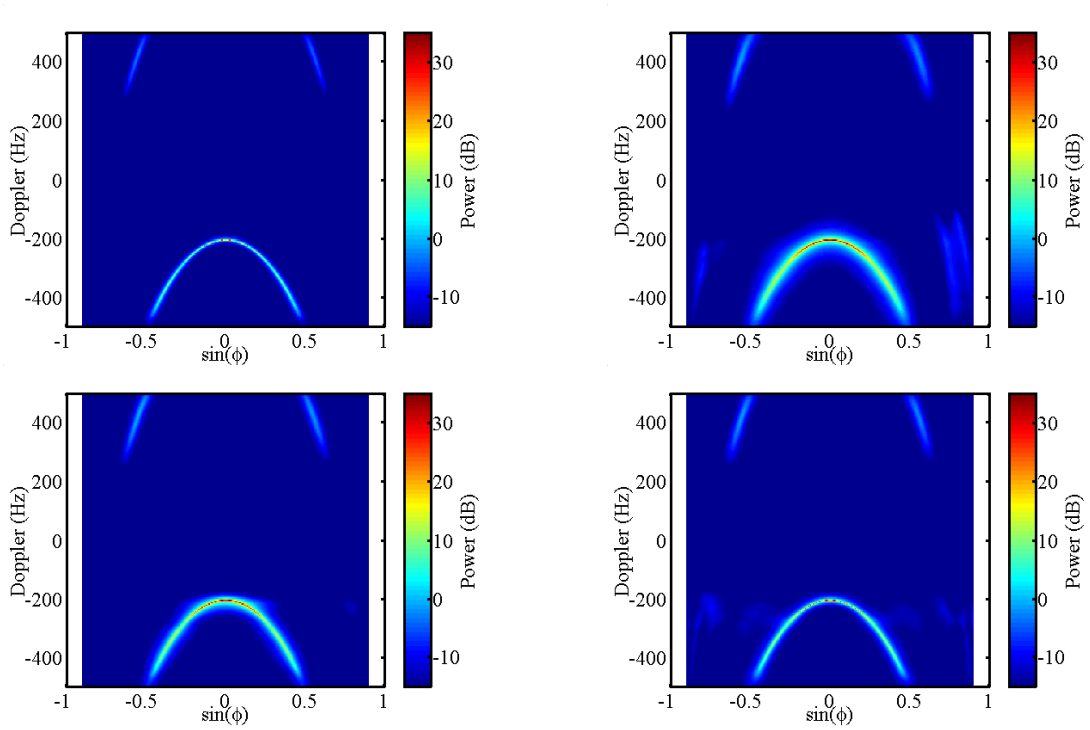

Figure 6.34. Known (top left), estimated (top right), estimated with single-azimuth elevation-Doppler compensation (bottom left), and estimated with multiple-azimuth elevation-Doppler compensation (bottom right) azimuth-Doppler MVDR spectra for a forward-looking chined conformal array.

6.6 Adaptive Angle-Doppler Compensation Results

Results from the previous section all required *a priori* information such as the slant range, the platform height, and the platform velocity vector. In this section we present results that are fully adaptive and require no *a priori* information.

For our first case, we again apply the Doppler warping technique to an 83°-crabbed ULA. In Fig. 6.35 we show adaptive SINR loss for the cases of no compensation, perfect theoretical Doppler warping, and two cases of adaptive Doppler warping. The first adaptive case uses clutter Doppler estimates from independent space-time processing and the second adaptive case uses Doppler estimates from the joint space-time technique.

The independent space-time processing technique results in poor Doppler estimates, which in turn results in correspondingly poor adaptive compensation performance. However, the joint space-time processing technique, which has good adaptive estimation performance, shows some improvement in adaptive losses. We are unable to fully align the nonstationary clutter as in the theoretical technique. However, the theoretical technique requires perfect *a priori* knowledge, which includes knowledge of the array crab. If this crab were unknown to us, the theoretical technique would show no performance improvement, since it assumes a perfectly side-looking array. We show the estimated MVDR spectra for both adaptive cases in Fig. 6.36. For the first adaptive case, we see how we improperly align the nonstationary data, resulting in a poor estimate, whereas the second adaptive case shows some improvement.

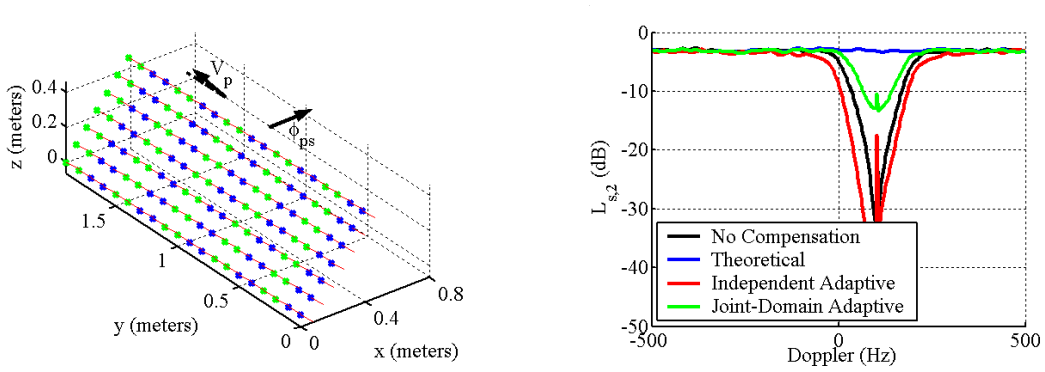

Figure 6.35. Adaptive SINR loss with no compensation, with theoretical Doppler warping, with independent space-time adaptive Doppler warping, and with joint space-time adaptive Doppler warping at a range of 36 km for a crabbed ULA.

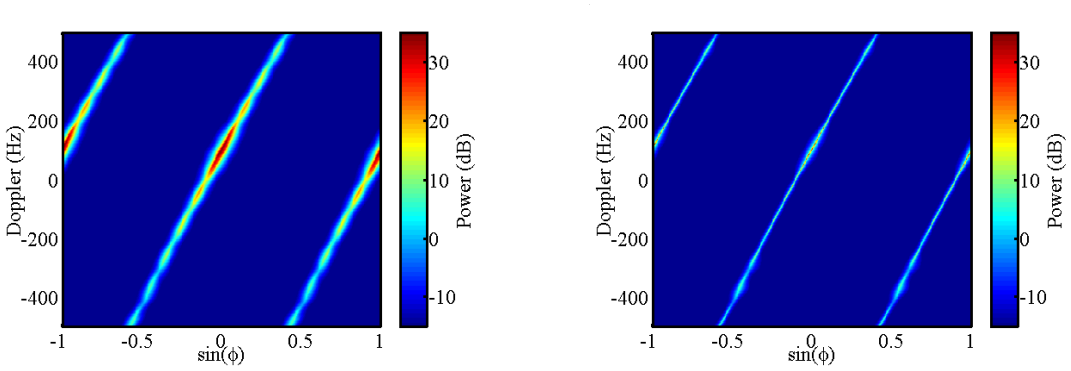

Figure 6.36. Estimated with independent space-time adaptive Doppler warping (left) and estimated with joint space-time adaptive Doppler warping (right) angle-Doppler spectra for a crabbed ULA.

For the next case, we look at the application of single-azimuth elevation-Doppler compensation to the 83°-crabbed tapered-canoe conformal array. We show adaptive SINR loss for the cases of no compensation, theoretical compensation with perfect knowledge, theoretical compensation with errored knowledge , and joint space-time adaptive compensation in Fig. 6.37. Similar to the previous ULA case, the adaptive technique shows some improvement, but is unable to fully mitigate the nonstationary clutter, as in the perfect theoretical case. However, when the array yaw is unknown as in the errored theoretical case, we see improvement using the adaptive technique.

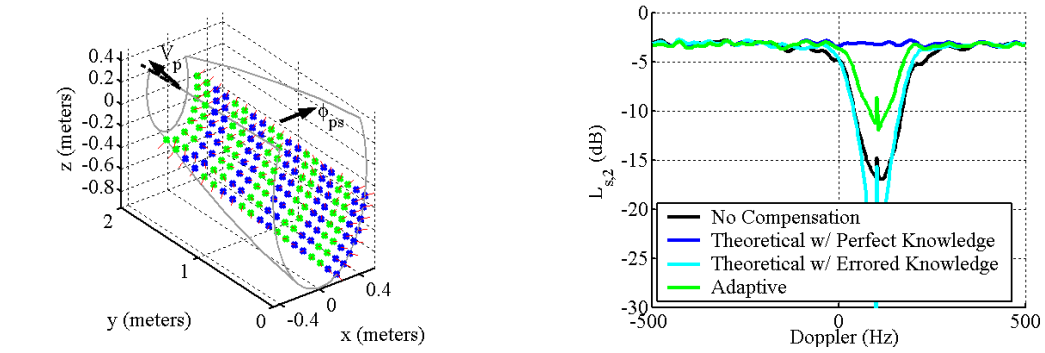

Figure 6.37. Adaptive SINR loss with no compensation, with theoretical single-azimuth elevation-Doppler compensation, and with joint space-time adaptive single-azimuth elevation-Doppler compensation at a range of 36 km for a crabbed tapered-canoe conformal array.

We next look at adaptive Doppler warping and adaptive HODW applied to a forward-looking ULA. We show adaptive SINR loss for the cases of no compensation, theoretical Doppler warping, joint space-time adaptive Doppler warping, theoretical HODW, and joint space-time adaptive HODW in Fig. 6.38. We also show the MVDR spectra for the adaptive cases in Fig. 6.39. First looking at the adaptive Doppler warping results, we see excellent agreement with the theoretical Doppler warping case. In general we find that the forward-looking geometries are less sensitive to the noisy adaptive Doppler estimates and show better agreement with the theoretical techniques. This is most likely a result of the minimal range of the mainbeam clutter Doppler. Looking at the adaptive HODW results, we see poorer performance in comparison with the theoretical result. This is a result of the poor clutter Doppler estimation performance at the higher azimuth angles previously discussed in Section 6.4.3.

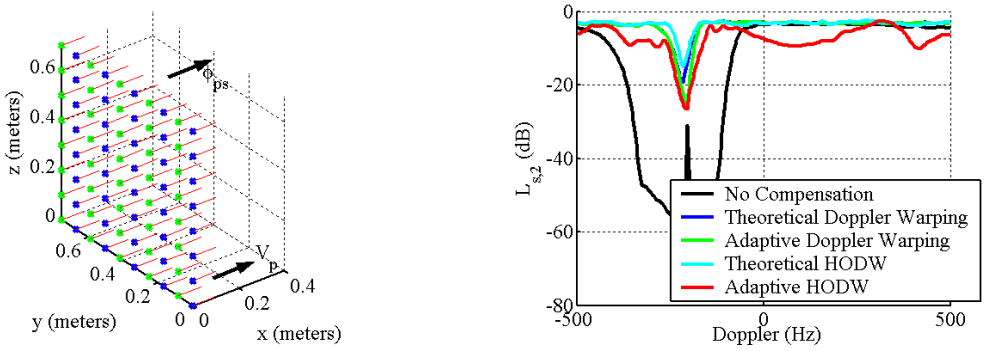

Figure 6.38. Adaptive SINR loss with no compensation, with theoretical Doppler warping, with joint space-time adaptive Doppler warping, with theoretical HODW, and with joint space-time adaptive HODW at a range of 25 km for a forward-looking ULA.

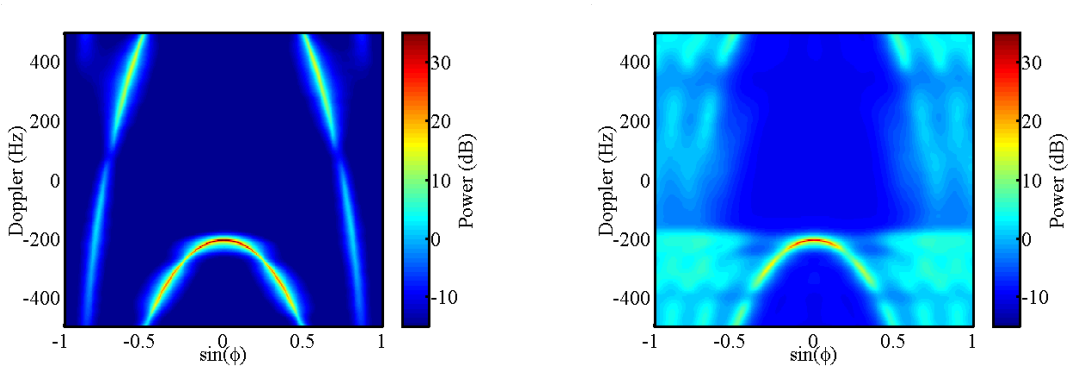

Figure 6.39. Estimated with joint space-time adaptive Doppler warping (left) and estimated with joint space-time adaptive HODW (right) MVDR spectra for a forward-looking ULA.

For our final case, we look at adaptive single-azimuth and hybrid elevation-Doppler compensation applied to the forward-looking chined conformal array. We show adaptive SINR loss results in Fig. 6.40 and MVDR spectra results in Figs. 6.41 and 6.42. Similar to the previous forward-looking ULA case, adaptive single-azimuth elevation-Doppler compensation shows good agreement with its theoretical counterpart. The adaptive hybrid elevation-Doppler compensation shows poor performance which is a result of poor clutter Doppler estimation errors at the higher elevation angles.

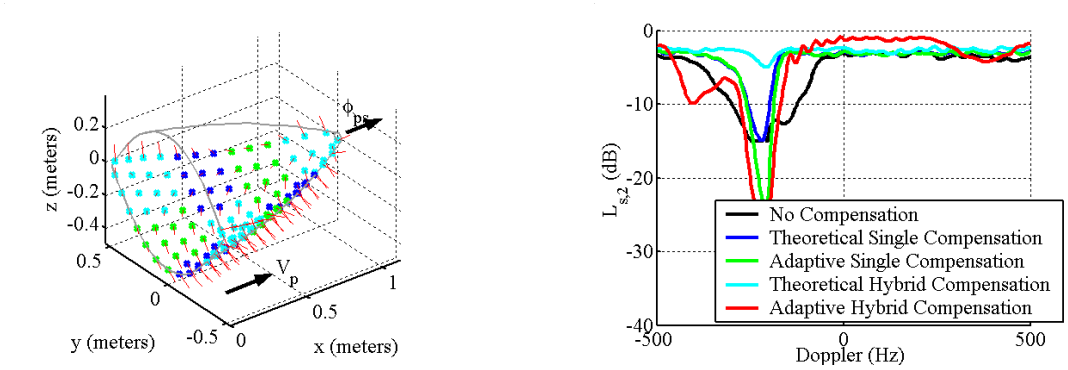

Figure 6.40. Adaptive SINR loss with no compensation, with theoretical single-azimuth compensation, with joint space-time adaptive single-azimuth compensation, with theoretical hybrid compensation, and with joint space-time adaptive hybrid compensation at a range of 25 km for a forward-looking chined conformal array.

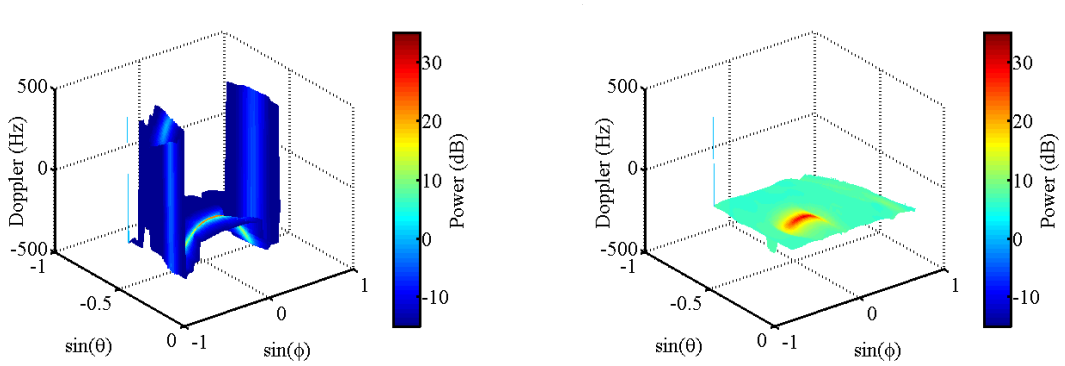

Figure 6.41. Estimated with joint space-time adaptive single-azimuth elevation-Doppler compensation (left) and estimated with joint space-time adaptive single-azimuth elevation-Doppler compensation (right) 3-D MVDR ridges for a forward-looking chined conformal array.

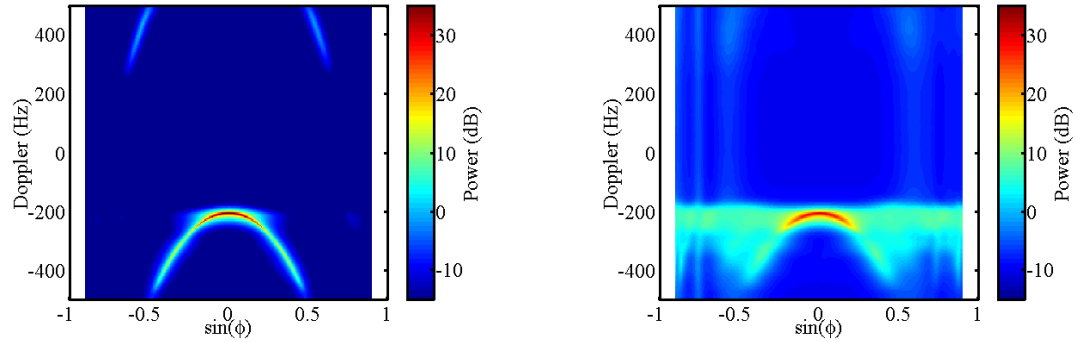

Figure 6.42. Estimated with joint space-time adaptive single-azimuth elevation-Doppler compensation (left) and estimated with joint space-time adaptive single-azimuth elevation-Doppler compensation (right) azimuth-Doppler MVDR spectra for a forward-looking chined conformal array.

6.7 Overall Performance Evaluation

In this section, we combine angle-Doppler compensation with the previously discussed reduced-dimension STAP and time-varying weights techniques. In Fig. 6.43, we show clairvoyant and adaptive SINR loss at a range of 16 km for a forward-looking chined conformal array. We show results for conventional full dimension STAP, EFA, EFA with time-varying weights, and EFA with time-varying weights and adaptive single-

azimuth elevation-Doppler compensation. Localized training and time-varying weights alone still have significant adaptive losses, exceeding 10 dB. The addition of angle-Doppler compensation greatly improves performance, limiting the adaptive loss to about 5 dB.

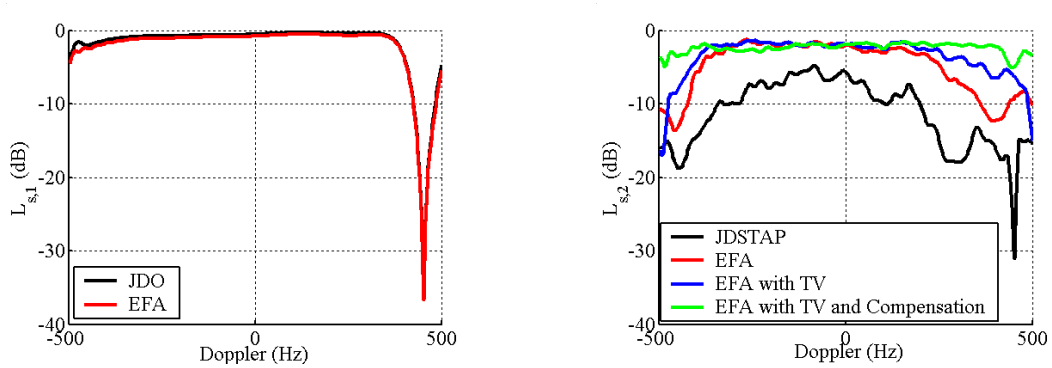

Figure 6.43. Clairvoyant (left) and adaptive (right) SINR loss at a range of 16 km for a forward-looking chined conformal array.

6.8 Summary

In this chapter, we presented a variety of angle-Doppler compensation techniques, which we then applied to a variety of planar and conformal array geometries. With perfect knowledge of the array position and orientation, these techniques mitigated the clutter nonstationarity almost completely. Additionally, we presented fully adaptive techniques, which require no *a priori* knowledge. While not performing as well as their theoretical counterparts, these techniques still showed significant improvement. Finally, we showed an overall performance evaluation of the chined conformal array at a very near range. The combination of angle-Doppler compensation with previously discussed reduced-dimension STAP and time-varying weight techniques, nearly fully mitigated the nonstationary clutter errors.

CHAPTER 7

ARRAY ERRORS AND CALIBRATION

7.1 Overview

Formulation of the adaptive weight vector, $\mathbf{w}_{\mathbf{adap}} = \mu\hat{\mathbf{R}}_k^{-1}\mathbf{v}_{\mathbf{s\text{-}t}}$, requires estimates of both the interference-plus-noise space-time covariance matrix and the space-time steering vector. Thus far we have assumed perfect knowledge of the space-time steering vector in order to evaluate the covariance matrix estimation performance. In this chapter we add both angle-independent and angle-dependent errors to the spatial steering vector and evaluate the impact on adaptive performance. We then present several array calibration techniques as ameliorating solutions.

To evaluate the influence of array errors on adaptive performance, we use the adaptive SINR loss performance metric previously defined in Chapter 3 as

$$L_{s,2} = \frac{\mathrm{SINR}_{\mathrm{adap}}}{\mathrm{SINR}_{\mathrm{opt}}} = \frac{\left|\mathbf{v}_{\mathbf{s\text{-}t,cfa}}^H \hat{\mathbf{R}}_k^{-1}\mathbf{s}_{\mathbf{s\text{-}t,cfa}}\right|^2}{\left(\mathbf{s}_{\mathbf{s\text{-}t,cfa}}^H \mathbf{R}_k^{-1}\mathbf{s}_{\mathbf{s\text{-}t,cfa}}\right)\left(\mathbf{v}_{\mathbf{s\text{-}t,cfa}}^H \hat{\mathbf{R}}_k^{-1}\mathbf{R}_k\hat{\mathbf{R}}_k^{-1}\mathbf{v}_{\mathbf{s\text{-}t,cfa}}\right)}. \tag{7.1}$$

We evaluate this loss under the assumption that we know the space-time covariance matrix exactly, i.e., $\hat{\mathbf{R}}_k = \mathbf{R}_k$, which gives the adaptive losses resulting from steering vector mismatch (SVM) as

$$L_{s,2,SVM} = \frac{\left|\mathbf{v}_{\mathbf{s\text{-}t,cfa}}^H \mathbf{R}_k^{-1}\mathbf{s}_{\mathbf{s\text{-}t,cfa}}\right|^2}{\left(\mathbf{s}_{\mathbf{s\text{-}t,cfa}}^H \mathbf{R}_k^{-1}\mathbf{s}_{\mathbf{s\text{-}t,cfa}}\right)\left(\mathbf{v}_{\mathbf{s\text{-}t,cfa}}^H \mathbf{R}_k^{-1}\mathbf{v}_{\mathbf{s\text{-}t,cfa}}\right)}. \tag{7.2}$$

In this chapter, we present results using combinations of angle-independent and angle-dependent errors, applying all errors at the element level. For the angle-

independent errors, we apply 1.2 dB RMS amplitude errors and a 15° RMS phase errors. For angle-dependent errors, we apply 0.01 m RMS element position errors and 10° RMS element normal errors.

7.2 Array Errors

In this section, we present results for three array geometries with both angle-independent and angle-dependent errors added at the element level. We vary the number of elements in each geometry so the influence of array errors on adaptive performance can be analyzed.

For our first geometry, we look the crabbed planar arrays shown in Fig. 7.1, where we have arrays with 50, 200, and 400 elements. We show plots of transmit patterns both with and without array errors for all three arrays in Fig. 7.2. First looking at plots with no array errors, we see only minor improvement in SLL as the number of elements increases. However, looking at the plots with array errors, we see a significant drop in SLL as the number of elements increases. Adding more elements averages out the array errors lessening their overall effect. In Fig. 7.3 we show clairvoyant and adaptive SINR loss for all three arrays with array errors. First looking at the clairvoyant loss, we see slight changes in the optimum performance with the varying number of elements, which is directly related to the varying transmit patterns. Looking at the adaptive SVM loss, we see a significant change in performance with the varying number of elements.

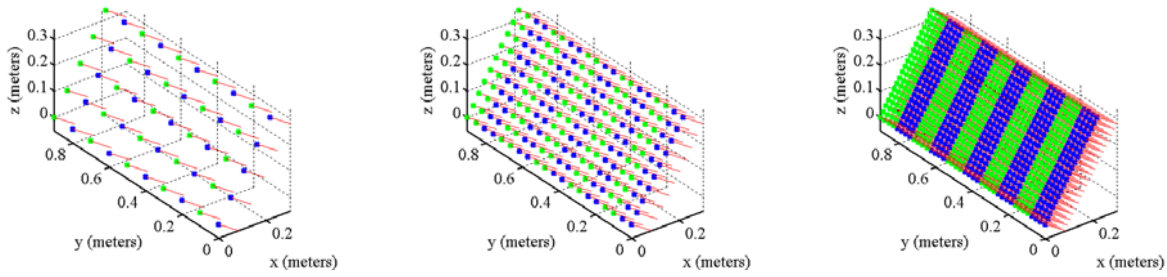

Figure 7.1. Crabbed planar array geometries with 50 elements (left), 200 elements (center), and 800 elements (right).

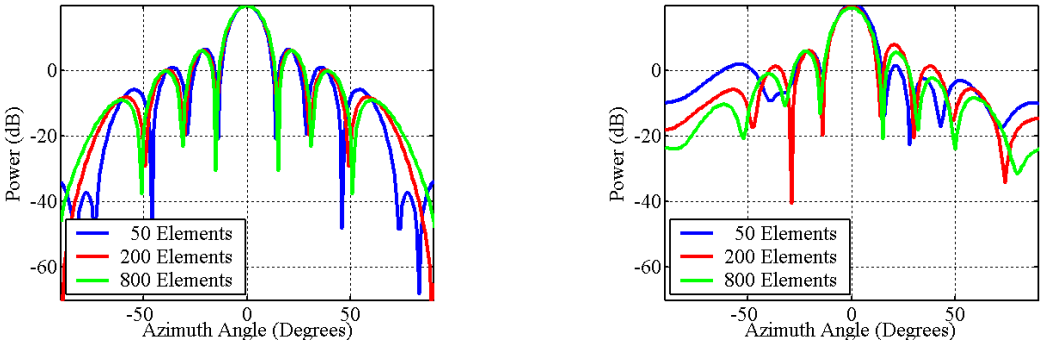

Figure 7.2. Array transmit patterns with (left) and without (right) array errors for a crabbed planar array with 50, 200, and 800 elements.

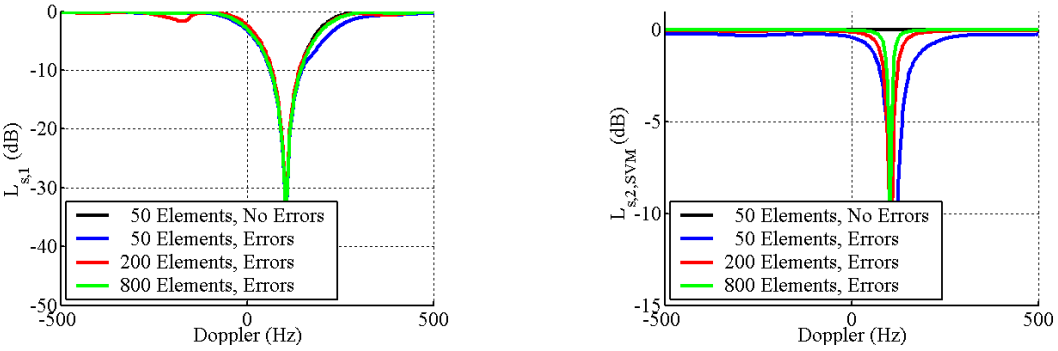

Figure 7.3. Clairvoyant (left) and adaptive (right) SINR loss for a planar array with and without array errors.

For our next geometry, we look at the crabbed tapered-canoe conformal arrays shown in Fig 7.4, where we again have arrays with 50, 200, and 400 elements. We show array transmit patterns with and without array errors in Fig. 7.5 and clairvoyant and adaptive SINR loss in Fig 7.6. Just as for the planar array, increasing the number of elements has little effect on the transmit pattern without array errors but improves the transmit pattern significantly when we include array errors. Similarly, we see a significant improvement in adaptive SVM loss by adding more elements.

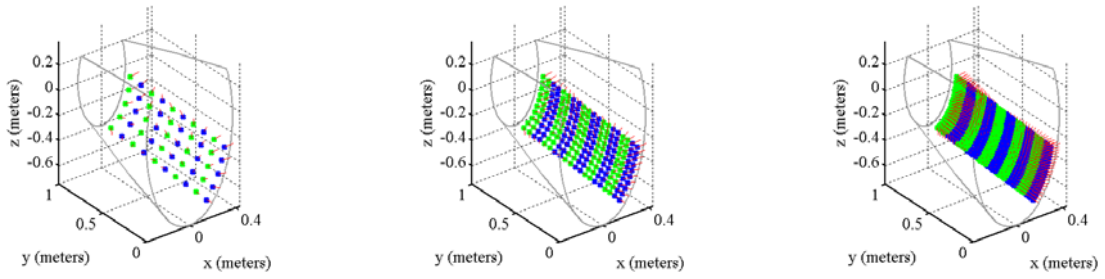

Figure 7.4. Crabbed tapered-canoe conformal array geometries with 50 elements (left), 200 elements (center), and 800 elements (right).

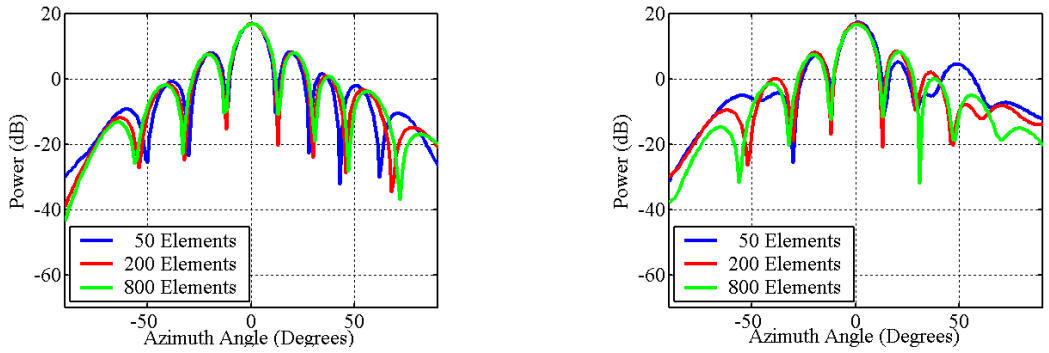

Figure 7.5. Array transmit patterns with (left) and without (right) array errors for a crabbed tapered-canoe conformal array with 50, 200, and 800 elements.

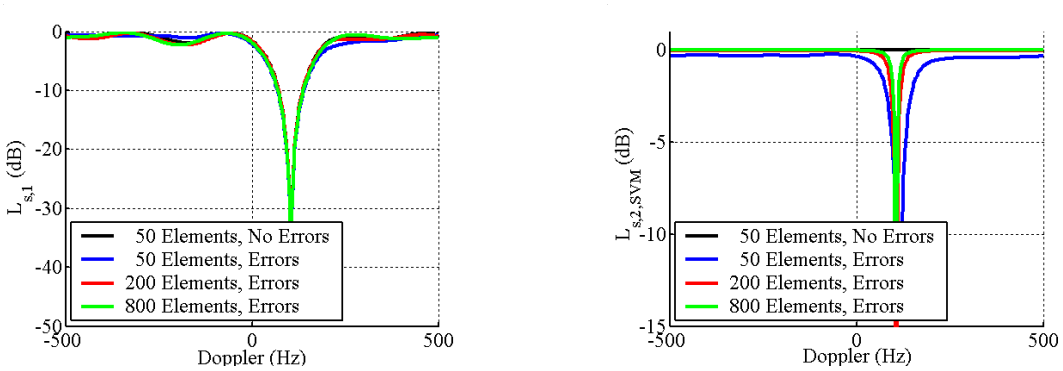

Figure 7.6. Clairvoyant (left) and adaptive (right) SINR loss for a crabbed tapered-canoe conformal array with and without array errors.

For our last geometry, we look at the forward-looking chined conformal array with 117, 455, and 1794 elements as shown in Fig 7.7. We show array transmit patterns with and without array errors in Fig. 7.8 and clairvoyant and adaptive SINR loss in Fig 7.9. We again see similar performance to the previous two geometries in that increasing the number of elements shows little improvement in the transmit pattern when we have no array errors but improves the transmit pattern greatly when we have array errors. Similarly, the adaptive losses decrease as more elements are added.

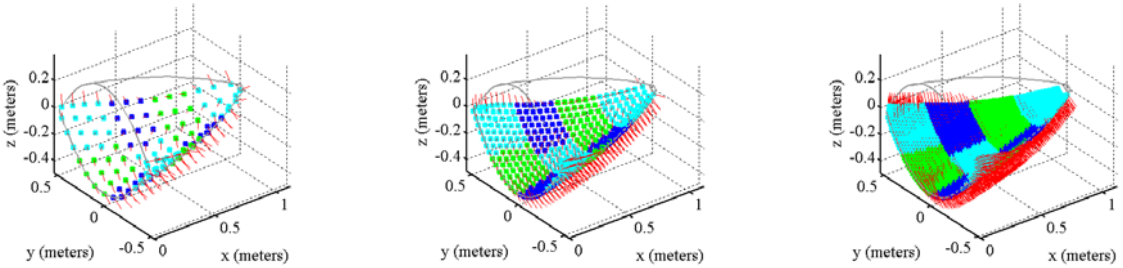

Figure 7.7. Forward-looking chined conformal array geometries with 117 elements (left), 455 elements (center), and 1794 elements (right).

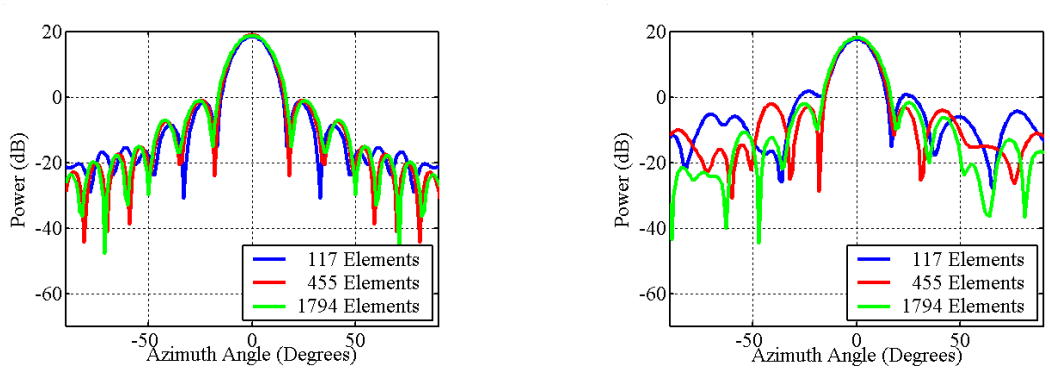

Figure 7.8. Array transmit patterns with (left) and without (right) array errors for a forward-looking chined conformal array with 117, 455 and 1794 elements.

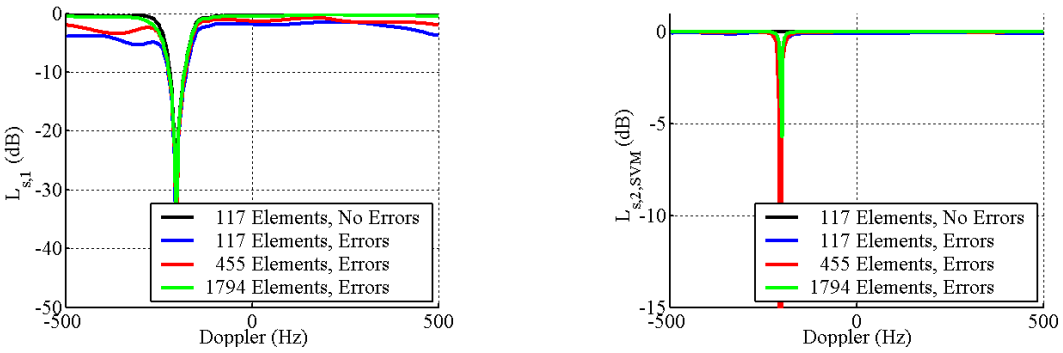

Figure 7.6. Clairvoyant (left) and adaptive (right) SINR loss for a forward-looking chined conformal array with and without array errors.

7.3 Array Calibration

The adaptive losses resulting from SVM are significantly lower than those for covariance-matrix mismatch shown previously in Chapter 4. In comparison, SVM losses only slightly burden clutter suppression performance. However, accurately estimating the spatial steering vector is still critical as it affects DOA estimation accuracy, as well as many of the nonstationary clutter mitigation techniques discussed in Chapters 5 and 6.

7.3.1 Array Calibration Techniques

We present an overview of our array calibration techniques in Table 7.1. These techniques are similar to those for a ULA presented in [44]. Herein, we apply these techniques to the conformal array case. In all of these, we calibrate the array from clutter data, using the max eigenvector of the spatial covariance matrix. Thus, these techniques only find the array spatial steering vector in the direction of the peak clutter returns.

Table 4.1. Overview of array calibration techniques.

Calibration Technique	Doppler Processing	Spatial Covariance Matrix Estimate
Max Eigenvector over all Doppler	Use all pulses (no Doppler processing)	Form a full MxM spatial covariance matrix averaging over pulses
Max Eigenvector at peak Doppler	Use peak Doppler bin for each range	Form a full MxM spatial covariance matrix averaging over range
Reduced Eigenvector over all Doppler	Use all pulses (no Doppler processing)	Form multiple reduced 2x2 spatial covariance matrices averaging over pulses
Reduced Eigenvector at peak Doppler	Use peak Doppler bin for each range	Form multiple reduced 2x2 spatial covariance matrices averaging over range

For our first technique (max eigenvector over all Doppler), we estimate the spatial covariance matrix from

$$\hat{\mathbf{R}}_{\mathbf{s}/k} = \frac{1}{N}\sum_{n=1}^{N} \mathbf{x}_{\mathbf{s}/n,k}\mathbf{x}_{\mathbf{s}/n,k}^{H}, \tag{7.3}$$

where $\mathbf{x}_{\mathbf{s}/n,k}$ is the spatial data snapshot from pulse n and range k. We then estimate the array spatial steering vector for range k as the maximum eigenvector of $\hat{\mathbf{R}}_{\mathbf{s}/k}$ with the normalization such that $\mathbf{v}_{\mathbf{s}/k}^H \mathbf{v}_{\mathbf{s}/k} = M$, i.e.,

$$\mathbf{v}_{\mathbf{s}/k} = \sqrt{\frac{M}{\mathbf{v}_{\mathbf{R},\max}^H \mathbf{v}_{\mathbf{R},\max}}} \mathbf{v}_{\mathbf{R},\max}. \tag{7.4}$$

By using all pulses, we are effectively averaging over all Doppler and azimuth. If we have a broad antenna beam in azimuth, this could result in a poor spatial steering vector estimate.

For our second technique (maximum eigenvector at peak Doppler), we first process the space-time data for each range in Doppler, keeping only the spatial data snapshot corresponding to the peak Doppler bin, $\mathbf{x}_{\mathbf{s}/n_{d,\max},k}$. We then average over range to estimate the spatial covariance matrix from

$$\hat{\mathbf{R}}_{\mathbf{s}/k} = \frac{1}{K} \sum_{r=1}^{K} \mathbf{x}_{\mathbf{s}/n_{d,\max},r} \mathbf{x}_{\mathbf{s}/n_{d,\max},r}^H, \tag{7.5}$$

where K is the number of range bins. Just like the previous technique, we estimate the spatial steering vector from the max eigenvector as in (7.4). This technique has the advantage over the first technique in that we filter the data to the peak Doppler bin and therefore limit the range of the data in azimuth. However, we now must average over range (elevation) to acquire adequate data, which again could result in a poor estimate.

For our final two techniques, instead of estimating the full spatial covariance matrix and maximum eigenvector, we estimate the covariance matrix and maximum eigenvector for each set of channel pairs. This gives a constraint in both amplitude and phase for each of the $M(M-1)/2$ sets of channel pairs. Finally, we find the array steering vector

from the least-squares solution of the set of equations. Just as before, we can apply either Doppler pre-processing option, which gives us the distinction between techniques three and four. The reduced eigenvector techniques offer the advantage of requiring less training data. However, these come at the cost of a least-squares solution, which may be inaccurate due to decorrelation effects between channels.

7.3.2 Array Calibration Results

In this section, we analyze the performance of the array calibration techniques for the array geometries pervious discussed in Section 7.2. We show the array calibration parameters in Table 7.2 and the performance results in Table 7.3. Due to the high computational cost of Monte Carlo trials, we average the RMS amplitude and phase errors over range.

Table 7.2. Array calibration parameters.

Calibration Technique	Number of Temporal Bins	Number of Ranges
Max Eigenvector over all Doppler	32	1
Max Eigenvector over peak Doppler	1	32
Reduced Eigenvector over all Doppler	32	1
Reduced Eigenvector over peak Doppler	1	32

Table 7.3. Array calibration RMS error results.

Array Geometry	Calibration Technique	RMS Amplitude Errors	RMS Phase Errors
Crabbed Planar	No Calibration	0.89 dB	10.47°
	Max Eigenvector, Full Doppler	0.58 dB	13.84°
	Max Eigenvector, Peak Doppler	0.29 dB	6.41°
	Reduced Eigenvector, Full Doppler	0.46 dB	13.30°
	Reduced Eigenvector, Peak Doppler	0.19 dB	8.99°
Crabbed Tapered Canoe	No Calibration	0.88 dB	10.72°
	Max Eigenvector, Full Doppler	0.60 dB	19.92°
	Max Eigenvector, Peak Doppler	0.34 dB	14.87°
	Reduced Eigenvector, Full Doppler	0.62 dB	14.72°
	Reduced Eigenvector, Peak Doppler	0.22 dB	12.71°
Forward-Looking Chined	No Calibration	0.61 dB	4.15°
	Max Eigenvector, Full Doppler	1.55 dB	41.02°
	Max Eigenvector, Peak Doppler	0.50 dB	4.21°
	Reduced Eigenvector, Full Doppler	1.11 dB	34.78°
	Reduced Eigenvector, Peak Doppler	0.44 dB	8.55°

We show the planar array geometry and adaptive SVM SINR loss in Fig. 7.10. All four array calibration techniques show improvement over the result without calibration. The peak-Doppler methods result in significantly lower losses than their full Doppler counterparts. The full-Doppler techniques average over all Doppler (azimuth), whereas the peak-Doppler techniques average over range (elevation). For the broadside of a ULA, the spatial properties vary over azimuth angle and are constant over elevation. As a result, we expect the peak-Doppler techniques to have the best performance. As a final note, the reduced-eigenvector techniques show a slight improvement over the equivalent max-eigenvector counterparts.

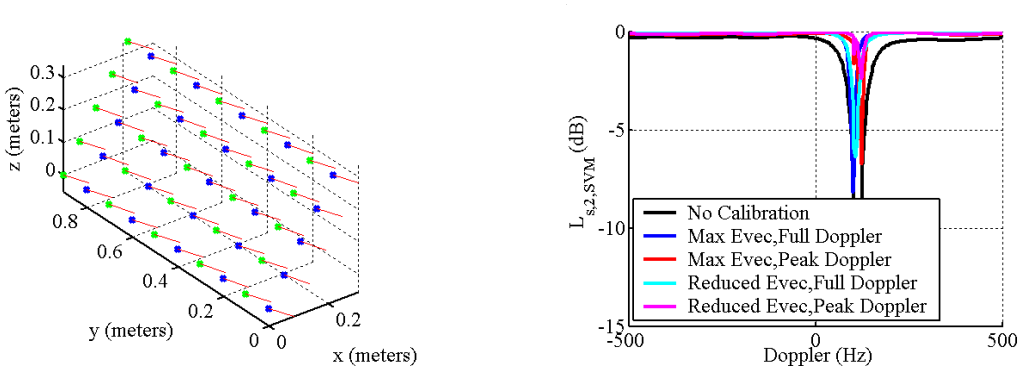

Figure 7.10. Array calibration results for a 50-element crabbed planar array.

Now looking at the first conformal array, we show the tapered-canoe array geometry and adaptive SVM SINR loss in Fig 7.11. These results show similar performance to the previous planar array, where the peak-Doppler techniques show the best performance. Compared to the planar array, the array calibration techniques for the tapered-canoe array perform slightly worse. The nonlinear array geometry hinders the peak-Doppler techniques because the array properties vary over range. Similarly, the nonlinear array geometry broadens the main lobe and creates higher SLLs, which hinder the full-Doppler technique.

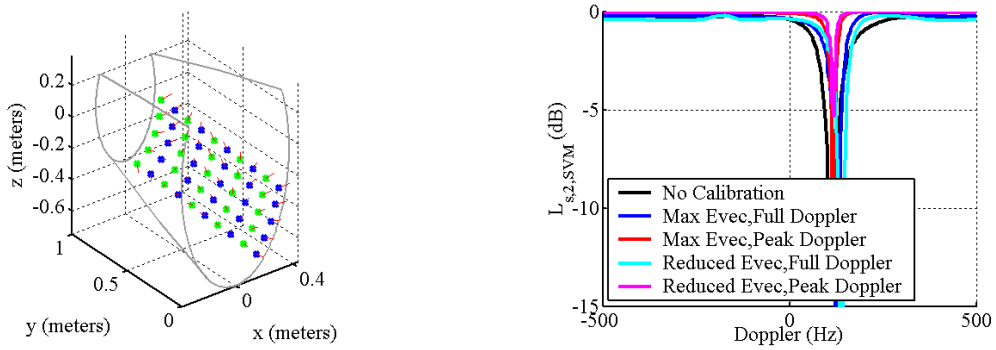

Figure 7.11. Array calibration results for a 50-element crabbed tapered-canoe conformal array.

For the final case, we look at the chined conformal array shown with the adaptive SVM SINR loss in Fig. 7.12. For this array, the full-Doppler techniques perform very poorly. This is most likely a result of the broad main lobe associated with this array. The peak-Doppler techniques show performance comparable with the previous two array geometries.

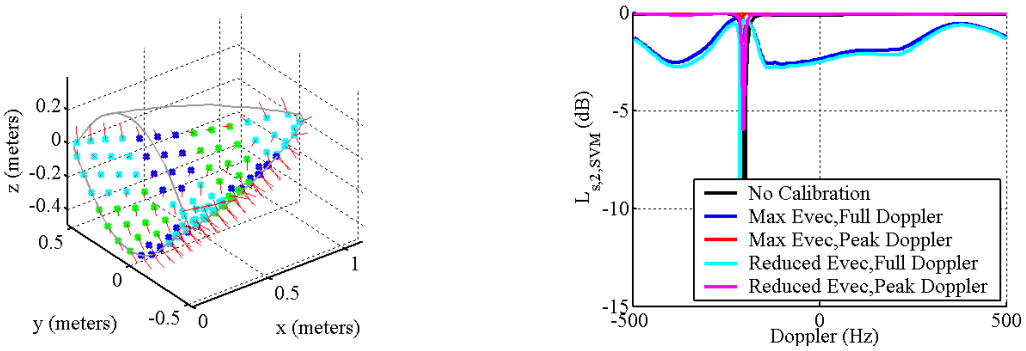

Figure 7.12. Array calibration results for a 117-element forward-looking chined conformal array.

CHAPTER 8

SUMMARY

8.1 Conclusions

In this thesis, we presented the application of STAP to conformal arrays. Conformal arrays assume the shape of the radar bearing platform and generally belong to the class of nonlinear arrays. As a result of this nonlinearity, the assumptions in conventional space-time target models no longer hold. In Chapter 3, we developed a conformal array space-time target model, including a novel subarraying technique and a novel conformal array matched filter definition. Additionally, the conformal array's nonlinear geometry results in array-induced clutter nonstationarity. This nonstationarity leads to high adaptive losses in conventional STAP algorithms, which we described in detail in Chapter 4. In Chapters 4-6, we presented several ameliorating solutions, which we summarize in Table 8.1. These techniques include, reduced-dimension STAP, time-varying weights, equivalent-ULA transformations, and novel angle-Doppler compensation techniques. Finally, we analyzed the impact of array errors and presented potential ameliorating array calibration solutions in Chapter 7.

Table 8.1. Summary of conformal array nonstationary clutter mitigation techniques.

Technique		Application	Description	Comments
Localized Training		All Geometries	Reduce space-time dimensions lowering requisite training samples	Useful at near ranges where limited training samples are available
Time-Varying Weights		All Nonstationary Geometries	Allow for linear variations over fast-time by increasing space-time dimensionality	Useful when at far ranges when clutter nonstationarity is approximately linear
Equivalent-ULA Transformations		All Nonlinear Geometries	Transform data into an equivalent-ULA form and process as if it were a ULA	Compensates for nonlinear geometry not for non-side-looking orientation
Angle-Doppler Compensation Techniques	Doppler Warping	Crabbed Linear Arrays	Apply varying Doppler shifts over fast-time to align peak clutter Doppler returns	Useful for linear arrays when Doppler varies slowly over fast-time
	HODW	Forward-Looking Linear Arrays	Apply varying Doppler shifts over fast-time and azimuth to align clutter Doppler returns	Useful for linear arrays when Doppler varies rapidly over fast-time
	Singe-Azimuth Angle-Doppler	Side-Looking Conformal Arrays	Apply varying elevation and Doppler shifts over fast-time to align peak clutter angle-Doppler returns	Useful for nonlinear arrays when angle-Doppler properties vary slowly over fast-time
	Hybrid Angle-Doppler	Forward-Looking Conformal Arrays	Apply varying elevation and Doppler shifts over fast-time and azimuth to align clutter angle-Doppler returns	Useful for nonlinear arrays when angle-Doppler properties vary rapidly over fast-time

8.2 Future Work

Future work will consider the following:

- Analysis and simulation of polarization and mutual coupling effects in conformal arrays;
- Further investigation of calibration techniques for conformal arrays; and,
- Analysis of the DOA estimation performance of conformal arrays including calculations of Cramer-Rao lower bounds (CRLBs).

REFERENCES

[1] J.R. Guerci, Space-Time Adaptive Processing for Radar, Artech House, Norwood, MA, 2003.

[2] R. Klemm, Space-Time Adaptive Processing: Principles and Applications, IEE Radar, Sonar, Navigation and Avionics 9, IEE Press, 1998.

[3] R. Klemm, Principles of Space-Time Adaptive Processing, 2nd Ed., IEE Radar, Sonar, Navigation and Avionics 12, IEE Press, UK, 2002.

[4] R. Klemm (Ed.), The Applications of Space-Time Processing, IEE Radar, Sonar, Navigation and Avionics 9, IEE Press, 2003.

[5] L.E. Brennan and I.S. Reed, "Theory of adaptive radar," *IEEE Trans. AES*, Vol. 9, No. 2, March 1973, pp. 237-252.

[6] I.S. Reed, J.D. Mallett, and L.E. Brennan, "Rapid convergence rate in adaptive arrays," *IEEE Trans. AES*, Vol. 10, No. 6, November 1974, pp. 853-863.

[7] W.L. Melvin, "Space-time adaptive processing and adaptive arrays: special collection of papers," *IEEE Trans. AES*, Vol. 36, No. 2, April 2000, pp. 508-509.

[8] J.N. Entzminger, C.A. Fowler and W.J. Kenneally, "JointSTARS and GMTI: past, present and future," *IEEE Trans. AES*, Vol. 35, No. 2, April 1999, pp. 748-761.

[9] B. D. Carlson and D. Willner, "Antenna pattern synthesis using weighted least squares," *IEE Proceedings*, Vol. 139, Pt H, No. 1, February 1992, pp. 11-16.

[10] R. F. E. Guy, "General radiation-pattern synthesis technique for array antennas of arbitrary configuration and element type," *IEE Proceedings*, Vol. 135, Pt H, No. 4, August 1998, pp. 241-248.

[11] Leo I. Vaskelainen "Iterative least-squares synthesis methods for conformal array antennas with optimized polarization and frequency properties," *IEEE Transactions on Antennas and Propagation*, Vol. 45, No. 7, July 1997, pp. 1179-85.

[12] Leo I. Vaskelainen, "Phase synthesis of conformal array antennas," *IEEE Transactions on Antennas and Propagation*, Vol. 48, No. 6, June 2000, pp. 987-91.

[13] E. J. Holder, "Sidelobe performance in quadratic phase conformal arrays," *IEEE Transactions on Antennas and Propagation*, Vol. 39, No. 8, August 1991, pp. 1234-1237.

[14] T.E. Morton and K.M. Pasala, "Pattern synthesis and performance of conical arrays," in *Proc. 2004 IEEE Southeastern Symposium on System Theory*, Atlanta, GA, 14-16 March 2004, pp 145-149.

[15] M Dinnichert, "Full polarimetric pattern synthesis for an active conformal array," in *Proc. 2000 IEEE International Conference on Phased Array Systems and Technology*, Palaiseau, France, 21-25 May 2000, pp 415-419.

[16] N Douchin and J. Lemorton, "Numerical analysis of active conformal arrays including crosspolarization effects," in *Proc. 1997 Conference on Antennas and Propagation*, Edinburgh, UK, 14-17 April 1997, Vol. 1, pp 200-205.

[17] M. Zatman, "Circular array STAP," *IEEE Trans. AES*, Vol. 36, No. 2, April 2000, pp. 510-517.

[18] T.K. Sarkar and R. Adve, "Space-time adaptive processing using circular arrays," *IEEE Antennas and Propagation Magazine*, Vol. 43, No. 1, February 2001, pp. 138-143.

[19] L.J. Griffiths, P.M. Techau, J.S. Bergin and K.L. Bell, "Space-time adaptive processing in airborne radar systems" in *Proc. 2000 IEEE Radar Conf.*, Alexandria, VA, 7-12 May 2000, pp. 711-716.

[20] Hien N Nguyen, John D. Hiemstra, and J. Scott Goldstein, "The reduced rank multistage Wiener filter for circular array STAP," in *Proc. 2003 IEEE Radar Conference*, Huntsville, AL, 5-8 May 2003, pp 66-70.

[21] J.G. Worms, "Spatial superresolution with conformal broadband antenna arrays," in *Proc. 2002 IEEE Radar Conf.*, Long Beach, CA, 22-25 April 2002, pp. 425-431.

[22] J.G. Worms, "Spatial superresolution with conformal array antennas," in *Proc. 2000 IEEE Radar Conf.*, Alexandria, VA, 7-12 May 2000, pp. 723-728.

[23] M.I. Skolnik, Introduction to Radar Systems, 2nd Ed., McGraw Hill, New York, NY, 1980.

[24] D.H. Johnson and D.E. Dudgeon, Array Signal Processing, Concepts and Techniques, Prentice Hall, Upper Saddle River, NJ, 1993.

[25] W.L. Melvin, "A STAP overview," *IEEE AES Magazine*, Vol. 19, No. 1, January 2004, pp. 19-35.

[26] S. Haykin, Adaptive Filter Theory, 3rd Edition, Prentice-Hall, Upper Saddle River, NJ, 1996.

[27] R.K. Hersey, W.L. Melvin and J.H. McClellan, "Clutter-limited detection performance of multichannel conformal arrays," *Signal Processing, Special Issue on New Trends and Findings in Antenna Array Processing for Radar,* Vol. 84, No. 9, August 2004, pp. 1481-1500.

[28] D.K. Fenner and W.F. Hoover, "Test results of a space-time adaptive processing system for airborne early warning radar," in *Proc. 1996 IEEE Radar Conf.,* Ann Arbor, MI, 13-16 May 1996, pp. 88-93.

[29] W.L. Melvin, "Space-time adaptive radar performance in heterogeneous clutter," *IEEE Trans. AES,* Vol. 36, No. 2, April 2000, pp. 621-633.

[30] B.C. Armstrong, H.D. Griffiths, C.J., Baker and R.G. White, "Performance of adaptive optimal Doppler processors in heterogeneous clutter," *IEE Proc.-Radar, Sonar, Navig.,* vol. 142, no. 4, August 1995, pp. 179-190.

[31] A. Futernik and A.M. Haimovich, "Performance of adaptive radar in range-heterogeneous clutter," *J. Franklin Institute,* vol. 335B, 1998, pp. 71-87.

[32] W.L. Melvin and J.R. Guerci, "Adaptive detection in dense target environments," in *Proc. 2001 IEEE Radar Conf.,* Atlanta, GA, 1-3 May 2001, pp. 187-192.

[33] K.F. McDonald and R.S. Blum, "Exact performance of STAP algorithms with mismatched steering and clutter statistics," *IEEE Trans. Signal Proc.,* Vol. 48, No. 10, October 2000, pp 2750-2763.

[34] W.L. Melvin, "STAP in heterogeneous clutter environments," in The Applications of Space-Time Processing, ed. R. Klemm, IEE Radar, Sonar, Navigation and Avionics 9, IEE Press, 2003.

[35] W.L. Melvin, M.J. Callahan and M.C. Wicks, "Adaptive clutter cancellation in bistatic radar," in *Proc. 2000 Asilomar,* Pacific Grove, CA, 29 October-1 November 2000, pp 1-7.

[36] W.L. Melvin, M.J. Callahan and M.C. Wicks, "Bistatic STAP: application to airborne radar," in *Proc. 2002 IEEE Radar Conference,* Long Beach, CA, 22-25 April 2002, ISBN 0-7803-7358-8

[37] B Himed, Y. Zhang and A. Hajjari, "STAP with angle-Doppler compensation for bistatic airborne radars," in *Proc. 2002 IEEE Radar Conference,* Long Beach, CA, 22-25 April 2002, pp 186-190.

[38] W.H. Kummer, "Basic array theory," *Proceedings of the IEEE* Vol. 80, No. 1, January 1992, pp. 127-140.

[39] M.A. Zatman, "How Narrow is Narrowband?," *IEE Proc.-Radar, Sonar, Navig.,* Vol. 145, No. 2, April 1998, pp. 85-91.

[40] J.B. Billingsley, A. Farina, F. Gini, M.V. Greco and L. Verrazzani, "Statistical analysis of measured radar ground clutter data, *IEEE Transactions on Antennas and Propagation*, Vol. 35, No. 2, April 1999, pp. 579-593.

[41] T.K. Sarkar, R.S. Adve, and M.C. Wicks, "Effects of mutual coupling and channel mismatch on space-time adaptive processing algorithms," in *Proc. 2000 IEEE International Conference on Phased Array Systems and Technology*, Palaiseau, France, 21-25 May 2000, pp 545-548.

[42] J.E. Luminati and T.B. Hale, "Steering vector mismatch: analysis and reduction," in *Proc. 2004 IEEE Radar Conference*, Philadelphia, PA, 26-29 April 2004, pp 592-597.

[43] R.S. Blum and K.F. McDonald, "Analysis of STAP algorithms for cases of mismatched steering and clutter statistics," *IEEE Transactions on Signal Processing*, Vol. 48, No. 2, February 2000, pp 301-310.

[44] W.L. Melvin, G.A. Showman, and J.R. Guerci, "A knowledge-aided GMTI detection architecture," in *Proc. 2004 IEEE Radar Conference*, Philadelphia, PA, 26-29 April 2004, pp 301-305.

[45] R.C. DiPietro, "Extended factored space-time processing for airborne radar," in *Proc. 26th Asilomar Conf.*, Pacific Grove, CA, Oct. 1992, pp. 425-430.

[46] H. Wang and L. Cai, "On adaptive spatial-temporal processing for airborne surveillance radar systems," *IEEE Trans. AES*, Vol. 30, No. 3, July 1994, pp. 660-670.

[47] B Himed, M.C. Wicks and P. Zulch, "A new constrained joint-domain localized approach for airborne radars," in *Proc. 2002 IEEE Radar Conference*, Long Beach, CA, 22-25 April 2002, pp 403-407.

[48] B Himed, M.C. Wicks and G.J. Gemello, "Accounting for array effects in joint-domain localized STAP processing," in *Proc. Radar 2002*, Edinburgh, UK, 15-17 October 2002, pp 403-407.

[49] M.A. Zatman, "The properties of adaptive algorithms with time varying weights," in *Proc. 2000 IEEE Sensor Array and Multichannel Signal Processing Workshop*, Cambridge, MA, 16-17 March 2000, pp. 82-86.

[50] S.D. Hayward, "Adaptive beamforming for rapidly moving arrays," in *Proc. CIE Int'l Conf of Radar* (IEEE Press), Beijing, China, 8-10 Oct 1996, pp. 480-483.

[51] B. Friedlander and A.J. Weiss, "Direction finding using spatial array smoothing with interpolated arrays," *IEEE Trans. AES*, Vol. 28, No. 2, April 1992, pp. 574-587.

[52] A. Barthelemy, “Application of interpolated arrays for angle estimation,” Technical Memorandum, 14 November 2003, pp. 1-13.

[53] V. Varadarajan and J.L. Krolik, “Space-time interpolation for adaptive arrays with limited training data,” in *Proc. 2003 International Conference on Acoustics, Speech and Signal Processing*, Hong Kong, 6-10 April 2003, Vol. 5, pp. 353-356.

[54] G. Strang, Linear Algebra and Its Applications, 3rd Edition, Harcourt Inc, Philadelphia, PA, 1988.

[55] W.L. Melvin, B Himed and M.E. Davis, “Doubly adaptive bistatic clutter filtering,” in *Proc. 2003 IEEE Radar Conference*, Huntsville, AL, 5-8 May 2003, pp 171-178.

[56] F.D. Lapierre, J.G. Verly and M. Van Droogenbroeck, "New solutions to the problem of range dependence in bistatic STAP radars," in *Proc. 2003 IEEE Radar Conf.*, Huntsville, AL, 5-8 May 2003, pp. 452-459.

[57] F.D. Lapierre, M. Van Droogenbroeck and J.G. Verly, "New methods for handling the range dependence of the clutter spectrum in non-sidelooking monostatic STAP radars," in *Proc. 2003 International Conference on Acoustics Speech and Signal Processing.*, Singapore, June 2003, pp. V_73-V_76.

[58] G.K. Borsari, “Mitigating Effects on STAP processing caused by an inclined array,” in *Proc. 1998 IEEE Radar Conference*, Dallas, TX, 11-14 May 1998, pp 135-139.

[59] O. Kreyenkamp and R. Klemm, “Doppler compensation in forward-looking STAP radar,” *IEE Proc.-Radar, Sonar, Navig*., vol. 148, no. 5, October 2001, pp. 253-258.

[60] K.P. On and B. Mulgrew, “Doppler compensation for JDL for airborne bistatic radar,” in *Proc. 2002 IEEE Sensor Array and Multichannel Signal Processing Workshop*, Cambridge, MA, 4-6 August 2002, pp. 82-86.

[61] F. Pearson and G. Borsari, “Simulation and analysis of adaptive interference suppression for bistatic surveillance radars,” *in Proc. 2001 ASAP*, 13-14 March 2001, Lexington, MA